FIRST-PRINCIPLES SIMULATIONS OF

SOLID STATE BATTERY MATERIALS

BY

JASON HOWARD

A Thesis Submitted to the Graduate Faculty of

WAKE FOREST UNIVERSITY GRADUATE SCHOOL OF ARTS AND SCIENCES

in Partial Fulfillment of the Requirements

for the Degree of

DOCTOR OF PHILOSOPHY

Physics

May 2018

Winston-Salem, North Carolina

Approved By:

Natalie Holzwarth, Ph.D., Advisor

Scott Geyer, Ph.D., Chair

Samuel Cho, Ph.D.

Oana Jurchescu, Ph.D.

Timo Thonhauser, Ph.D.

ACKNOWLEDGEMENTS

For this thesis work I first would like to acknowledge my advisor Dr. N.A.W. Holzwarth for her guidance which has helped me develop into a successful scientist. I would also like to acknowledge the physics and chemistry department faculty and students for both educating me and providing me a sense of community. I also would to acknowledge the grounds keepers at Wake Forest that provide a serene atmosphere through their dedicated care to the plants and trees that decorate the campus. Last but not least I would like to acknowledge my wife, her family and mine for providing the love and support that helps one overcome the challenges of completing a PhD.

Table of Contents

v

Part I

List of Figures

List of Figures

Part II

Abstract

Abstract

In this work materials with possible applications in all solid state Li-ion batteries are explored using computational methods within the framework of density functional theory and kinetic Monte Carlo. The density functional theory simulations use fundamental quantum mechanics along with some approximations to produce accurate models of real materials. A smaller portion of the work uses kinetic Monte Carlo to provide qualitative information about the convergence properties of transport coefficients. The materials $Li_{2+x}SnO_3$ and $Li_{2+x}SnS_3$ are studied in the context of electrodes for Li-ion batteries. Their structures are calculated, conduction pathways for the Li-ions predicted, open cell voltages calculated, and reactivity with lithium at the surface studied. The results for these materials provided insight into existing experimental data from the literature and made predictions for open cell voltages that had not yet been measured. The materials Li_4SnS_4, Li_2OHCl, and Li_2OHBr are studied in the context of solid state electrolytes for Li-ion batteries. The structural properties are explored for some materials by calculating Helmholtz free energies to help understand temperature dependent phases. First principles molecular dynamics are performed on some of these materials to gain insight into the mechanisms for Li-ion diffusion, which is related to the Li-ion conductivity. The molecular dynamics simulations of these materials are also used to calculate order parameters, such as time averaged site occupancies, which provide insight into temperature dependent aspects of their structure. The computations using kinetic Monte Carlo are limited

to the study of the convergence properties of transport coefficients on a lattice equivalent to the Li lattice of Li_2OHCl. These Monte Carlo simulations provide critical insight on the level of statistics needed to converge the transport coefficients related to ionic conductivity. As a whole the simulations in this research provide atomistic level knowledge of real world energy storage materials.

Part III

Introduction

Chapter 1

Thesis introduction

1.1 Overview

The work contained in this dissertation is centered around the calculation of fundamental structural and dynamic properties of solid state battery materials. The work includes both studies of electrodes and electrolytes but is primarily focused on electrolytes. The goal of the research is developing accurate models that aid in the fundamental understanding of materials. The calculations contained in this work are primarily calculated using density functional theory[1,2] with the quantum ESPRESSO code[3] with critical datasets necessary for the computations created with the ATOM-PAW code.[4] Some simulations in one project where completed by kinetic Monte Carlo to provide critical insight on the convergence properties of transport coefficients. The work can be summarized as an effort to understand the basic structural properties, conductivity properties, voltage properties, and phase properties of the materials. Overall the work is applied computational physics to understand battery materials but some of the work includes some mathematical physics and methods development applicable outside of the domain of battery materials. The goal for the work was that by developing accurate models of real materials, insight can be gained at the atomic

scale of the fundamental nature of these materials and questions can be answered that may be experimentally challenging. The models are also meant to serve as conceptual frame works to aid oneself and others in understanding and visualizing the fundamental properties of the material. An inherent part of the modeling process is working as closely with existing experimental data or experimental collaborators as possible. By developing models that reproduce as much of experimental knowledge as possible it is more reasonable to expect that they are an accurate representation of nature and that taking the next step and understanding something not experimentally measured is warranted.

The main driving force behind battery research is the desire for higher capacity batteries with respect to energy and power in terms of both volume (volumetric) and mass (gravimetric). There is also a desire for safer batteries that are not flammable. The electrode materials studied in this work were of interest because of their larger theoretical volumetric and gravimetric energy density compared to a graphite anode. The study of solid state electrolytes is related to the desire of using metallic lithium anodes in lithium ion batteries. The use of a metallic lithium anode offers the highest theoretical volumetric and gravimetric energy density and the use of solid state electrolytes is thought to be a route in achieving this goal. The use of solid state electrolytes also improves safety as compared to many of the liquid polymer electrolytes that are in use today. It is hoped this work can benefit the effort to improve battery technology.

The methods section (chapter 1.2 and 1.3) gives a brief overview of the fundamental quantities to be calculated. This is partitioned into battery physics and quantum mechanics. In the battery physics section the basic quantities to be calculated are described and in the quantum mechanics section the very basics of the fundamental equations are described. The second chapter is a work studying the solid state lithium ion electrodes Li_2SnS_3 and Li_2SnO_3. This work can be described as an effort

to calculate the open cell voltages, ionic conduction pathways, and reactivity of of the materials with lithium at the surface. The third chapter is a study of the solid state electrolyte Li_4SnS_4 as a collaborative effort with Dr. N.A.W. Holzwarth and Ahmad Al-Qawasmeh. This work was centered around calculations of the time dependent motions of the atoms through the method of first principles molecular dynamics. These calculations enabled a deeper understanding of the motion and average location of the lithium ions in Li_4SnS_4. The fourth chapter is a study of the solid state electrolyte Li_2OHCl as a collaborative effort between Zachary Hood and Dr. N.A.W. Holzwarth. This work studying Li_2OHCl involves finding structural models for the temperature dependent phases of the material and studying the lithium ion motion using first principles molecular dynamics in the cubic phase of the material. The fifth chapter is a kinetic Monte Carlo study of the convergence properties of transport coefficients on the lithium lattice of Li_2OHCl which is paired with some first principles molecular dynamics simulations. The kinetic Monte Carlo simulations in this chapter provided critical insight into the statistical, system size, and time dependent convergence properties of tracer diffusion, cross correlations, and mobility on this lattice. The first principles molecular dynamics simulations are interpreted using the kinetic Monte Carlo as a reference. The sixth chapter is a study of the relative stability of the disordered cubic phases of Li_2OHCl and Li_2OHBr compared to ordered structures of the materials. This work addresses the question of why does Li_2OHBr exist in the cubic phase at a much lower temperature than Li_2OHCl.

1.2   Battery physics

The goal of this thesis work was to model solid state battery materials in hopes of revealing fundamental aspects of their properties at an atomistic level. Batteries are a fundamental part of modern technological societies and improvements in battery

technology will allow for them to be used in applications that will help offset the use of fossil fuels. The primary applications where reducing fossil fuels is a concern is automotive and grid power. The development of more advanced battery technology combined with renewable energy resources can allow for this to be achieved. It is the goal of this work that providing a better fundamental understanding of the materials in question will aid in the development process. This chapter will explore some of the fundamental properties of batteries and the equations that determine some of the fundamental physics.

1.2.1 Voltage

To start it is important to note a battery is technically a collection of cells and that this chapter will actually focus on the physics of an individual cell. An individual cell at the theoretical level consists of two electrodes separated by an electrolyte. The electrodes are materials that allow for the creation of a chemical potential difference of a working ion between the ion in/at the chemical environment of one electrode vs the other. The electrolyte is a material that prevents the passage of electrons but allows the passage of ions letting the electrons then pass through an external circuit during discharge to do work. This chemical potential difference is related to the open cell voltage by[5]

$$\frac{\mu_{\varepsilon 1} - \mu_{\varepsilon 2}}{zF} = -V_{\varepsilon_1 vs. \varepsilon_2} \; . \tag{1.1}$$

Where $\mu = \frac{\partial G}{\partial n}$ with G being the Gibbs free energy and n being the particle number of the working ion plus electron neutral pair, ε_1 and ε_2 are the electrodes, z is the charge number of the working ion, and F is Faraday's constant. A positive $V_{\varepsilon_1 vs. \varepsilon_2}$ means a favorable reaction occurs from moving a working ion plus electron from electrode ε_2 to ε_1. The open cell voltage is the maximum possible voltage useful

for extracting work during the discharge process.

1.2.2 Structure

An important aspect of computational studies of materials is finding an appropriate model of the materials in question. This process involves careful comparison with experiment to interpret the computational data. In principle for materials that are in thermodynamic equilibrium at atmospheric pressures (PV is small) the structures should be one that minimizes the Helmholtz free energy[6]

$$\mathcal{F} = \langle E \rangle - TS \tag{1.2}$$

The average internal energy $\langle E \rangle$ and entropy are given in terms of the partition function,

$$Z = \sum_i e^{-\frac{E_i}{k_B T}} \, , \tag{1.3}$$

as

$$\langle E \rangle = -\frac{\partial \ln(Z)}{\partial(\frac{1}{k_B T})} \tag{1.4}$$

and

$$S = \frac{\langle E \rangle}{T} - k_B \ln(Z) \, , \tag{1.5}$$

where T is the temperature and k_B is the Boltzmann constant. The energies E_i appearing in the partition function, within the context of electrons that are adiabatic with the nuclear motions (Born-Oppenheimer approximation), are in principle a function of the nuclear positions $\mathbf{R}_i$ and their velocities $\frac{d\mathbf{R}_i}{dt}$.

In many cases, in particular at low temperatures, the structure of a material is well predicted by only considering the structure with the lowest E_i as a function of nuclear positions.

1.2.3 Ionic conductivity

In battery materials, in particular the electrolyte, one property of importance is the ionic conductivity. Having a high ionic conductivity allows for efficient transfer of the working ion during battery operation by minimizing the Ohmic losses. In terms of linear response theory using the fluctuation dissipation theorem a diagonal element of the dc conductivity tensor has been derived by Kubo[7] to be given in terms of thermodynamic averages as

$$\sigma_{xx}(T) = \frac{V}{2k_B T} \int_0^\infty \langle J_x(t) \cdot J_x(0) \rangle dt \; . \tag{1.6}$$

Where V is the volume and $J_x(t)$ is the x-component of the current density given by

$$J_x(t) = \frac{e}{V} \sum_{i=1}^{N} Q_i \frac{dX_i(t)}{dt} \; . \tag{1.7}$$

Where e is the fundamental charge, N is the total number of ions, Q_i is the charge number of the ion i, and the brackets indicate an average over initial times. The above equation for ionic conductivity in terms of the velocity auto correlation function has been shown by Haile[8] to be equal to the following.

$$\sigma_{xx}(T) = \frac{e^2}{2k_B V T} \lim_{t \to \infty} \frac{\left\langle \left[\sum_{i=1}^{N} Q_i(X_i(t) - X_i(0)) \right]^2 \right\rangle}{t} \; . \tag{1.8}$$

The sum over the charge weighted displacement vectors of the ions will be called the charge moment vector given by the following.

$$p_x(t) \equiv \sum_{i=1}^{N} Q_i(X_i(t) - X_i(0)) \; . \tag{1.9}$$

In many materials there is a single highly mobile ion species with the other ion species effectively trapped in local minimum, under this context the charge moment vector

can be split into a mobile part and non mobile part as

$$p_x(t) = p_x^m(t) + p_x^{nm}(t) \ . \tag{1.10}$$

with m referring to mobile and nm referring to non mobile. The squared charge moment vector is then given as the following.

$$p_x(t)^2 = p_x^m(t)^2 + 2p_x^m(t) \cdot p_x^{nm}(t) + p_x^{nm}(t)^2 \ . \tag{1.11}$$

For the fully non mobile contribution, the ensemble average should limit to a constant in the long time limit, so that when dividing by t as in the definition of the conductivity, the contribution will go to zero. The ensemble average cross term can be argued to go to zero by rewriting the it as

$$\left\langle p_x^m(t) \cdot p_x^{nm}(t) \right\rangle = \left\langle |p_x^m(t)||p_x^{nm}(t)|cos\theta_{m,nm} \right\rangle \ . \tag{1.12}$$

Then noting that because the ensemble average of $\lim_{t\to\infty} |p_x^{nm}(t)|$ is bounded by maximum value defined here as a that Eq 1.12 in $\lim_{t\to\infty}$ is bounded as

$$-a\left\langle |p_x^m(t)| \right\rangle \le \lim_{t\to\infty} \left\langle p_x^m(t) \cdot p_x^{nm}(t) \right\rangle \le a\left\langle |p_x^m(t)| \right\rangle \ . \tag{1.13}$$

Then because $\lim_{t\to\infty} < p_x^m(t)^2 > \to bt$, a constant times time, the inequality can be written as

$$-a\sqrt{bt} \le \lim_{t\to\infty} \left\langle p_x^m(t) \cdot p_x^{nm}(t) \right\rangle \le a\sqrt{bt} \ , \tag{1.14}$$

which when divided by t in the limit both sides of the inequality go to zero. This indicates that it is only necessary to track the mobile ions of the material in question.

For crystalline materials where the mobile ions sit on sites defined by potential energy "valleys" and move be traversing over potential energy barriers, the ionic

conductivity is well modeled by a Arrhenius equation of the form,

$$\sigma = \frac{A}{T}e^{-E_a/k_BT} \ ,$$
(1.15)

where A is a pre-exponential factor, T the temperature, E_a the activation energy, and k_B Boltzmann's constant. For defect free crystalline materials the activation energy E_a normally takes on the form $E_a = \frac{E_f}{2} + E_m$, where E_f is the formation energy of a defect and E_m is the potential energy barrier of the conducting pathway.

1.3   Quantum mechanics

The calculations contained in this work are based on the ideal of atomic scale modeling of the materials. At this level the desirable equation to solve is Schrödinger's equation, which in the time independent form can be written as the following eigen value problem.

$$H\Psi = E\Psi$$
(1.16)

Where H is the Hamiltonian made of the kinetic and potential energy operators, Ψ is the many body wave function, and E is the total energy of the system. This equation is not a relativistic equation and in some cases the more exact Dirac equation must be used, but in this work all systems were modeled with no relativistic effects. In practice, solving the Schrödinger equation exactly is not possible which is more clear if the Hamiltonian is written out in full in Hartree units as following[9, 10]

$$
\begin{aligned}
H = &\frac{1}{2}\sum_{j}^{N_e}\sum_{i\neq j}^{N_e}\frac{1}{|\mathbf{r}_i - \mathbf{r}_j|} + \frac{1}{2}\sum_{J}^{N_I}\sum_{I\neq J}^{N_I}\frac{Z_IZ_J}{|\mathbf{R}_I - \mathbf{R}_J|} \\
&- \sum_{J}^{N_I}\sum_{i}^{N_e}\frac{Z_J}{|\mathbf{r}_i - \mathbf{R}_J|} - \sum_{I}^{N_I}\frac{1}{2M_I}\nabla_I{}^2 - \sum_{i}^{N_e}\frac{1}{2}\nabla_i{}^2 \ .
\end{aligned}
$$
(1.17)

Here Z_I is the atomic charge number of nucleus I, N_e is the number of electrons, N_I is the number of atomic nucleus, $\mathbf{R}_I$ is the position of nucleus I, $\mathbf{r}_i$ is the position of electron i, M_I is the mass of nucleus I in terms of the electron mass, ∇_I^2 is the Laplace operator taking derivatives of the wave function with respect to the coordinates of nucleus I, and ∇_i^2 is the Laplace operator taking derivatives of the wave function with respect to the coordinates of electron i. A Hamiltonian of this form means the wave function Ψ will be a function of all of the nuclear and electronic coordinates given by :

$$\Psi \equiv \Psi(\mathbf{r}_1, .., \mathbf{r}_{N_e} : \mathbf{R}_1, ..., \mathbf{R}_{N_I}) \tag{1.18}$$

This is an immensely difficult problem to solve with the computer time scaling exponentially with the number of particles in the system. Starting in the 1930's efforts were made to simplify the problem and produce approximations that would enable accurate calculations feasible with available computing resources. First came Thomas-Fermi theory, later the Hartree-Fock equations, and then density functional theory along with the Kohn-Sham equations. Layered on top of the fundamental theories are a variety of approximations and implementation methods that allow for real calculations. In the work contained in this dissertation calculations were performed using density functional theory. For this reason the rest of this chapter will be focused on some of the basic theoretical details of density functional theory and its implementation.

1.3.1   Born-Oppenheimer approximation

The first step that can be taken to greatly reduce the computational effort of solving the many body Schrödinger equation is to consider electrons that are adiabatic with the nuclear positions. Considering the electrons adiabatic with the nuclear positions implies that the electron density reaches equilibrium with the nuclear positions practically instantaneously compared with the nuclear motions. This approximation is

rationalized by the much smaller mass of the electron as compared to nuclear masses. This approximation is known as the Born-Oppenheimer approximation and gives the simplified form of the many body Hamiltonian

$$H = \frac{1}{2} \sum_{j}^{N_e} \sum_{i \neq j}^{N_e} \frac{1}{|\mathbf{r}_i - \mathbf{r}_j|} - \sum_{J}^{N_I} \sum_{i}^{N_e} \frac{Z_J}{|\mathbf{r}_i - \mathbf{R}_J|} - \sum_{i}^{N_e} \frac{1}{2} \nabla_i^2 \ . \tag{1.19}$$

1.3.2 Density functional theory

The fundamental principle of density functional theory comes from the Hohnberg and Kohn theorem,[1] which shows that the ground state wave function Ψ_o and its properties are a unique functional of the electron density $n(\mathbf{r})$.[9,10] The theorem is based around variational principle

$$\frac{\langle \Psi' | H | \Psi' \rangle}{\langle \Psi' | \Psi' \rangle} \geq \frac{\langle \Psi_o | H | \Psi_o \rangle}{\langle \Psi_o | \Psi_o \rangle} = E_o \ , \tag{1.20}$$

where Ψ' is trial wave function. The next step is to consider two Hamiltonians H and H' that differ only by an external potential such that

$$H = T + V \tag{1.21}$$

and

$$H' = T + V' \ . \tag{1.22}$$

Here T is the kinetic energy operator and V/V' denote the external potential. Now assuming we are working with normalized wave functions $\langle \Psi' | \Psi' \rangle = 1$ and $\langle \Psi_o | \Psi_o \rangle = 1$ the proof is by reductio adsurdum. Starting with the assumption that there are two Hamiltonians H and H' with ground state wave functions Ψ_o and Ψ' that differ only by the external potential such that $H - H' = V - V'$ but whose ground state wave

functions have the same density $\Psi_o^* \Psi_o = n(\mathbf{r}) = \Psi'^* \Psi'$.

$$\langle \Psi_o | H' | \Psi_o \rangle > \langle \Psi' | H' | \Psi' \rangle = E_1 \tag{1.23}$$

$$\langle \Psi_o | H | \Psi_o \rangle + \langle \Psi_o | H' - H | \Psi_o \rangle > \langle \Psi' | H' | \Psi' \rangle = E_1 \tag{1.24}$$

$$E_2 + \langle \Psi_o | H' - H | \Psi_o \rangle > E_1 \tag{1.25}$$

$$E_2 + \int (V' - V) n(\mathbf{r}) d\mathbf{r} > E_1 \tag{1.26}$$

Then starting by interchaning all the Ψ', H', Ψ_o, and H.

$$\langle \Psi' | H | \Psi' \rangle > \langle \Psi_o | H | \Psi_o \rangle = E_2 \tag{1.27}$$

$$\langle \Psi' | H' | \Psi' \rangle + \langle \Psi' | H - H' | \Psi' \rangle > E_2 \tag{1.28}$$

$$E_1 + \langle \Psi' | V - V' | \Psi' \rangle > E_2 \tag{1.29}$$

$$E_1 - \int (V' - V) n(\mathbf{r}) d\mathbf{r} > E_2 \tag{1.30}$$

By then adding eq 1.26 and eq 1.30 the contradiction,

$$E_1 + E_2 > E_1 + E_2 \tag{1.31}$$

is found. This means that there cannot be different external potentials that give the same density and that the wave function and its properties are a unique functional of the density: $\Psi \equiv \Psi[n(\mathbf{r})]$.

In the context of fixed nuclear coordinates, total energy can be expressed as a functional of the density as follows.

$$E[n(\mathbf{r})] = \int n(\mathbf{r})V(\mathbf{r})d\mathbf{r} - \frac{1}{2}\sum_i^{N_e}\int \psi_i^*\nabla^2\psi_i d\mathbf{r} + \frac{1}{2}\int\int \frac{n(\mathbf{r})n(\mathbf{r}')}{|\mathbf{r}-\mathbf{r}'|}d\mathbf{r}d\mathbf{r}' + E_{xc}[n(\mathbf{r})]$$

$$= E_V[n(\mathbf{r})] + T_{ni}[n(\mathbf{r})] + E_H[n(\mathbf{r})] + E_{xc}[n(\mathbf{r})] .$$

$$(1.32)$$

Where $E_V[n(\mathbf{r})]$ is the energy calculated from the interaction of the potential coming from the fixed nuclei with $V(\mathbf{r})$ being the potential the electrons see from the fixed nuclei, $T_{ni}[n(\mathbf{r})]$ is the kinetic energy of the electrons assuming they are non interacting, the ψ's are wave functions for the individual electrons, $E_H[n(\mathbf{r})]$ is the Hartree approximation to the potential energy of the electrons from the Coulomb interaction, and $E_{xc}[n(\mathbf{r})]$ is the exchange and correlation energy which takes into account everything missing from the other terms. The key equations solved in the codes used in this work are the Kohn and Sham equations[2,9,10]

$$[\frac{-\nabla_i^2}{2} + V_N + V_H + V_{xc}]\psi_i = \epsilon_i\psi_i , \tag{1.33}$$

where $\frac{-\nabla_i^2}{2}$ is the kinetic energy operator for wave function i, V_N is the potential energy operator from the fixed nuclear positions, V_H is the Hartree (classical) potential energy operator for the electron electron Coulomb interaction, V_{xc} is defined as the functional derivative of $E_{xc}[n(\mathbf{r})]$ with respect to $n(\mathbf{r})$. The density $n(\mathbf{r})$ is determined with the wave functions ψ_i by

$$n(\mathbf{r}) = \sum_i^{N_e}\psi_i^*(\mathbf{r})\psi_i(\mathbf{r}) . \tag{1.34}$$

To find an approximation to the ground state energy, trial wave functions are guessed

and then $n(\mathbf{r})$ determined from this. With $n(\mathbf{r})$, the potential energy operator $V_H + V_{xc}$ in Eq. 1.33, is known so these equations can then be solved. The resultant wave functions are then used to calculated a new density and the process is repeated until predetermined self consistency is achieved based on numerical convergence criteria. With the resultant wave functions from the self consistent procedure the total energy can then be determined with Eq. 1.32. In practice the energy is only approximated and this is due to the exchange and correlation term which must be treated with an approximation. In this work the approximation used for all calculations is known as the local density approximation (LDA).[11] Other approximations important for calculations of solids are the frozen core approximation which freezes the electron density for the all electron result for the isolated atomic species up to some defined valence. With the remaining density that is free during the calculations the method of pseudo potentials is used to treat the wave functions close to the nuclear cores. In this work the pseudo potentials were implemented in the projector augmented wave formalism using the ATOMPAW code[4] to generate necessary datasets and the quantum ESPRESSO code for simulations.[3]

1.3.3   Connections to battery physics

The Kohn-Sham equations allow for the calculation of the total electronic kinetic plus potential energy of the electrons in terms of the nuclear positions. With these values important properties of materials can be calculated. The calculation of this total electronic energy is the starting point for the calculation of many the pertinent quantities of batteries. The chemical potentials that appear in the equation for the open cell voltage depend on differences in energy. The ionic conductivity can be calculated by doing classical molecular dynamics using the quantum mechanical calculation of the electron density to determine the forces on the ions. These calculated total electronic energies can be interpreted through the partition function to predict

thermodynamically favorable structures. Perturbation theory can be applied to the wave functions computed with the Kohn-Sham equations and allow for a harmonic treatment of lattice vibrations, which allows for more accurate claculations of the Helmholtz free energies.

Chapter 2

First principles simulations of Li$_{2+x}$SnO$_3$ and Li$_{2+x}$SnS$_3$

2.1 Introduction

This work started as a project by the suggestion of my advisor Dr. N.A.W. Holzwarth to understand the Li-ion conduction process in the materials Li$_2$SnO$_3$ and Li$_2$SnS$_3$. The initial work consisted of looking for migration pathways of a vacancy in the crystal lattices. The initial work also involved looking for possible vacancy interstitial pairs in the crystal lattices and calculating their formation energy. Initially it was thought that the materials may have electrolyte properties and they could be of interest in that aspect for battery materials. Literature review revealed that Li$_2$SnO$_3$ had been studied as an electrode material for Li-ion batteries. This information about Li$_2$SnO$_3$ led to the idea of doing simulations with regard to its electrode like properties and motivated comparison with Li$_2$SnS$_3$ to answer the question "does Li$_2$SnS$_3$ have the same electrode properties as Li$_2$SnO$_3$". The next couple paragraphs will give an overview of this project which eventually culminated in a research article published in Physical Review B.[12]

One goal of studying a solid state ionic conductor is to understand the conduction mechanisms. Both the materials Li_2SnO_3 and Li_2SnS_3 had previous reports of their Li-ion conductivity through impedance measurements. The use of theoretical models allows for a picture like view at the atomic scale of the atoms in the crystal lattice. With a good enough simulation, the hope is that with comparison to experiment the conduction mechanism can be identified in the material. This was a primary goal of the work. In the work the, first conduction mechanism investigated was the vacancy mechanism, which is a common conduction mechanism in ionic crystals. The second, which came after the identification of interstitial locations in the lattice, was an interstitialcy mechanism. The interstitialcy mechanism is also referred to the "kick-out" mechanism, which involves a interstitial site pushing out a host lattice site into another adjacent interstitial site and then taking its place. In this work the mechanisms found were evaluated in terms of there activation energy and then compared to experimental values. There was reasonable agreement with experiment and some further insights could be proposed based on the simulations.

After performing literature review and it was discovered that Li_2SnO_3 had electrode like properties, it was decided to study the material in this context. The available literature described that Li_2SnO_3 could be used as a secondary electrode (anode) where in the first cycle it would react with excess lithium and become an amorphous material of Li_2O and Sn, the Sn would then alloy and de-alloy with the lithium. The usefulness of the material came from the principle that the Li_2O would buffer volume changes of the alloying and de-alloying of Li with the Sn. The initial goal was to study the initial decomposition process of the material. To do this Li were randomly placed on the available interstitial sites over the concentration range $0 < x < 1$ in $Li_{2+x}SnO_3$. The calculations agreed with experiment in that they predicted a transition from crystalline to amorphous at approximately the experimentally observed value of x. The calculations where further compared to experiment by calculation of

open cell voltages (vs bcc Li). The voltage calculations where in disagreement with experiment even when carefully sampling configurational dependence. Calculations of the open cell voltage including possible defects identified in the literature gave evidence of Li/Sn site sharing in the material. Calculations were also performed for Li absorption on to the surface and interfacing with bulk lithium. These simulations found lithium could be favorably adsorbed to the surface and that the material was metastable (thermodynamical unstable but with kinetic barrier) at the surface with respect to bulk lithium.

The material Li_2SnS_3 had less previous research and had just recently been categorized in terms of structure and Li-ion conductivity. The goal of the project become to compare and contrast with Li_2SnO_3. This included performing the same calculations of the lithiation process. The simulations found that Li_2SnS_3 also had electrode like properties with a positive voltage verus bcc Li , but the material did not decompose under bulk intercalation of lithium onto the interstitial sites. The voltage calculation of Li_2SnS_3 was corroborated by an experimental measurement published after our publication from an independent research group.[13] Calculations of lithium absorption to the surface and interfaces with bulk lithium revealed some contrast to Li_2SnO_3. The results showed that there was favorable adsorption of lithium to the surface and that the interface of Li_2SnS_3 with bulk lithium was unstable.

The completion of this project required some level of programming. The purpose of this programming could be described as both to prepare input files for Quantum ESPRESSO and post processing of the Quantum ESPRESSO results for the useful information. Most programming was done using c++ and was facilitated by the writing of two classes that would prove to be instrumental to fast and efficient programming for this project and others. These classes were a "file class" and a "coordinates class" which automated many common issues associated with preparing files and dealing with coordinates. This allowed for "black boxing" redundant code

and for efficient programming at a meta-level when dealing with files and atomic co-ordinates. Coding dealing with preparation of input files primarily revolved around preparing the interface calculations which required making surface cleaves, making the Li interface, adjusting vacuum length, and scaling fractional coordinates along the cleave to adjust for vacuum length. These tasks were facilitated by the writing of a "clever", "coordinates scaling", and "interface maker" program. Programs for post processing the Quantum ESPRESSO results dealt with averaging data, calculating standard deviations, and producing partial density of states plots for specific regions of the supercell. The code for calculation of the regional partial density of states was the most challenging programming effort of this project.

This project was completed in collaboration with my advisor Dr. N.A.W. Holzwarth whom gave me the initial task of studying the Li-ion migration paths in the materials. Dr. Holzwarth had previously done simulations of the materials Li_2SnS_3 and Li_2SnO_3 as a collaboration with the experimental researcher Dr. Brant that was already published[14] when I started this work. The structural simulations in this previously published work served as the starting point for the simulations in this work. In this work all calculations were completed by myself under the guidance of Dr. Holzwarth, aside from the charge density plots shown in Fig 7 and Fig 9 of the published work[12] which were done by Dr. Holzwarth.

2.2   Published work

The published work can be found in appendix A.

Chapter 3

First principles molecular dynamics of Li$_4$SnS$_4$

3.1 Introduction

The work in this chapter started as a collaboration between Ahmad Al-Qawasmeh, Dr. N.A.W. Holzwarth and myself. Ahmad and Dr. N.A.W. Holzwarth had already began investigating the materials Li$_4$SnS$_4$ and Li$_4$SnSe$_4$ in the context of solid state Li-ion electrolytes. Ahmad had been making structural models and finding possible Li-ion conduction pathways in the materials. Dr. N.A.W. Holzwarth had become interested in the recent developments that computing power had reached the level that first principles molecular dynamics was a possible means of studying Li-ion diffusion in materials. With Li-ion diffusion an approximation of the Li-ion conductivity was possible through the Nernst-Einstein relation. Dr. N.A.W. Holzwarth had started the process of completing molecular dynamics simulations to calculate the tracer diffusion coefficients for the Li-ions in these materials. At this point Dr. N.A.W. Holzwarth asked if I was interested in collaborating on the project. I thought this would be interesting and took up the task of testing cutoff parameters for the

molecular dynamics simulations in order to optimize the amount of simulation time while keeping a reasonable accuracy. After finding more ideal cutoff parameters my task was to perform the molecular dynamics simulations of Li_4SnS_4 while Ahmad was tasked with doing the same for Li_4SnSe_4. Along with doing the simulations for Li_4SnS_4 I spent time researching the theories behind the connection of the Li-ion tracer diffusion and Li-ion conductivity. The beginnings of these theories originated in the Brownian motion paper[15] by Einstein and later includes contribution from an experimental scientist named Dr. Haven, whom was a physics professor at Wake Forest University from 1965-1983. Einstein's Brownian motion paper gave a general equation for a diffusion coefficient in terms of mobility and temperature, this equation was in the non interacting limit of the particles. Later this equation was inverted for the mobility and expressed in terms of conductivity. This equation became known as the Nernst-Einstein equation. It was known that this equation would have a systematic error if the particle motions were correlated with each other. Dr. Haven spent time taking careful measurements of ionic conductivity and tracer diffusion coefficients to investigate the discrepancy that would occur for different materials. There is a quantity known as the Haven ratio that effectively measures the discrepancy that occurs between the measured ionic conductivity and the one calculated using the tracer diffusion coefficient in the Nernst-Einstein relation. Although the simulations in this work were not long enough to calculate the Haven ratio, understanding the principles behind the ratio helped to put the simulated results into the appropriate context.

This work lead to a publication in the Journal of the Electrochemical Society.[16] This project required some level of programming. The main programming task for this project was writing a code that would take the molecular dynamics trajectories and calculate time averaged site occupancy factors. In the published work presented in this chapter I was responsible for the molecular dynamics simulations of Li_4SnS_4,

coding the program for calculation of site occupancy factors, and helping write the molecular dynamics and conclusions sections.

3.2 Published work

The published can be found in appendix B.

Chapter 4

First principles simulations of Li$_2$OHCl

4.1 Introduction

This project started as a collaboration with the experimental chemist Zachary Hood, who at the time was working at Oak Ridge national lab and associated with Georgia Tech University. Zach Hood had recently been involved with a published project[17] cycling the solid state Li-ion electrolyte Li$_2$OHCl with lithium metal anodes. The computational research started with an effort to develop a model for the low temperature orthorhombic structure of the material. The material is known to exist in two phases, a high temperature (>310K) cubic structure and a low temperature (<310K) orthorhombic structure. The cubic phase of the material is disordered and has superior Li-ion conductivity to that of the low temperature phase. One of the goals of studying this material was to understand the phase transformation and a key to that was determining a structural model for the orthorhombic phase. Many structures were tried and a candidate orthorhombic was found that using standard structural relaxations within density functional theory had lattice parameters in rea-

sonable agreement with experiment aside from one axis that had a larger error than usual. It was hypothesized that this discrepancy may be due to non trivial phonon free energies. To test this hypothesis, the structural free energy was relaxed in the context of the quasi-harmonic phonon approximation which did improve agreement with experiment. So one of the outcomes of this research was a prediction for the detailed structure of the low temperature orthorhombic phase of Li_2OHCl. In this work the computations were aided by carefully performed experimental preparations and measurements by Zach Hood to whom much gratitude is due.

The other part of the computational work involved the use of first principles molecular dynamics to study the Li-ion diffusion properties. The published work included calculations of Li-ion conductivity from tracer diffusion coefficients assuming no correlation between the Li-ions. Comparison to experimental data revealed a large discrepancy beyond the reasoned statistical and systematic errors, this indicated a prediction of highly correlated Li-ion motion. During this work some effort was put into understanding more advanced methods to calculate Li-ion conductivity that were derived from the Kubo formalism. It was determined that the calculations did not have enough statistics to converge these quantities but the research led to another project that was started partially in parallel. Aside from calculations of the tracer diffusion coefficients the molecular dynamics were used to give a visual depiction of the hopping events that occurred on this particular lattice. The molecular dynamics simulations were also used to understand the average position of the OH group orientations.

This work was published in Physical Review Materials.[18] In the published work all simulations where completed by myself under the guidance of Dr. N.A.W. Holzwarth, and all experimental work was completed by Zachary Hood. The manuscript was written by me aside from the methods section for the experiment. Zachary Hood did help with review and improvement of the initial draft of the manuscript, in particular

the parts that compare simulations to experiment.

In this work coding was a vital aspect of its completion. While quantum ESPRESSO was used for calculation of fundamental quantities a significant amount of post processing was required. This coding including integration of the phonon density of states to calculate phonon free energies, interpolation of free energies on a grid of lattice constants using MATLAB, calculating histograms of the OH group orientations, and codes for calculation of transport coefficients from the molecular dynamics trajectories.

4.2 Published work

The published work can be found in appendix C.

Chapter 5

Kinetic Monte Carlo study of convergence properties of transport coefficients as guide to first principles molecular dynamics of Li$_2$OHCl

5.1   Introduction

This work started in parallel with the work of chapter 4. From the first principles molecular dynamics of Li$_2$OHCl in chapter 4 it was originally desired to calculate the exact dc conductivity of the lithium ions using the Kubo formalism. The question that arose during the work was whether the simulations had enough statistics to accurately converge the Kubo formalism. To answer this question a kinetic Monte Carlo code was written to help investigate the convergence properties of transport coefficients on a lattice equivalent to that of the lithium sub lattice of Li$_2$OHCl. The

kinetic Monte Carlo simulation is a greatly simplified physical model that only includes the lattice geometry and site blocking of the hopping ions. The benefit of the simplified model is the ability to reach levels of statistics not possible with first principles molecular dynamics. With these Monte Carlo simulations it was determined that for the simulations of lithium diffusion in chapter 4 that there was not enough data to converge the Kubo formalism. The work in this chapter aimed to show a careful study of the convergence properties of transport coefficients using the lithium lattice of Li_2OHCl as an example system. This work also performs some first principles molecular dynamics on Li_2OHCl and shows how the kinetic Monte Carlo simulations can be used as a reference to interpret them. The first principles simulations are limited to smaller system sizes than the previous study to allow for greater statistics. The work also provides further evidence for a prediction made of highly (anti) correlated Li-ion motion in Li_2OHCl in the previous work of chapter 4. This work has been submitted to Solid State Ionics for review.

The work of this chapter was initiated and completed by myself. This included researching and understanding the fundamental theories of kinetic Monte Carlo and transport coefficients and the writing of the code for performing the kinetic Monte Carlo simulations. Revising and editing of the first draft of the manuscript was completed in collaboration with Dr. N.A.W. Holzwarth.

5.2 Manuscript submitted

The manuscript of this work submitted for publication to Solid State Ionics can be found in appendix D.

Chapter 6

Disordered subspace approximation to the Helmholtz free energy for systems of known multiplicity: application to phase properties of Li$_2$OHCl and Li$_2$OHBr

6.1 Introduction

This work was started as an effort to understand the difference in temperature dependent phase properties of Li$_2$OHCl and Li$_2$OHBr. Both of these materials have a potential use as solid state Li-ion electrolytes. The material Li$_2$OHCl is known to exist in the low temperature ($<$310K) ordered orthorhombic phase and a high temperature ($>$310K) disordered cubic phase. The material Li$_2$OHBr is only known to

exist in a disordered cubic phase down to at least 150K. The question this work set out to answer is why is Li_2OHBr stabilized in the cubic phase down to such a low temperature. This question is important because the cubic phase is the high ionic conductivity phase. To address this question it was decided to calculate Helmholtz free energies for ordered and disordered models of the two materials and compare the relative stabilities. A difficulty of doing this for these materials is the disordered phases have a large number of possible lattice configurations which makes evaluation of the partition function non-trivial. In this work a Monte Carlo like method is proposed to evaluate the Helmholtz free energies of these systems assuming the total multiplicity of the lattice configurations is known. This method is referred to as the "disordered subspace approximation" and it is similar to Monte Carlo in that relies on randomly sampling the the configuration space. The method is advantageous because it allows for direct evaluation of the Helmholtz free energy without need for calculation of the partition function and that the lattice configuration samples can be completed entirely in parallel. The difficulties come from needing an accurate value for the total multiplicity, the ability to randomly sample the configuration space, and the need for a large number of lattice configuration samples.

This work was completed mostly independently but with conversations between Dr. N.A.W. Holzwarth and myself about the status of the project being instrumental in moving the research forward. The initial idea for the "disordered subspace approximation" came when discussing the difficulties of calculating the Helmholtz free energy for a disordered system. The work is being prepared for publication and the current state of the manuscript is now presented.

6.2 Manuscript in preparation

6.2.1 Introduction

All solid state batteries are believed to enable higher energy density and more stable/safer batteries.[19] All solid state Li-ion batteries with a metallic lithium anode will allow the highest theoretical energy density. Solid state electrolytes unlike polymer electrolytes are not flammable, leading to a safer battery. Recently two solid state materials studied for their potential use in batteries are the anti perovskite like halide materials Li_2OHCl and Li_2OHBr.[17,18,20,21] These materials have been characterized as fast ion conductors and the material Li_2OHCl has been cycled in a symmetric cell with lithium metal electrodes.[17] An interesting aspect of these materials relates to their possible phases. The material Li_2OHCl is experimentally known to exist in two phases, a disordered cubic phase ($T > 310K$) and an ordered orthorhombic low temperature phase ($T < 310K$). The cubic phase has superior ionic conductivity than the ordered phase and is the phase of interest for battery application. Interestingly the material Li_2OHBr is only known to exist in the disordered cubic phase. The question this paper tackles is what causes the difference in the phase properties between these similar materials? In this paper this question is tackled by using calculations of internal energy, configurational entropy, and phonon free energies in the harmonic approximation for disordered cubic and ordered orthorhombic structural models for the two materials.

6.2.2 Methods

The calculations in this work were completed using density functional theory[1,2] simulations using the Quantum ESPRESSO code[3] within the projector augmented wave formalism[22] and using the local density approximation[11] for the exchange and correlation. The data sets for the projector augmented wave formalism basis and projector

functions were produced with the ATOMPAW code.[4] For calculations of the phonon densities of states quantum ESPRESSO was used to perform density functional perturbation theory calculations.[23] To visualize and make figures of the crystal structures VESTA and XCRYSDEN were used.[24, 25] Post processing of the static lattice internal energies and phonon free energies was done with MATLAB.[26]

In this work a plane wave cut off $|\mathbf{k} + \mathbf{G}|^2 \leq 64$ Ry was used along with a $2{\times}2{\times}2$ shifted (0.5 0.5 0.5) k-point grid was used. For implementation of the disordered subspace approximation to the Helmholtz free energy the cutoffs were lowered to optimize computer time but retain sufficient accuracy in energy differences. For the $2{\times}2{\times}2$ supercell representations of the disordered cubic phase used in the free energy calculations a $2{\times}2{\times}2$ shifted (0.5 0.5 0.5) k-point grid was used. For the 10 atom ordered orthorhombic structure reported in a previous study[18] a $4{\times}4{\times}2$ zone centered k-point grid was used. For the new ordered structure reported in this work a $2{\times}2{\times}2$ zone centered k-point grid was used. Phonon densities of states were calculated with $4{\times}4{\times}2$ and $2{\times}2{\times}2$ zone centered q-point grids for the 10 atom and 40 atom simulation cells respectively. Phonon free energies were calculated from the phonon density of states $g(\omega)$ by

$$F_{ph} = k_B T \int_0^\infty \ln \left[2 \sinh(\frac{\hbar\omega}{2k_B T}) \right] g(\omega) d\omega \tag{6.1}$$

where k_B is Boltzmanns's constant, T is the temperature, and ω is the phonon frequency.

6.2.3 Free energy approximation

The fundamental question this paper is addressing is why does Li_2OHBr appear to only exist in the disordered cubic phase while Li_2OHCl has two definite phases. To answer this question it is desirable to perform a calculation of the Helmholtz free

energy

$$F(T) \equiv -k_B T \ln(Z) ,$$ (6.2)

where T is the temperature, k_B is Boltzmann's constant, and Z is the partition function.

For the materials in this paper which include possible configurational dependence of the static lattice internal energies and phonon free energies, the partition function is given by

$$Z = \sum_{i=1}^{\Omega} e^{-\frac{U_i}{k_b T}} Z_{hp}^i = \sum_{i=1}^{\Omega} e^{-\frac{U_i + F_{hp}^i}{k_B T}}$$ (6.3)

where Z is the partition function, Ω is the total number of possible atomic configurations, i is the ith configuration, U_i is the static lattice internal energy for configuration i, Z_{hp}^i is the harmonic phonon partition function for configuration i, and F_{hp}^i is the harmonic phonon free energy for configuration i.

The Helmholtz free energy is then given as

$$F(T) = <U_{sl}> + <F_{hp}> -TS_{\Omega}$$ (6.4)

where the average static lattice internal energy is given by

$$<U_{sl}> = \sum_{i=1}^{\Omega} U_i \frac{e^{-\frac{U_i + F_{hp}^i}{k_B T}}}{Z} ,$$ (6.5)

the average harmonic phonon free energy is given by

$$<F_{hp}> = \sum_{i=1}^{\Omega} F_{hp}^i \frac{e^{-\frac{U_i + F_{hp}^i}{k_B T}}}{Z} ,$$ (6.6)

and the configurational entropy of mixing between the Ω number lattice configurations is given by

$$S_{\Omega} = \frac{<U_{sl}> + <F_{hp}>}{T} + k_B \ln(Z) .$$ (6.7)

With the definition of entropy given by Eq. 6.7 and the definition of entropy, in terms of the total number of states $\mathcal{M}$ of a system,

$$S \equiv k_B \ln(\mathcal{M}) , \tag{6.8}$$

the effective total number of states can be defined as

$$\mathcal{M} = e^{\frac{<U_{sl}>+<F_{hp}>}{k_b T}+\ln(Z)} . \tag{6.9}$$

The exponential weights of the Boltzmann factors and the large number of configurations possible for lattice systems make direct evaluation of the partition function not feasible so some approximation is required. The first approximation considered is the fully disordered (fd) approximation that replaces the averages of the static lattice internal energy, phonon free energy, and the configurational entropy by their values in the high temperature limit. This approximation is given as

$$F_{fd}(T) = \frac{1}{\Omega} \sum_{i=1}^{\Omega} U_i + \frac{1}{\Omega} \sum_{i=1}^{\Omega} F_{hp}^i - k_b T \ln(\Omega) \geq F(T) \tag{6.10}$$

with the inequality noting that this must be greater than or equal to the the true free energy. The fully disordered free energy is only equal to the true free energy when all the $U_i + F_{hp}^i$ terms in the partition function are equal. For the cubic systems studied in this work the value of Ω can be calculated through combinatorics of the possible configurations of the lithium lattice. Considering only the combinatorics of the lithium lattice assumes the rotational configuration space of the OH groups is coupled to the lithium lattice configuration space. In the systems studied in this work there are 2 lithiums for every 3 lithium sites in a unit cell, taking s as the dimension

of a cubic supercell Ω is given as the following,

$$\Omega = \frac{(3s^3)!}{(2s^3)!(s^3)!} \ .$$

(6.11)

To build upon this approximation it is useful to imagine that if the spread in the values of $U_i + F_{hp}^i$ is large than because of the exponential nature of the Boltzmann weights the system will effectively be restricted to some subset of the entire number of configurations Ω. First by ordering $U_i + F_{hp}^i$ in ascending order

$$U_1 + F_{hp}^1 \ \leq \ ... \ \leq \ U_\mathcal{N} + F_{hp}^\mathcal{N} \ \leq \ ... \ \leq \ U_\Omega + F_{hp}^\Omega$$

(6.12)

a fully disordered subpace approximation to the free energy can be written as

$$F(T) \approx \left[\frac{1}{\mathcal{N}} \sum_{i=1}^\mathcal{N} U_i + \frac{1}{\mathcal{N}} \sum_{i=1}^\mathcal{N} F_{hp}^i - k_B T \Big\{ \ln(\Omega) + \ln(\frac{\mathcal{N}}{\Omega}) \Big\} \right]_{min \to \mathcal{N}} \ .$$

(6.13)

Where the term $\ln(\Omega)$ has been left in purposes of writing the configurational entropy in terms of the prior known value Ω, and $\mathcal{N}$ is the approximate number of configurations the configuration space is restricted to. Although Eq. 6.13 is a better approximation to the crude fully disordered approximation in principle it will not be possible to list all the states and their energies. For practical purposes is useful write Eq. 6.13 in the alternate form

$$F(T) \underset{\mathcal{S} \to \infty}{\approx} \left[\frac{1}{\mathcal{N}'} \sum_{i'=1}^{\mathcal{N}'} U_{i'} + \frac{1}{\mathcal{N}'} \sum_{i'=1}^{\mathcal{N}'} F_{hp}^{i'} - k_B T \Big\{ \ln(\Omega) + \ln(\frac{\mathcal{N}'}{\mathcal{S}}) \Big\} \right]_{min \to \mathcal{N}'}$$

(6.14)

where $\mathcal{S}$ is the number of randomly generated samples from the configuration space of the Ω total configurations, i' is the i'th prime configuration of the $\mathcal{S}$ number samples ordered from least to greatest energy $(U_i' + F_{hp}^{i'})$, and $\mathcal{N}'$ are the number of the lowest energy $(U_i' + F_{hp}^{i'})$ that minimize Eq. 6.14, and $\mathcal{N}'/\mathcal{S} = \mathcal{N}/\Omega$ as $\mathcal{S} \to \infty$.

34

6.2.4 Results

In this work density functional theory calculations were used for the calculations of the static lattice internal energies and phonon free energies. To carry out the fully disordered subspace approximation is was necessary to produce models of the disordered cubic phase. A representation of an abstract unit cell of the disordered cubic phase is shown in Fig 6.1 with more structural details found in.[18] To understand the stability of these calculations relative to the ordered phase it was necessary to have models of ordered phases for the material. In a previous study[18] a orthorhombic structure was identified that had reasonable agreement with experimental x-ray powder diffraction. A representation of this previously determined orthorhombic structure is shown in Fig 6.2. In this work a new ordered structure was found, a representation of this structure is shown in Fig 6.3. This new structure has a lower static lattice internal energy as the previously determined structure but it is not clear if it is the structure that forms in nature. For the purposes of this study both of these ordered structures will be used to understand the relative stability of the disordered phase in an effort to understand why Li_2OHBr exists in the cubic phase to such a low temperature.

To model the disordered cubic phases first an approximate lattice parameter was found by relaxing 10 randomly generated structures for each Li_2OHBr and Li_2OHCl with respect to the cubic lattice parameter. These structures where generated by randomly placing the lithiums on the available lithium sites and randomly orienting the OH groups on the 4π solid angle as described in the previous study.[18] These average lattice parameters where then used for the simulations to compute the disordered subspace approximation. For the disordered subspace approximation 1000 randomly generated structures in $2\times2\times2$ supercells were relaxed at the average lattice parameter from the previous calculation. These relaxations were completed by
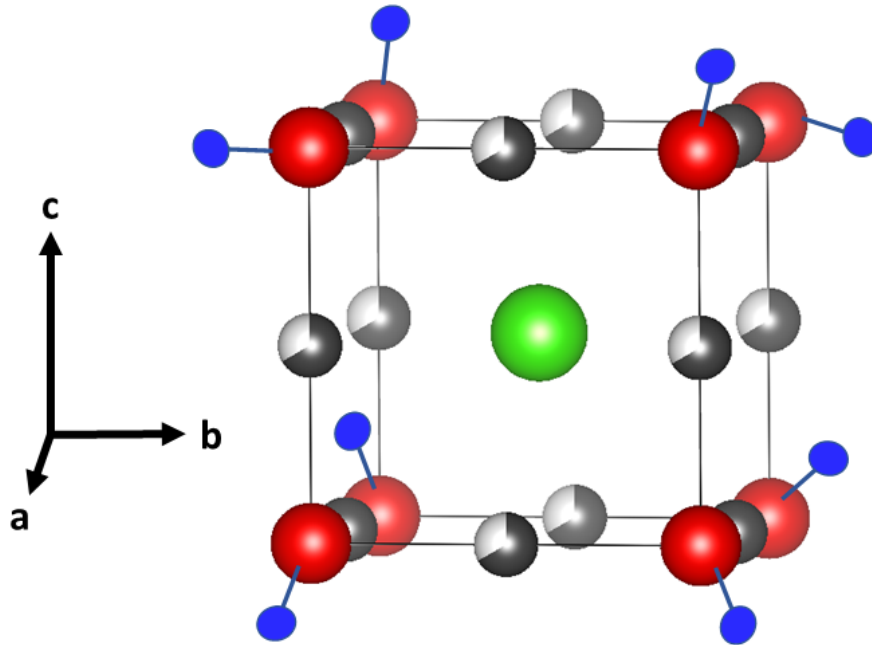
Figure 6.1: Representation of the disordered cubic structure. Red balls represent oxygen, dark and light gray balls represent fractionally occupied lithium sites, blue balls represent hydrogen, and green balls represent chlorine or bromine.
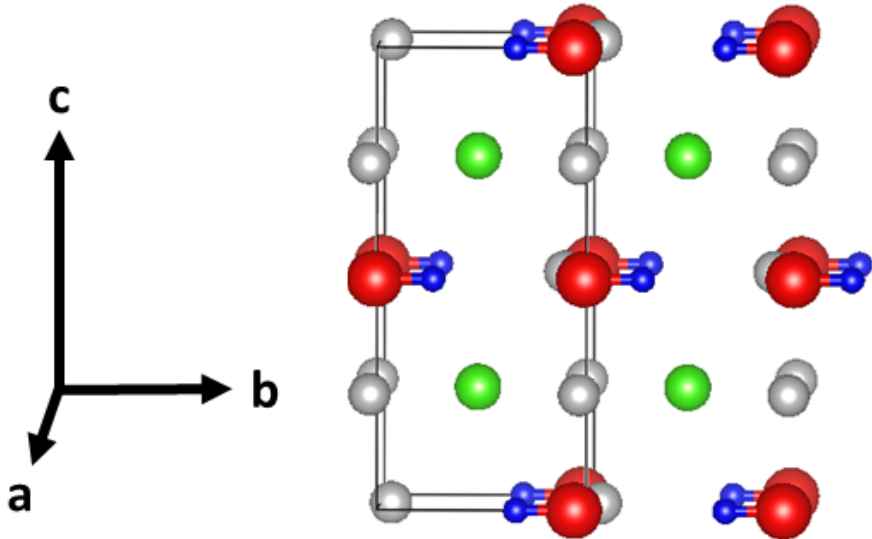

Figure 6.2: Representation of the orthorhombic structure determined in a previous study. Red balls represent oxygen, gray balls represent lithium, blue balls represent hydrogen, and green balls represent chlorine or bromine.

first fixing the lithium and relaxing the other atoms and then allowing full relaxation of all atoms. From these simulations the phonon density of states was computed
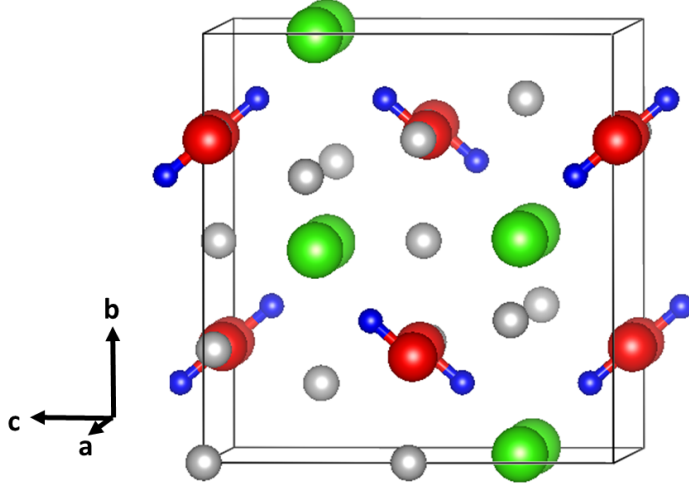
Figure 6.3: Representation of a new ordered structure identified in this work. Red balls represent oxygen, grey balls represent lithium, blue balls represent hydrogen, and green balls represent chlorine or bromine.

for the structures with the lowest 20 energies. This was done because phonon free energies vary less than the static lattice internal energies so in minimizing the disordered subspace approximation it is only necessary to calculate phonon free energies for a set of the configurations with lowest static lattice internal energies. With these calculations of the phonon density of states the phonon free energies where then computed. With this set of static lattice internal energies and phonon free energies the procedure of minimizing the disordered subspace approximation was carried out for a range of temperatures. At each temperatures the $U_i + F_{ph}^i$ terms are rearranged in ascending order and the minimization carried out. What is of interest in this work is to reference these free energy calculations to the free energies of the ordered models for the materials. The quantity of interest is

$$F_{tot}^{cubic} - F_{tot}^{ortho} = \Delta F_{tot} = \Delta F_{ph} + \Delta U - T\Delta S_\Omega \qquad (6.15)$$

which if negative indicates the cubic phase is favorable and if positive the orthorhombic phase is favorable.

The results of the simulations for Li_2OHCl are shown in Figs 6.4 (a) and (b). The results of the simulations for Li_2OHBr are shown in Figs 6.5 (a) and (b). In comparing Fig 6.4 (a) to Fig 6.5 (a) it is seen that the results predict that when referenced to the structure shown in Fig 6.2, Li_2OHCl is stable in the cubic phase for $T > 170K$ and cubic Li_2OHBr is stable for all temperatures. In comparing Fig 6.4 (b) to Fig 6.5 (b) it is seen that the results predict that when referenced to the structure in shown in Fig 6.3, Li_2OHCl is stable in the cubic phase for $T > 368$ and Li_2OHBr is stable in the cubic phase for $T > 183$. So between the two ordered reference structures used they both predict that Li_2OHBr should exist in the cubic phase at a much lower temperature ($> 170K$ lower) than Li_2OHCl. This is in agreement with the experimental finding which makes it reasonable to interpret these results for the physical reason. In examining the results in Figs 6.4 and Figs 6.5 it is predicted that the reason for Li_2OHBr existing in the cubic phase at a lower temperature is a combination of a lower ΔF_{ph} and ΔU as compared to Li_2OHCl. For referencing to the ordered structure shown in Fig 6.3 the reason for the predicted lower transition temperature is predicted to be approximately evenly distributed between the ΔU and ΔF_{ph} terms. For referencing to the structure shown in Fig 6.2 the reason for the predicted stability of the cubic phase at all temperatures for Li_2OHBr is due primarily to the ΔU term.

It should be noted that there is an expected systematic error in the calculation of the ΔF_{tot} values of at least $0.02eV$ per formula unit, which is primarily due convergence of low frequency phonon modes and not including temperature dependent lattice effects through the quasi harmonic approximation. Although the errors in in ΔF_{tot} are large it is expected that there is some error cancellation in the value of $\Delta F_{tot}^{Cl} - \Delta F_{tot}^{Br}$. The value of $\Delta F_{tot}^{Cl} - \Delta F_{tot}^{Br}$ is related to the differences in predicted

transition temperatures. In this way it is expected that results are meaningful and that it is a correct prediction that Li_2OHBr should exist in the cubic phase at a lower temperature as Li_2OHCl.

6.2.5 Conclusions

A method is suggested for calculation the Helmholtz free energy of system with many configurations and a known multiplicity. The method is successfully applied to understanding the phase properties of Li_2OHCl and Li_2OHBr. Confirmation of the experimentally known property of Li_2OHBr being stable in the cubic phase at a much lower temperature than Li_2OHCl gives confidence interpreting the results for the physical reason. The results suggest this is primarily due to a lower static lattice internal energy difference between the disordered cubic and orthorhombic ordered phases of Li_2OHBr, and also some contribution from a lower phonon free energy difference between the disordered cubic phase and ordered orthorhombic phases.
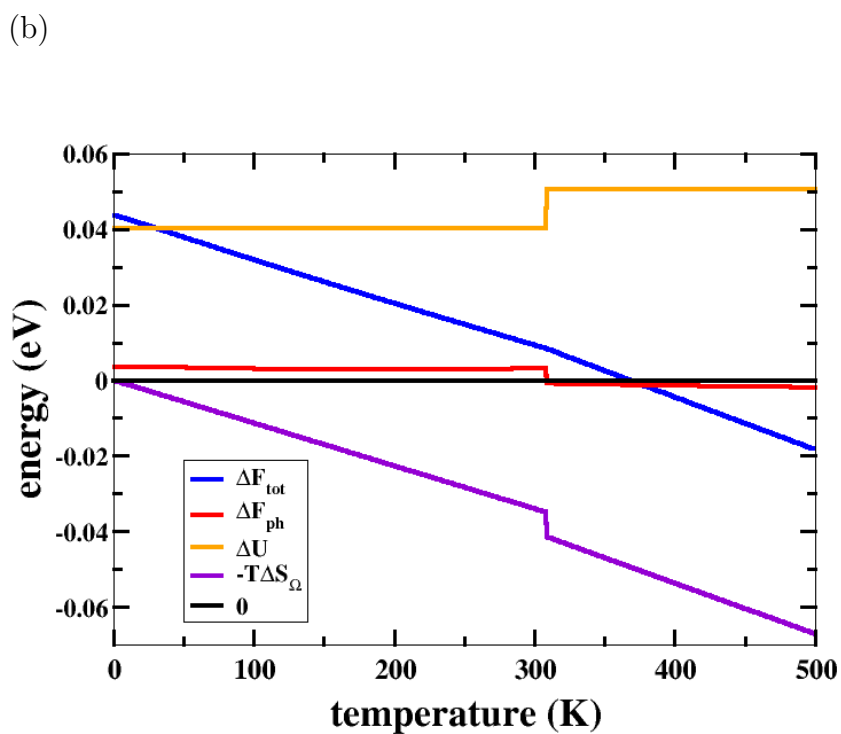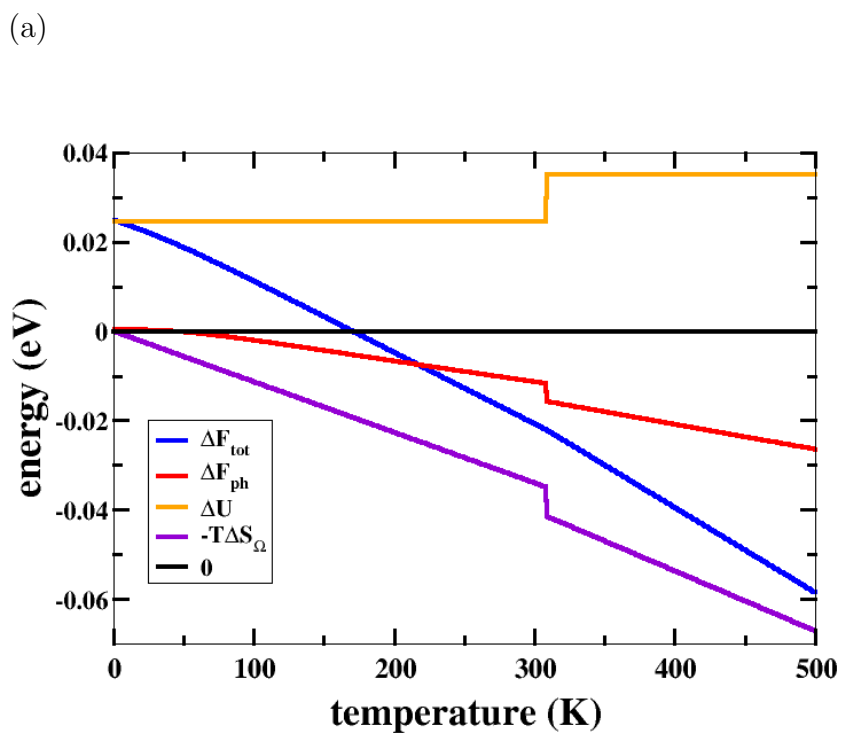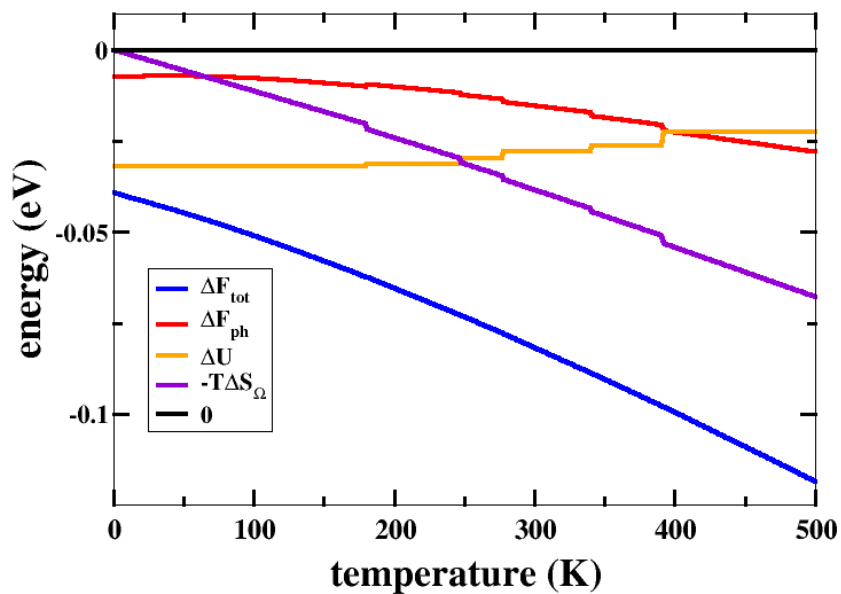
(a)

(b)

Figure 6.4: ΔF_{tot} and components for Li$_2$OHCl given per formula unit. (a) is the cubic phase referenced to the ordered structure shown in Fig 6.2 and (b) is the cubic phase referenced to the ordered structure shown in Fig 6.3.
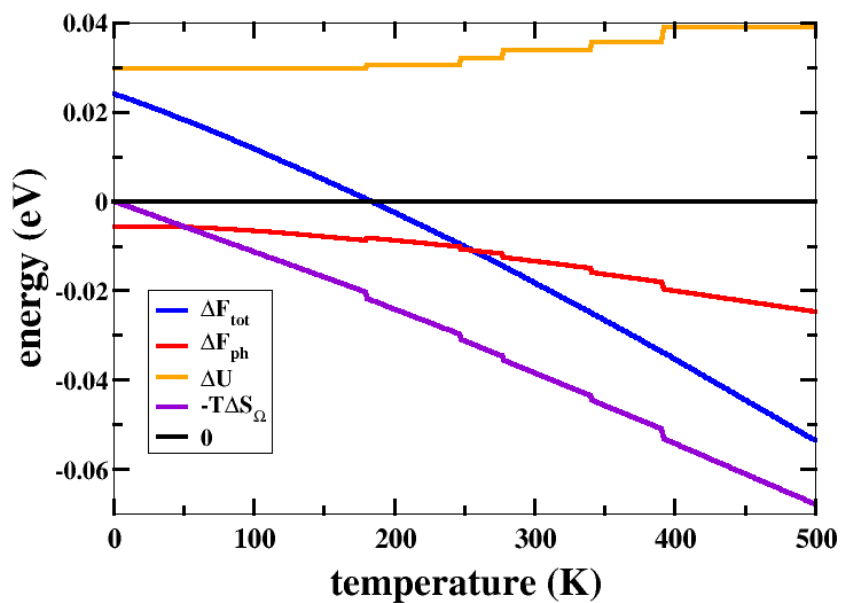
(a)

(b)

Figure 6.5: ΔF_{tot} and components for Li$_2$OHBr given per formula unit. (a) is the cubic phase referenced to the ordered structure shown in Fig 6.2 and (b) is the cubic phase referenced to the ordered structure shown in Fig 6.3.

Chapter 7

Conclusions

7.1 Conclusions

In this work first principles simulations and kinetic Monte Carlo simulations have been used to understand specific and general properties of solid state battery materials. The first principles simulations are used to accurately model real materials and provide a conceptual framework to aid in the understanding of the basic properties of these materials. In general the calculations have produced accurate structural models, accurate calculations of voltages, ionic diffusion, time averaged order parameters, and ionic correlations. The kinetic Monte Carlo simulations have provided critical insight in to the statistical and convergence properties of tracer diffusion, effective diffusion, and mobility for a lattice system.

Along with simulations of the properties of real materials some mathematical work was accomplished. The cross correlations of the effective diffusion were recast into a sum over event products which allowed for decreasing the standard deviation and to better understand the correlation in terms of time and spatial separation of the events. In an effort to understand the phase properties of disordered lattice materials a approximation to the Helmholtz free energy called the "disorderd" subspace ap-

proximation was developed. This approximation was successfully implemented in the understanding of two solid state electrolytes. This approximation is general and can be applied to any ensemble of energies (states) where the total number of energies (states) is known and can be sampled randomly. In this work the states took the form of lattice configurations.

Overall this work has provided accurate simulations of real materials and qualitative simulations of transport coefficients. These simulations are useful to the greater scientific literature because they help others understand the materials and help to understand properties of the materials difficult to understand through experiment. This work also puts forth some advancements in methodology which are hoped to assist other computational researchers.

Appendices

Appendix A

First principles simulations of $Li_{2+x}SnO_3$ and $Li_{2+x}SnS_3$

First-principles simulations of the porous layered calcogenides $Li_{2+x}SnO_3$ and $Li_{2+x}SnS_3$

Jason Howard and N. A. W. Holzwarth[*]

Department of Physics, Wake Forest University, Winston-Salem, North Carolina 27109-7507, USA
(Received 26 May 2016; revised manuscript received 14 July 2016; published 26 August 2016)

First-principles simulations of the porous layered calcogenide materials Li_2SnO_3 and Li_2SnS_3 are used to study their structures, Li ion mobilities, and their interactions with excess Li. The pristine materials are characterized by a regular pattern of voids within the calcogenide layers which are occupied by intralayer Li ions. The energetically most favorable Li ion migration processes for both materials result in a net motion perpendicular to the layers and involve intralayer Li ions and nearby interstitial sites. The ideal lattice has eight symmetry related stable interstitial sites within the conventional unit cell which, in addition to participating in the Li ion migration processes, are also important for accommodating excess Li during lithiation processes. Consistent with experimental findings, the simulations find that the addition of Li atoms to Li_2SnO_3 results in a disruption of the calcogen lattice with the breaking of Sn-O bonds. The estimated voltage versus bcc Li for this system is in qualitative agreement with experiment provided that Sn/Li disorder is taken into account. By contrast, the simulations predict that the addition of Li atoms to Li_2SnS_3 results in a stable metallic material up to a stoichiometry of Li_3SnS_3. This prediction has not yet been studied experimentally. Simulations of surfaces of these materials find that it is energetically favorable to add a small amount of excess surface Li. However, interfaces of these materials with Li metal are found to be reactive. Some of the findings may be relevant to other materials having the same crystal structure such as Li_2MnO_3 and Li_2TiO_3.

I. INTRODUCTION

Efficient ionic conductivity in crystalline materials depends on a delicate balance of structural, chemical bonding, and charge transfer factors. The study of Li ion conduction in Li_2SnO_3 and Li_2SnS_3 provides an interesting example of these factors with possible implications for a variety of technologies including solid state batteries.

The crystal structure of Li_2SnO_3 and Li_2SnS_3 is related to the structure of layered dichalcogenides such as SnS_2 [1]. A patterned layer of the calcogenide is constructed by systematically removing one-third of the Sn atoms within a layer of SnS_2, leaving star-shaped voids. Filling these voids with Li results in a structure similar to the corresponding layers in Li_2SnO_3 and Li_2SnS_3, as shown in Fig. 1. In SnS_2 each calcogen is bonded to three Sn atoms, while the void pattern in $Li_2Sn(O/S)_3$ allows for each calcogen to be bonded to two Sn atoms. As will be discussed in more detail in Sec. III, the full structure of $Li_2Sn(O/S)_3$ includes a particular stacking of the layers and the placement of interlayer Li sites [2–4]. Interestingly, a number of other Li ion conducting materials have this same structure including Li_2MnO_3 and Li_2TiO_3 [5,6].

The conductivity of Li ions in Li_2SnO_3 has been measured to be very small (10^{-8} S/cm at 290° C), although the activation barrier for conduction is in a reasonable range [7]. One of the interesting proposed uses for Li_2SnO_3 is as an anode material for lithium ion batteries [8–10]. The mechanism involves the material undergoing an irreversible decomposition during the first lithiation of the material forming a composite of Li_2O and Li_xSn. Li_2O serves to buffer the volume expansion of the active anode material Li_xSn. Li_2SnO_3 is among other tin based electrode materials with a similar mechanism such as SnS_2, SnO, and SnO_2 [8,11,12]. By contrast, Brant *et al.* [4]

showed that Li_2SnS_3 has good ionic conductivity (10^{-5} S/cm at 25° C). The lithiation properties of Li_2SnS_3 have not yet been studied.

The purpose of the present study is to computationally examine both Li_2SnO_3 and Li_2SnS_3 in order to understand the mechanisms for Li ion migration, the lithiation processes, and the interface properties. The remainder of the paper is organized as follows. Section II details the computational methods used in this work. Structural details are presented in Sec. III while Li ion migration in the stoichiometric materials are presented in Sec. IV. Models of the lithiation processes are presented in Sec. V and interfaces with vacuum and with Li metal are discussed in Sec. VI. Section VII contains the discussion and conclusions. Some of the structural details are given in the appendix.

II. METHODS

The computational methods used in this work were based on density functional theory [13,14] implemented with the projector augmented wave formalism (PAW) [15]. The PAW atomic data sets were calculated using the ATOMPAW code [16] and the materials simulations were performed using the QUANTUM ESPRESSO software package [17]. The local density approximation exchange correlation functional (LDA) [18,19] was used throughout all calculations. The minimum energy path for Li ion migration was estimated using the "nudged elastic band" (NEB) method [20–22] as programmed in the QUANTUM ESPRESSO package, using five images between each metastable configuration. In modeling charged defects (Li ion vacancies or interstitials), the system was assumed to remain electrically insulating and a uniform background charge was added in order to evaluate the electrostatic interactions. The partial density of states $\langle N^a(E) \rangle$ were calculated as described in previous work [23,24], using weighting factors based on the charge within the augmentation spheres of each atom with radii
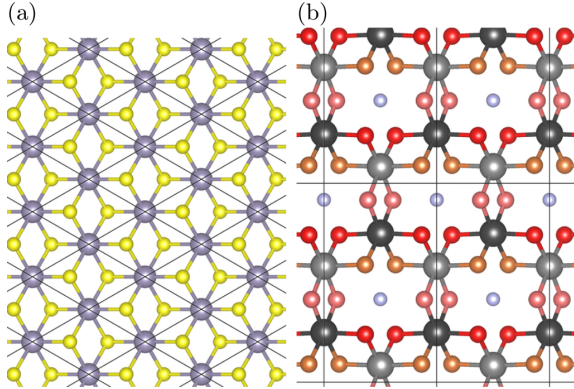
*natalie@wfu.edu

064108-1

FIG. 1. (a) Planar projection of ball and stick model of a single layer of SnS_2 with gray and yellow balls representing Sn and S, respectively. Lines indicate the two-dimensional (hexagonal) unit cells. (b) Planar projection of ball and stick model of a single layer of Li_2SnO_3, excluding the interlayer Li sites. This structure has two inequivalent Sn sites indicated with two shades of gray, three inequivalent O sites indicated with three shades of red, orange, and pink, and one Li inequivalent intralayer Li site indicated with light blue. Lines indicate the boundaries of the two-dimensional unit cells.

$r_c^{Li} = 1.6, r_c^{Sn} = 2.3, r_c^O = 1.2$, and $r_c^S = 1.7$ in bohr units. The reported $\langle N^a(E) \rangle$ curves are averaged over all sites of type a. The isosurfaces of electron density were computed using the PWPAW code [25] and visualized using OPENDX [26]. Structural visualizations used the XCRYSDEN code [27,28] and the VESTA code [29].

Integrals over the Brillouin zone used a Gaussian smearing factor of 0.001 Ry and a uniform grid of $4 \times 2 \times 2$ Bloch vectors **k** for the conventional unit cells. Supercell simulations used consistent **k**-point sampling. For evaluating the partial densities of states, the **k**-point sampling was increased by a factor of 2 in each dimension. The plane wave expansions of the electron wave functions included reciprocal lattice vectors **G** such that $|\mathbf{k} + \mathbf{G}|^2 \leqslant 64$ bohr^{-2}. Most of the defect studies were modeled using $2 \times 1 \times 1$ supercells. Spot checks of finite size errors show them to be approximately 0.02 eV for the NEB calculations and for the relative energies of point defects.

III. STRUCTURE

The crystal structures of Li_2SnO_3 [2] and Li_2SnS_3 [4] are very similar, both having the centered monoclinic space group C2/c (No. 15 as listed in the International Table of Crystallography [30]). The materials are layered in the a-b planes with an A-B stacking sequence. The A and B layers are geometrically equivalent but differ by an inversion. Visualizations of the structure are shown in Fig. 2 from two different perspectives. The layered structure of Li_2SnS_3 was described by Kuhn $et\ al.$ [3] as $Li[Li_{\frac{1}{3}}Sn_{\frac{2}{3}}S_2]$, with the outer Li representing the planes of Li and the inner bracket representing the layers of the complex of tin sulfide plus Li. Using this same notation Li_2SnO_3 can be described as $Li[Li_{\frac{1}{3}}Sn_{\frac{2}{3}}O_2]$.

The crystal axes and angle are labeled a, b, c, and β. Computational and experimental results for lattice parameters
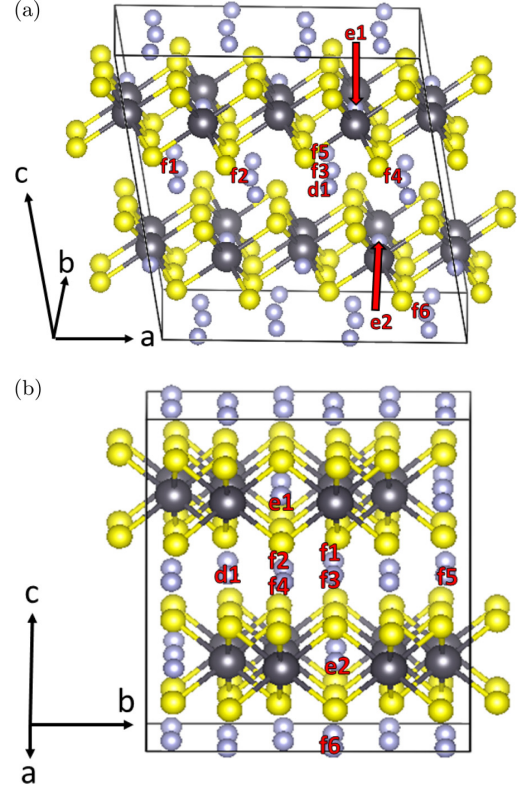

FIG. 2. Ball and stick model of Li_2SnS_3 with lithium light gray, tin dark gray, and sulfur yellow. Site labels d_i, f_i, and e_i reference possible lithium vacancy conduction pathways with the letter being the Wyckoff label. (a) and (b) Show different viewpoints as labeled by the corresponding axes to the left. This figure is geometrically representative of Li_2SnO_3 as well.

are listed in Table I. When scaled by 1.02 to compensate for the systematic LDA lattice contraction, the calculated results agree well with the experimental measurements. The fractional coordinates for the structures are presented in Appendix A. The electronic structures including band structures and densities of states were previously reported [4].

TABLE I. Computational and experimental lattice parameters for Li_2SnO_3 and Li_2SnS_3. Experimental results for Li_2SnO_3 and Li_2SnS_3 are from Refs. [31] and [4], respectively.

	Lattice(Å,°)	Comp.	Expt.
Li_2SnO_3	a	5.22	5.3033(2)
	b	9.06	9.1738(3)
	c	9.78	10.0195(2)
	β	100.31°	100.042(2)°
Li_2SnS_3	a	6.30	6.3964(5)
	b	10.91	11.0864(9)
	c	12.15	12.405(1)
	β	99.94°	99.867(5)°

TABLE II. Relative energies (in eV) of lithium ion vacancies with the zero of energy set to the lowest energy vacancy for each material calculated in a $2 \times 1 \times 1$ supercell. The site labels refer to the Wyckoff letters for the distinct Li sites.

Material	d site	f site	e site
Li_2SnO_3	0.11	0.09	0
Li_2SnS_3	0	0	0.35

In preparation for studying Li ion conduction and lithiation in these materials, the energies of relaxed ideal point defects in $2 \times 1 \times 1$ supercells were studied. Table II lists the relative energies of the inequivalent Li ion vacancies. It is of interest to note that the most favorable vacancy in Li_2SnO_3 is located at an e site while in Li_2SnS_3 the e site is the location of the least energetically favorable vacancy. Interstitial defects were also studied. In a search of the void regions of the crystal, only one unique site for a stable interstitial defect was found in each material. Within the conventional cells, the interstitial sites have multiplicity and Wyckoff label 8f and are located at the fractional coordinates (0.066, 0.093, 0.425) and (0.062, 0.086, 0.430) for Li_2SnO_3 and Li_2SnS_3, respectively. In both materials, the interstitial sites are located near the Li e sites of the host lattice, displaced along the c axis above and below the $[Li_{\frac{1}{3}}Sn_{\frac{2}{3}}(O/S)_2]$ layers.

The literature has identified several other defects in both materials [3,4,31,32]. These defects include Li/Sn antisites and stacking faults. These defects can be important factors in both Li ion migration and lithiation processes.

IV. ION MIGRATION

Li ion conductivity has been experimentally measured for stoichiometric Li_2SnO_3 and Li_2SnS_3 [4,7]. The conductivity can be modeled by an Arrhenius relationship in the form of Eq. (1):

$$\sigma = \frac{A}{T} e^{-E_a/kT}. \tag{1}$$

In this equation A is a constant, T the temperature in Kelvin, k the Boltzmann constant, and E_a the activation energy for Li ion conduction. The activation energy E_a is a parameter that is determined experimentally by analyzing the temperature dependence of the conductivity and can be theoretically approximated through Eq. (2):

$$E_m \leqslant E_a \leqslant E_m + \frac{E_f}{2}. \tag{2}$$

The migration energy E_m is the lowest energy barrier for Li ion conduction approximated using NEB calculations. The formation energy E_f is the energy of creating a vacancy interstitial pair calculated using Eq. (3), with E_{defect} and $E_{perfect}$ being total density functional energies in equivalent supercells of the structurally relaxed vacancy interstitial pair and the perfect crystal, respectively:

$$E_f = E_{defect} - E_{perfect}. \tag{3}$$

In Eq. (2) the lower limit represents the "intrinsic" case where the material has a large population of native vacancy interstitial

defects and the upper limit represents the "extrinsic" case where material has few native vacancy interstitial defects [33]. Additionally, real materials can have other defects such as Li/Sn antisite defects and stacking faults which can be detected by x-ray analysis. For the case of Li_2SnO_3, several samples were studied by Teo *et al.* [7]. The sample with the lowest E_a and highest conductivity had the sharpest and most complete diffraction peaks. This indicates that this sample is relatively free of these Sn/Li antisite and stacking fault defects [31].

In computationally determining E_m for the vacancy mechanism, suitable pathways were chosen along the main axes of the $2 \times 1 \times 1$ supercell. Two pathways corresponded to migration in the a-b plane in the Li layers between the main $[Li_{\frac{1}{3}}Sn_{\frac{2}{3}}(O/S)_2]$ layers of the material, while the other was a spiral along the c axis through the $[Li_{\frac{1}{3}}Sn_{\frac{2}{3}}(O/S)_2]$ layers. Geometrically identical pathways were investigated in the two materials using the vacancy labels shown in Fig. 2. The paths in the figure are labeled by their Wyckoff label and numeric identifier. Table II gives the relative energies for the vacancies on the Li site types. The results for the NEB calculations showing the energy landscape connecting the images for the relaxed vacancy configurations are displayed in Fig. 3. The desired quantity from these plots is E_m and it is found by searching for the path with the lowest energy difference between highest and lowest energy along the path. The results for vacancy migration in Li_2SnS_3 are relatively large with migration barriers of 0.6–0.7 eV for all of the paths. By contrast Li_2SnO_3 shows an interesting result of having $E_m = 0.3$ eV along the c axis while the other paths have $E_m = 0.8$–0.9 eV.

In this study, no viable pure interstitial conduction mechanisms were found. On the other hand several viable interstitialcy [34] mechanisms were found; the most favorable path is shown in Fig. 4. An interstitialcy mechanism is one in which an interstitial ion moves into a host lattice site as that host lattice ion moves to an adjacent interstitial location. In Fig. 4 the two unique steps of the path are labeled as "a" and "b" and shown from two viewpoints. In the "a" step, an interstitial ion moves onto a host e site as that e-site ion moves to the neighboring interstitial site. In the "b" step, the interstitial ion moves to the nearest host d site as that d-site ion moves to the nearest interstitial site. It is the "a" step that allows the Li ion to move through the $[Li_{\frac{1}{3}}Sn_{\frac{2}{3}}(O/S)_2]$ layers. The results for the NEB calculations in Fig. 4 show that for both Li_2SnO_3 and Li_2SnS_3, this interstitialcy mechanism is the most favorable mode of Li ion conduction. The E_m values for this most favorable interstitialcy mechanism is 0.14 eV for Li_2SnO_3 and 0.22 eV for Li_2SnS_3. Interestingly the "a" step in this process has a markedly smaller barrier than the "b" step for Li_2SnO_3, while for Li_2SnS_3 both steps have approximately the same barrier. The other less favorable interstitialcy mechanisms had E_m values of 0.46 eV for Li_2SnO_3 and 0.59 eV for Li_2SnS_3. These mechanisms had equivalent "a" steps as in Fig. 4 but the "b" step was different by the involvement of host f-site ions moving to neighboring interstitial sites.

To compare the most favorable E_m for the vacancy and interstitialcy mechanisms with experiment, the inequality in Eq. (2) is used. To estimate the interstitial-vacancy pair formation energy E_f, Eq. (3) is used. E_{defect} is determined from metastable configurations of a host lattice Li ions displaced
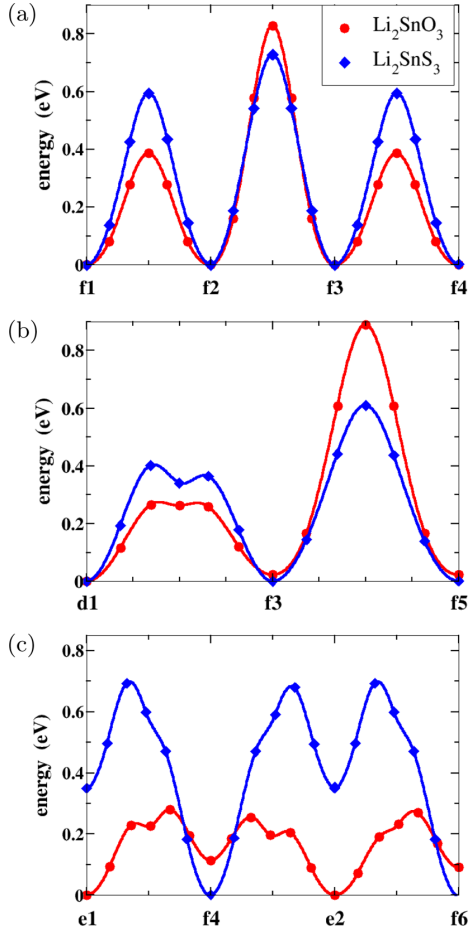
FIG. 3. Energy path diagrams for vacancy migration calculated using NEB with Li_2SnO_3 (red) and Li_2SnS_3 (blue). Path labels refer to the site labels in Fig. 2. The zero of energy for each curve has been set to the lowest energy of that path. Migrations along the a, b, and c axes are shown in plots (a), (b), and (c), respectively.

into an interstitial site. From these results, the lowest E_f for a vacancy interstitial pair was 1.25 eV for Li_2SnO_3 and 0.96 eV for Li_2SnS_3. If a large population of defects is present in the material, it is expected for E_a to be closer to E_m, while if very few are present E_a is expected to be closer to $E_m + \frac{E_f}{2}$. The results are listed in Table III. The experimental values of E_a for both samples are best explained by the interstitialcy mechanism using the upper limits of Eq. (2). This infers that these samples have a small number of native vacancy-interstitial defects.

V. LITHIATION

A. Geometrical structures

Several authors have studied lithiation of Li_2SnO_3 [8–10] and have shown lithium can be absorbed into the material. Experimental lithiation of Li_2SnS_3 has not been reported in
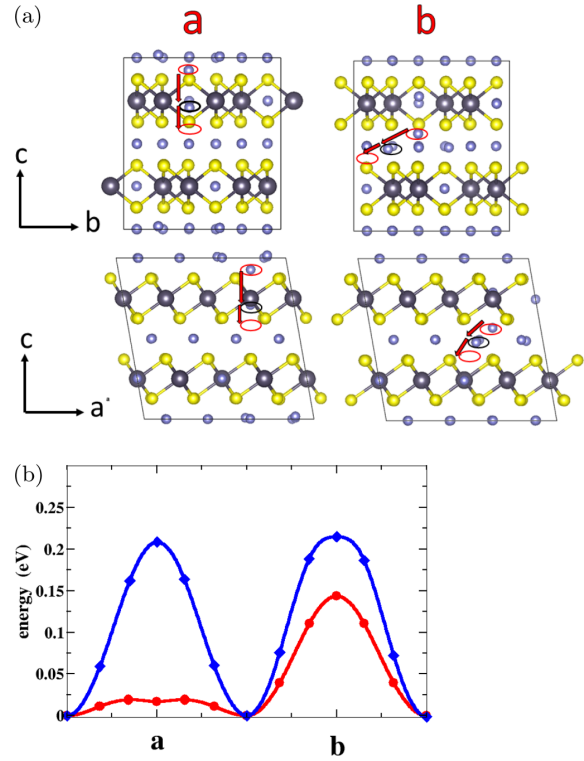

FIG. 4. (a) Ball and stick model for the interstitialcy Li ion conduction mechanism in Li_2SnS_3 using the same ball conventions as in Fig. 2. This figure is geometrically representative for the same conduction mechanism in Li_2SnO_3. (b) Energy path diagrams for interstitalcy Li ion migration using red for Li_2SnO_3 and blue for Li_2SnS_3. The labels a and b above the diagrams in (a) and the path labels in (b) refer to the two unique steps of this interstitialcy mechanism.

the literature. In order to model a possible mechanism of the lithiation for Li_2SnO_3 and Li_2SnS_3, a bulk intercalation process was assumed. This process involved placing excess lithium in the lattice of interstitials given by the coordinates in Sec. III. There are eight interstitial sites per conventional cell.

TABLE III. Calculated lower an upper bound for E_a from Eq. (2) using the most favorable E_m for the vacancy and interstitialcy mechanisms along the indicated axis. Listed experimental results are from Refs. [7] and [4], respectively. All energies given in eV.

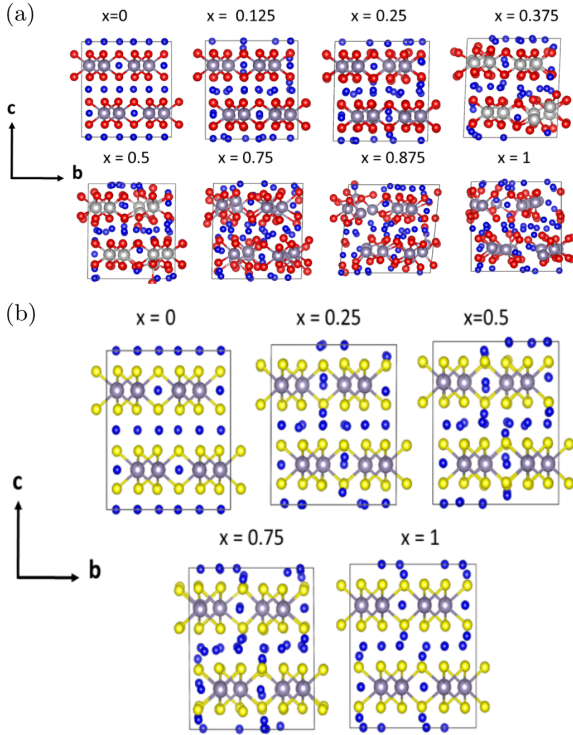| Li_2SnO_3	E_m	E_a	$E_m + \frac{E_f}{2}$
Vacancy (c axis)	0.28	$\leqslant E_a \leqslant$	0.91
Interstitialcy (c axis)	0.14	$\leqslant E_a \leqslant$	0.77
Experiment		0.69–0.91	
Li_2SnS_3	E_m	E_a	$E_m + \frac{E_f}{2}$
Vacancy (b axis)	0.61	$\leqslant E_a \leqslant$	1.07
Interstitialcy (c axis)	0.22	$\leqslant E_a \leqslant$	0.68
Experiment		0.59	

FIG. 5. Ball and stick models of optimized structures for $Li_{2+x}SnO_3$ in (a) and $Li_{2+x}SnS_3$ in (b) for indicated values of x. Li, Sn, O, and S are represented by blue, gray, red, and yellow balls, respectively.
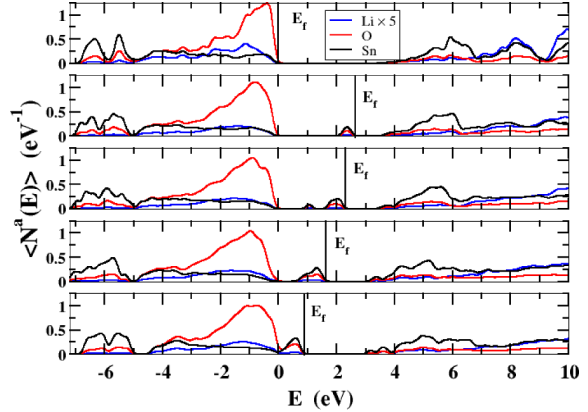

FIG. 6. Partial density of states for $Li_{2+x}SnO_3$ with the zero of energy set to the top of the occupied valence band of the pure material. In addition to the partial density of states for the perfect crystal, a sample of results for $x = 0.25, 0.5, 0.75$, and 1.0, calculated within the $2 \times 1 \times 1$ supercell, are presented in separate panels. For visibility, the lithium curves were scaled by a factor of 5.

Initially a random sampling of configurations of lithium placed in the interstitial sites for $2 \times 1 \times 1$ supercells were optimized with full structural relaxations for $0 \leqslant x \leqslant 1$ in $Li_{2+x}Sn(O/S)_3$. The limit $x = 1$ corresponds to filling all available interstitial sites defined for the perfect lattice. A sample of these configurations over the concentration range is shown in Fig. 5. It is shown in Fig. 5(a) that $Li_{2+x}SnO_3$ gradually becomes disordered as x increases. Qualitatively the material could be described as experiencing an amorphous transition at $x \approx 0.75$, which is consistent with the findings of Zhang *et al.* [9] who show that $Li_{2+x}SnO_3$ loses its diffraction peaks in the range $0.75 \lesssim x \lesssim 5$. Figure 5(b) shows that the computed model of $Li_{2+x}SnS_3$ is stable up to $x = 1$. Analysis of the change in cell parameters is given in Appendix B. The lattice of $Li_{2+x}SnO_3$ expands monotonically with concentration along all axes for $0 \leqslant x < 0.5$. For $0.5 \leqslant x \leqslant 1$ the expansion continues to be monotonic but there is a large variability in the cell parameters. The lattice of $Li_{2+x}SnS_3$ expands monotonically across all axes for $0 \leqslant x \leqslant 1$ with relatively small variability in the results due to Li configurations.

B. Electronic structures

Partial density of states calculations in the range $0 \leqslant x \leqslant 1$ are shown in Figs. 6 and 8. The partial density of states

for $x = 0$ for both materials agree with those presented by Brant *et al.* [4] While the calculational methods are known to underestimate the energies of the band gaps, the relative energies are expected to be well represented.

Pristine Li_2SnO_3 is found to have a relatively large band gap (roughly 4 eV). For $x > 0$, an occupied impurity-like band appears within the original band gap for $Li_{2+x}SnO_3$. The impurity band moves towards the top of the valence as x increases, as shown in Fig. 6.

In order to get a better idea of the nature of the "gap states" in $Li_{2+x}SnO_3$, an example of a $x = 0.25$ configuration within the conventional cell was modeled and the results are shown in Fig. 7. Isosurfaces of the electron density associated with
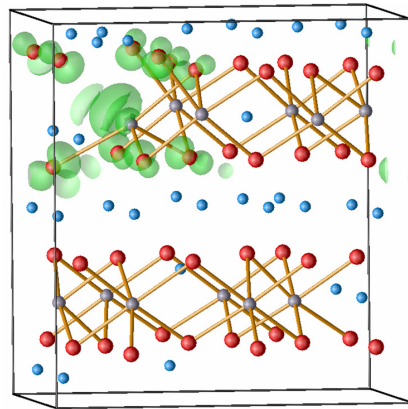

FIG. 7. Ball and stick diagram of an orthorhombic section of a unit cell of $Li_{2.25}SnO_3$ with Li, Sn, and O indicated with blue, gray, and red balls, respectively. Isosurfaces bounding the $0.1e/\text{Å}^3$ density level of the states associated with the excess electrons are indicated in green. The orientation is similar to that of Fig. 2(b).
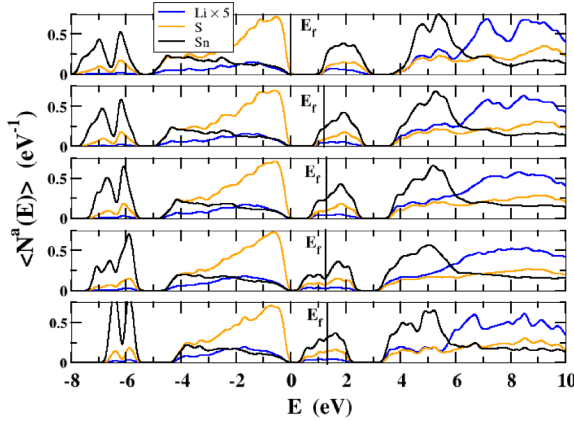
FIG. 8. Partial density of states for $Li_{2+x}SnS_3$ with the zero of energy set to the top of the occupied valence band of the pure material. In addition to the partial density of states for the perfect crystal, a sample of results for $x = 0.25, 0.5, 0.75$, and 1.0, calculated within the $2 \times 1 \times 1$ supercell, are presented in separate panels. For visibility, the lithium curves were scaled by a factor of 5.

the occupied intercalation states are shown. In this case, the intercalation density is localized primarialy on O sites near one of the Sn sites which has a broken Sn-O bond.

By contrast, pristine Li_2SnS_3 is found to have a small band gap (roughly 1 eV), due to unoccupied conduction bands formed from the hybridization of Sn $5s$ and S $3p$ orbitals. For $x > 0$, the excess electrons of $Li_{2+x}SnS_3$ occupy the available conduction states with little change in the shapes of the partial densities of states curves, as shown in Fig. 8.

Figure 9 illustrates the isosurfaces for the excess electron charge density in $Li_{2+x}SnS_3$ for two selected configurations at $x = 0.5$ and $x = 1.0$ in the conventional cell. The form of the isosurfaces is consistent with an antibonding hybridization of the Sn $5s$ and S $3p$ states that make up the conduction band.
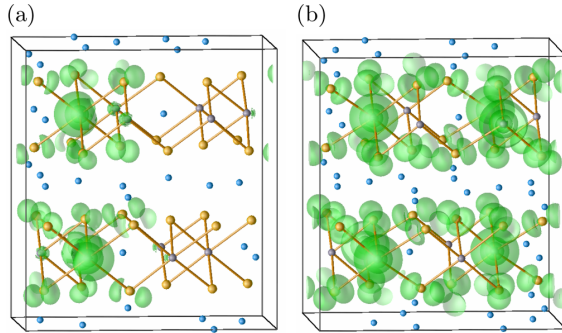

FIG. 9. Ball and stick diagrams of an orthorhombic section of unit cells of $Li_{2.5}SnS_3$ (a) and Li_3SnS_3 (b), with Li, Sn, and S indicated with blue, gray, and yellow balls, respectively. Isosurfaces bounding the $0.03 e/Å^3$ density level of the states associated with the excess electrons are indicated in green. The orientation is similar to that of Fig. 2(b).

In the $x = 1$ case the isosurfaces for the two layers are related by an inversion consistent with the symmetry of the lattice.

C. Voltage profiles

The average open cell voltage of the compound $Li_{2+x}Sn(O/S)_3$ lithiated with x Li ions per formula unit versus bcc lithium metal can be approximated by [35]

$$V_{avg}(x) = \frac{-\Delta E}{x} = \frac{\int_0^x dx' V_{obs}(x')}{x}. \quad (4)$$

For computational reasons, it is convenient to calculate the averaged voltage between the two intercalation limits $Li_2Sn(O/S)_3$ and $Li_{2+x}Sn(O/S)_3$ and Eq. (4) can be used to relate the result to an experimental voltage $V_{obs}(x)$. The approximation assumes that the internal energy difference ΔE is a good approximation to the Gibbs free energy difference ΔG where $\Delta G = \Delta E + P\Delta V - T\Delta S$. This implies that $P\Delta V$ and $T\Delta S$ as small compared with ΔE. We further approximate ΔE by its value at $T = 0$ K.

In practice, for a given value of x there are many possible configurations (σ) of the lithium interstitials. Each of these configurations will have a configuration dependent internal energy difference $\Delta E_\sigma(x)$ given by

$$\Delta E_\sigma(x) = E^\sigma_{Li_{2+x}Sn(O/S)_3} - E_{Li_2Sn(O/S)_3} - x E_{Li_{bcc}}. \quad (5)$$

The internal energy difference of the system can be determined by averaging over all of the configurations,

$$\Delta E(x) = \sum_\sigma \Delta E_\sigma(x) P_\sigma(x), \quad (6)$$

where $P_\sigma(x)$ denotes the probability of any given configuration σ at Li concentration x.

Open cell voltages are equilibrium processes so the probabilities can be approximated by a Boltzmann distribution at temperature T:

$$P_\sigma(x) = \frac{e^{-\Delta E_\sigma(x)/kT}}{Z(x)} \quad \text{where} \quad Z(x) = \sum_\sigma e^{-\Delta E_\sigma(x)/kT}. \quad (7)$$

Here k denotes the Boltzmann constant and $Z(x)$ denotes the partition function. In practice, it is difficult to sample enough configurations to evaluate the probabilities in Eq. (7) using first principles alone. However, qualitative information is readily available from samples of the configuration and concentration dependent voltages $V_\sigma(x)$ defined as

$$V_\sigma(x) = -\frac{\Delta E_\sigma(x)}{x}, \quad (8)$$

and presented in Figs. 10 and 11. In Fig. 10, the simulations were done using $2 \times 1 \times 1$ supercells. For each concentration x with $0.0625 < x < 1$, two randomly chosen configurations σ were computed. For $x = 0.0625$ and $x = 1$ only one unique configuration is possible for these supercells. Figure 11 includes results from a variety of supercells. The results for $0.0625 < x \leqslant 0.5$ all had their initial configurations chosen randomly aside from the special case of $V_\sigma(x = 0.25) = 0.53$ V.

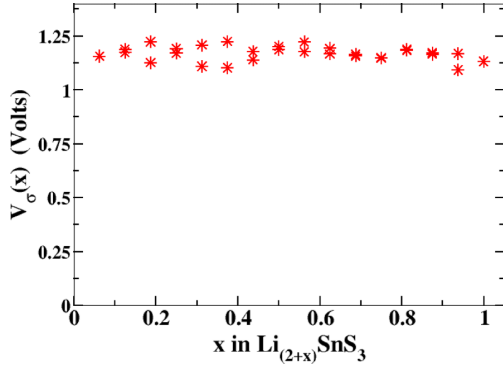Due to its stable interstitial lattice, to interpret the results for $Li_{2+x}SnS_3$, the ideas of cluster expansion [36] can be used. The

FIG. 10. Sampling of $V_\sigma(x)$ calculated with Eq. (8) for $Li_{2+x}SnS_3$.

idea of a cluster expansion is to expand $\Delta E_\sigma(x)$ over a set of configuration variables $\sigma_i..\sigma_k$ and effective cluster interactions $E_{i..k}$ as in Eq. (9):

$$\Delta E_\sigma(x) = \sum_i E_i \sigma_i + \sum_{i,j} E_{ij}\sigma_i\sigma_j + \sum_{i,j,k} E_{ijk}\sigma_i\sigma_j\sigma_k.... \quad (9)$$

The E_i, E_{ij}, and E_{ijk}... terms represent the lattice site, pairwise interaction, and three site interactions, respectively. For this system, the E_i terms are all equivalent due to the interstitial sites being geometrically equivalent. If the E_i terms are concentration independent and if higher order terms $E_{i..k}$ are small, then $\Delta E_\sigma(x)$ can be approximated by Eq. (10):

$$\Delta E_\sigma(x) \approx \sum_i E_i \sigma_i \propto x E_i. \quad (10)$$

This implies that a plot of $V_\sigma(x)$ will be approximately constant over x and σ. The plot in Fig. 10 shows this behavior so we can infer that in $Li_{2+x}SnS_3$ the lattice site interaction is concentration independent and is large compared to the pairwise and higher interactions. For this constant voltage case, we can predict that the measured voltage will be $V_{obs}(x) \approx 1.2$ V.

While there has apparently not yet been an experimental measurement of the intercalation voltage of $Li_{2+x}SnS_3$, there have been several measurements of the intercalation voltage
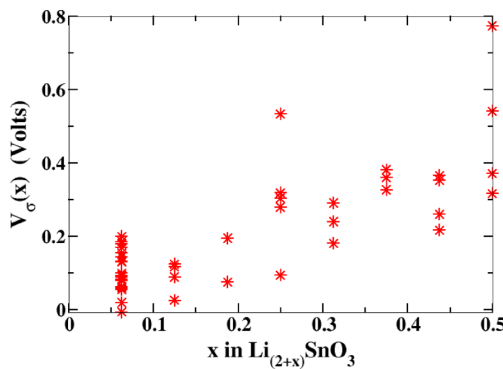

FIG. 11. Sampling of $V_\sigma(x)$ calculated with Eq. (8) for $Li_{2+x}SnO_3$.

of $Li_{2+x}SnO_3$ reported in the literature [8–10]. The literature results find $V_{obs}(x)$ to be a *decreasing* function of x with $V_{obs}(x)$ varying from ~1.0 V to ~0.4 V for $0 \leqslant x \leqslant 0.5$. By contrast, the simulation results for the concentration and configuration dependent voltages $V_\sigma(x)$ shown in Fig. 11, together with Eqs. (4) and (6), indicate that the intercalation voltage for $Li_{2+x}SnO_3$ is predicted to be an *increasing* function of x.

Some details of this apparent discrepancy between the simulation results and experiment are as follows. For $Li_{2+x}SnO_3$ the limits of x for the voltage calculations were restricted to $0 \leqslant x \leqslant 0.5$. This was done because the breakdown of the lattice makes the voltage approximation less applicable due to increasing entropy and that as the system becomes disordered the configurational space becomes much larger. Even for the $0 \leqslant x \leqslant 0.5$ range, the lattice of interstitials can be described as metastable, so that an analytic cluster expansion [36] such as given in Eq. (9), is not well defined for $Li_{2+x}SnO_3$. For the calculated range of $0 \leqslant x \leqslant 0.5$ seen in Fig. 11, the results must be analyzed qualitatively keeping in mind that results higher in voltage for a particular x are more probable. Estimating the concentration and configuration averaged voltage from $V_\sigma(x)$ given in Fig. 11 shows that the simulations predict a voltage which increases with x. For $0 \leqslant x \leqslant 0.5$, the voltage can be estimated as roughly 0.1 V $\lesssim V_{avg}(x) \lesssim 0.6$ V. It is notable that at the low concentration of $x = 0.0625$, the voltage is predicted to be ~0.9 V below that of experiment. In order to thoroughly study this particular concentration, 22 calculations were performed with a variety of supercells $(1 \times 1 \times 4, 2 \times 2 \times 1, 2 \times 1 \times 2, 4 \times 2 \times 1)$. This was done to qualitatively study the Li-Li interactions on the interstitial lattice. Pair interactions were thoroughly studied, a sample of short- to mid-range three site interactions, some close ranged four site, and the possibility of staging into the layers. The results suggest it is unlikely that the large gap with experiment, at this particular $x = 0.0625$ concentration, can be explained by simply not having sampled the right configurations. The special result $V_\sigma(x = 0.25) = 0.53$ V was a configuration of four favorable pairs of Li interstitials identified while studying the $x = 0.0625$ case, dispersed uniformly in a $2 \times 2 \times 1$ supercell. The converged configuration retained the Li pair structure, but the resulting voltage cannot be explained by the Li pair interactions found at $x = 0.0625$. This illustrates the concentration and configuration dependence of the voltage for this system.

In an effort to understand the discrepancy between the calculated voltage and experimental voltage for $Li_{2+x}SnO_3$, crude modeling of defects and their effect on voltage was done. The defects accounted for were antisite defects and stacking faults, both studied in the literature [31,32]. A brief study of the formation energy of Sn/Li antisite defects were calculated for a particular Sn(4e) site, in a $2 \times 1 \times 1$ supercell, swapped with its nearest 8f, 4d, or 4e lithium host lattice sites. Using Eq. (3) the formation energies for the Sn(4e)-Li(8f,4d,4e) antisite defects were calculated to be 2.3, 1.6, and 1.8 eV, respectively. The Sn(4e)/Li(4d) was found to have the lowest formation energy and chosen for the model. This Sn(4e) site was equivalent to the (0.00, 0.749, 0.25) tin site listed in Appendix A. For a stacking fault a $2 \times 1 \times 1$ supercell was used with the uppermost (along the c axis) $[Li_{\frac{1}{3}}Sn_{\frac{2}{3}}O_2]$ plane shifted by the $[\frac{1}{2},\frac{1}{6},0]$ suggested
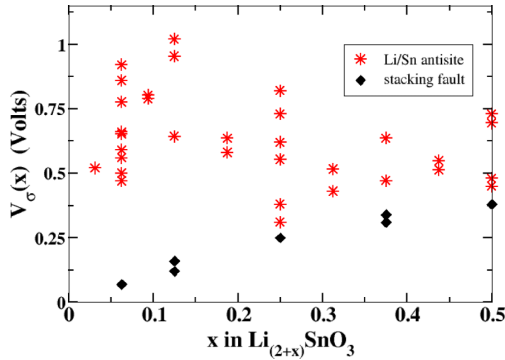
FIG. 12. Sampling of $V_\sigma(x)$ calculated with Eq. (8) for $Li_{2+x}SnO_3$ with antisite and stacking fault defects. Red stars represent results in the presence of Li/Sn antisite defects. Black diamonds represent results in the presence of stacking faults.

by Tarakina *et al.* [31] as the most probable with a 40% likelihood. Our simulation is a coarse approximation with 50% stacking faults imposed on every other [$Li_{\frac{1}{3}}Sn_{\frac{2}{3}}O_2$] plane. Using Eq. (3) the formation energy of this configuration is 0.01 eV. Figure 12 shows a sampling of $V_\sigma(x)$ for both of the defective structures. It is shown in these results that Sn/Li antisite defects can have a large impact on the voltage and greatly improves correspondence with experiment. The stacking fault results show very similar results to the voltage profiles of the simulations without stacking faults shown in Fig. 11.

VI. SURFACES AND INTERFACES WITH LITHIUM

The purpose of studying surfaces and interfaces for Li_2SnO_3 and Li_2SnS_3 is to explore their interaction with lithium at the surface. Transmission electron microscopy images of Li_2SnO_3 reported by Wang *et al.*[10] show nanoflakes with their exposed surface in the *a-b* plane. Motivated by this observation, only surfaces and interfaces in the *a-b* plane were studied.

A. Surface simulations

Surface simulations were performed using the slab geometry shown in Fig. 13. The supercells were simulated using fixed lattice constants based on the 1×1 cell in the *a-b* plane using the optimized a and b lattice constants and a slab thickness determined by $n = 4$ as defined in Fig. 13, corresponding to 20 formula units of $Li_{2+x}Sn(O/S)_3$. The vacuum distance separating the periodic slabs was chosen to be 15 Å for $Li_{2+x}SnO_3$ and 18.7 Å for $Li_{2+x}SnS_3$.

A convenient measure of surface stability is the surface energy which can be defined according to

$$\gamma = \frac{E_{slab} - N E_{bulk} - x E_{Li}}{2\mathcal{A}}. \tag{11}$$

Here E_{slab} and E_{bulk} denote the total electronic energies of the slab and of the bulk $Li_2Sn(O/S)_3$, respectively. N is the number of formula units in the slab and E_{Li} denotes the total
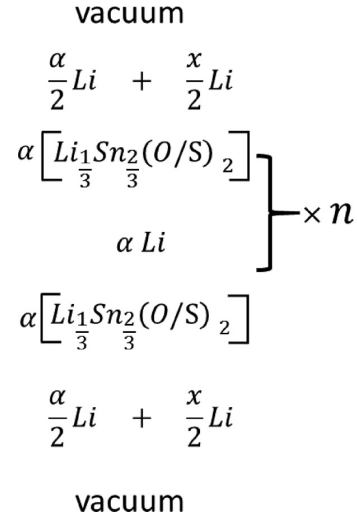

FIG. 13. Schematic diagram of surface geometries for $Li_{2+x}Sn(O/S)_3$ slabs in vacuum. Here x represents the excess lithium per formula unit and is assumed to be distributed equally on the two surfaces. The variable n determines the thickness of the slab. The normalizing factor $\alpha = \frac{3}{2(n+1)}$ is introduced so that the diagram corresponds to one unit of $Li_{2+x}Sn(O/S)_3$.

energy per atom of bcc Li. $\mathcal{A}$ denotes the area of a single surface plane in the simulation cell.

For this surface geometry, the stoichiometric surface ($x = 0$) is missing half of its Li sites. For convenience, the simulations assumed that the missing sites were distributed evenly over the two simulation surfaces. For the chosen supercell, simulations with two, four, and six extra Li atoms correspond to $x = 0.1, 0.2$, and 0.3, respectively. Figure 14 shows the results for the surface energies of Li_2SnS_3 and Li_2SnO_3. This figure shows both materials tend to lower their surface energy when absorbing lithium, which is indicative of a favorable process.
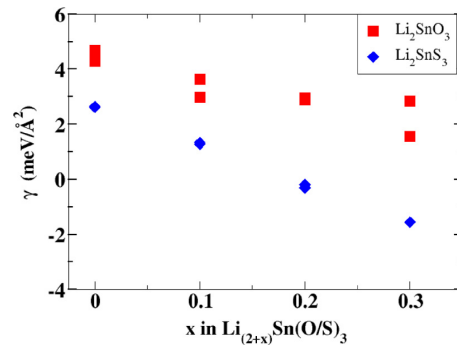

FIG. 14. Surface energies as a function of x as defined in Eq. (11) with $Li_{2+x}SnO_3$ shown as red squares and $Li_{2+x}SnS_3$ with blue diamonds. For all concentrations except $Li_{2.3}SnS_3$, two or more configurations were modeled.
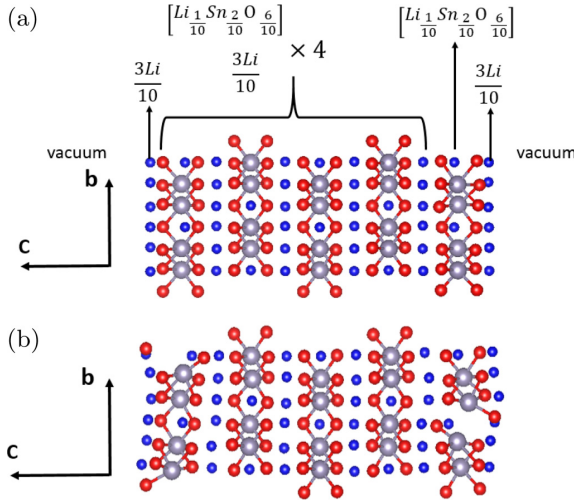
FIG. 15. Optimized surfaces for $Li_{2+0.3}SnO_3$ with different initial positions. In (a), the initial surface Li positions were the ideal bulk lattice sites. In (b), random noise added to the surface lithium sites.

Multiple metastable configurations were found for excess Li concentrations $x > 0$ as indicated in Fig. 14. An interesting example is shown in Fig. 15 which shows two configurations of $Li_{2+0.3}SnO_3$. The configuration shown in Fig. 15(a) was
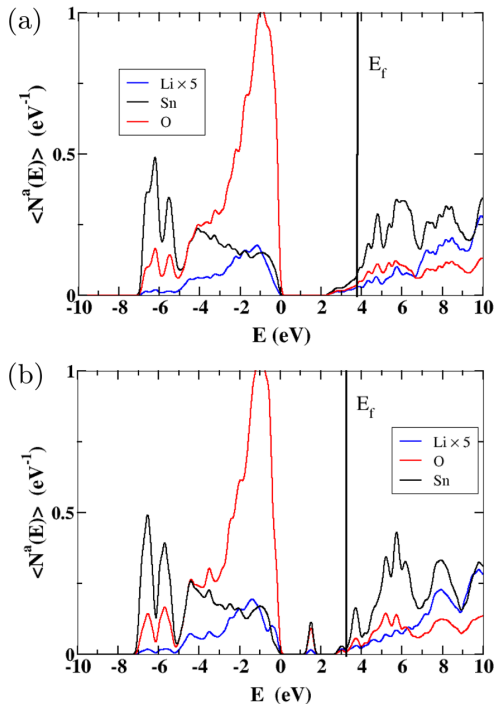

FIG. 16. Partial densities of states for (a) ordered [correspond to Fig. 15(a)] and (b) disordered [corresponding to Fig. 15(b)] $Li_{2+0.3}SnO_3$ surfaces. In each plot, the Li contribution has been scaled by 5.
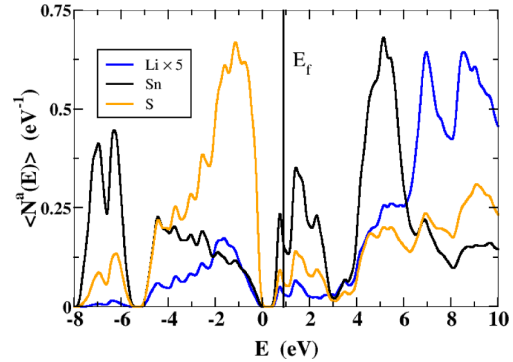

FIG. 17. Partial densities of states for a $Li_{2+0.3}SnS_3$ surface. In this plot, the Li contribution has been scaled by 5.

optimized from the ideal bulk positions of the surface Li sites. The configuration in Fig. 15(b) was optimized from randomized positions of the surface Li sites and has a lower value of γ by 1 meV/$\mathring{A}^2$. The corresponding partial densities of states plots for these two cases are shown in Fig. 16. These results show that the metastable ordered configuration has a partial density of states much like that of the bulk lattice with the Fermi level raised to within the conduction band due to the excess Li atoms at the surface. The relaxed configuration shows new states within the bulk band gap which are due to broken Sn-O bonds.

Less variation in the surface geometries and energies were found for the $Li_{2+x}SnS_3$ simulations. The partial density of states are shown in Fig. 17. In this case, the density of states is similar to that of the bulk with the Fermi level located within the Sn-S conduction band due to the excess surface Li atoms. The shift in the energies of the conduction band states is localized to the surface layer Sn $5s$ states.

B. Interface simulations

To further explore the interaction of these materials with lithium interface calculations were done with bulk lithium using slab geometry. The converged results from the $x = 0.3$ surface calculations, with lithium left in their native positions from the layers, were used as the starting point for these simulations. The vacuum of these relaxed surface calculations were filled with 30 Li atoms distributed uniformly and at a density that is approximately that of bulk lithium. These structures were optimized with fixed lattice parameters in the layer planes while the supercell dimension perpendicular to the layers was allowed to vary.
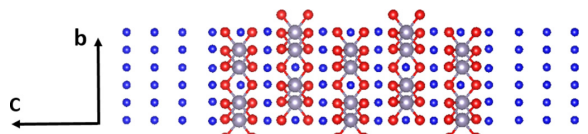

FIG. 18. Ball and stick model of the optimized ideal interface of Li_2SnO_3/Li. Li, Sn, and O are indicated with blue, gray, and red balls, respectively.

54
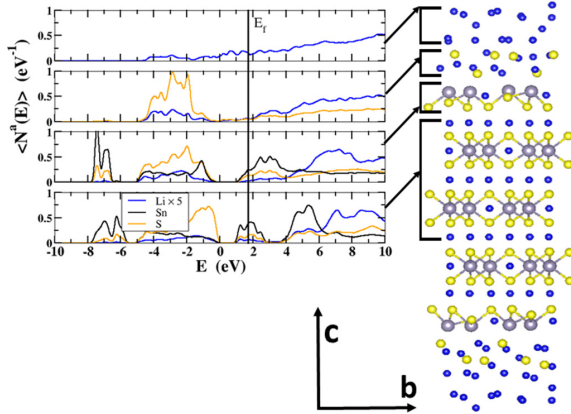
FIG. 19. Partial densities of states of regions of the optimized interface of Li_2SnS_3/Li (with Li contributions scaled by a factor of 5). The corresponding ball and stick model of the optimized geometry is shown on the right of the diagram with Li, Sn, and S indicated with blue, gray, and yellow balls.

Figure 18 shows the optimized geometry for the ideal Li_2SnO_3/Li interface. In this case, the converged geometry of the lithium slab resembles that of bcc lithium, skewed by the interface boundary. While this ideal interface has been found, it is metastable relative to the formation of Li_2O. For example, displacing one of the surface O sites into the lithium slab generally results in a lower energy structure (by 1.5 eV in one example) with broken Sn-O bonds.

Figure 19 shows the optimized geometry for the Li_2SnS_3/Li interface, showing that Li_2SnS_3 undergoes a decomposition at the surface. In order to examine the Li_2SnS_3/Li in greater detail, partial densities of states from four different sections of the calculation slab were analyzed as shown in Fig. 19. The top section represents pure metallic Li. The second section resembles Li_2S, while the third section shows nonstoichiometric Li_xSnS_y. The central layer of the slab represents bulk Li_2SnS_3.

VII. DISCUSSION AND CONCLUSIONS

The results of these simulations show that, despite the fact that the porous layered calcogenide materials Li_2SnO_3 and Li_2SnS_3 both have the same crystal structure based on the space group C2/c, they have very different responses to excess Li. An important component of the explanation is the qualitative differences in the band structures of the two materials. Li_2SnS_3 has an unoccupied conduction band formed from Sn $5s$ and S $3p$ states [4] located 1 eV above the valence band. The simulations for $Li_{2+x}SnS_3$ show that these bands readily accommodate the excess electrons from lithiation. Figure 9 shows isosurface plots for electrons within this band for particular configurations of the lithiated material for $x = 0.5$ and $x = 1$, illustrating the antibonding Sn $5s$ and S $3p$ states. A consequence of this lithiation mechanism is the predicted constant voltage versus Li concentration x as shown in Fig. 10. By contrast, in Li_2SnO_3 the corresponding bands for Sn $5s$ and O $2p$ states lie much higher in energy. The

TABLE IV. Fractional coordinates (x, y, z) of unique atoms in the conventional unit cells of Li_2SnO_3 and Li_2SnS_3 compared with experimental measurements reported by Refs. [2] and [4], respectively. The "site" column lists the site multiplicity and Wyckoff label. In order to more easily compare the two structures, the crystal origin chosen by Ref. [4] for Li_2SnS_3 was shifted by $(0, \frac{1}{2}, \frac{1}{2})$.

	Atom	Site	Comp.	Expt.
Li_2SnO_3	Li	8f	(0.232, 0.077, −0.001)	(0.239, 0.078, −0.001)
	Li	4e	(0.000, 0.085, 0.250)	(0.000, 0.083, 0.250)
	Li	4d	(0.250, 0.250, 0.500)	(0.250, 0.250, 0.500)
	Sn	4e	(0.000, 0.417, 0.250)	(0.000, 0.417, 0.250)
	Sn	4e	(0.000, 0.749, 0.250)	(0.000, 0.751, 0.250)
	O	8f	(0.134, 0.258, 0.131)	(0.134, 0.260, 0.133)
	O	8f	(0.114, 0.583, 0.131)	(0.110, 0.584, 0.134)
	O	8f	(0.133, 0.909, 0.129)	(0.135, 0.909, 0.133)
Li_2SnS_3	Li	8f	(0.256, 0.085, 0.000)	(0.253, 0.084, 0.000)
	Li	4e	(0.000, 0.083, 0.250)	(0.000, 0.083, 0.250)
	Li	4d	(0.250, 0.250, 0.500)	(0.250, 0.250, 0.500)
	Sn	4e	(0.000, 0.417, 0.250)	(0.000, 0.417, 0.250)
	Sn	4e	(0.000, 0.750, 0.250)	(0.000, 0.750, 0.250)
	S	8f	(0.132, 0.255, 0.128)	(0.136, 0.258, 0.131)
	S	8f	(0.115, 0.583, 0.127)	(0.112, 0.583, 0.131)
	S	8f	(0.132, 0.911, 0.126)	(0.135, 0.908, 0.127)

simulation shows that the lithiation process is still energetically favorable, but in order to accommodate the excess electrons, new localized states are formed within the band gap of the material. The simulations show that these states are typically associated with broken Sn-O bonds such as shown in Fig. 7.

Calculations of the voltage versus lithium concentration for $Li_{2+x}SnO_3$ shown in Figs. 11 and 12 demonstrate that Li/Sn antisite defects can have a significant impact on the voltage profiles. The results suggest that Li/Sn antisite defects are present in the experimental samples presented in the literature [8–10]. Preliminary computational results for Li/Sn antisite defects in $Li_{2+x}SnS_3$ suggest their effects on the voltage profiles are small. Our calculations for defect free $Li_{2+x}SnS_3$ predict a constant voltage versus lithium concentration, which has not yet been confirmed experimentally. Assuming that the lithiation proceeds to the concentration of $x = 1$ without interference from possible competing reactions, the theoretical capacity is estimated to be 117 mAh/g.

For both materials, the most efficient ion migration processes were shown to involve the interstitial sites in interstitiacy mechanisms with net migration perpendicular to the porous layers as shown in Fig. 4, finding $E_m = 0.14$ eV and $E_m = 0.22$ eV for pristine Li_2SnO_3 and Li_2SnS_3, respectively. Recently, nuclear magnetic resonance experiments on Li_2SnO_3 have detected signals corresponding to the three unique Li sites, finding evidence for the predominant diffusion pathway to occur perpendicular to the a-b layer planes [37]. This is in qualitative agreement with the calculations, although the analysis of the experiments did not involve consideration of interstitial sites. Comparing the calculated results for E_m with activation energies E_a extracted from impedance measurements, suggests that the bottleneck for ion migration in the pristine materials is the formation of vacancy-interstitial pairs. For lithiated $Li_{2+x}SnS_3$, we expect there to be a sizable
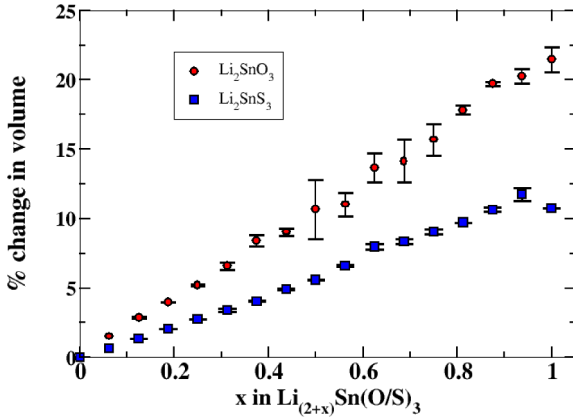
FIG. 20. Percent change in volume for $Li_{2+x}SnO_3$ (red circles) and $Li_{2+x}SnS_3$ (blue squares). Error bars are the standard deviation of the mean.

population of interstitial Li ions so that their migration should be dominated by E_m. Further computational and experimental investigations are needed to verify whether or not the activation energy of lithiated $Li_{2+x}SnS_3$ has the expected small value of $E_a \approx E_m = 0.2$ eV.
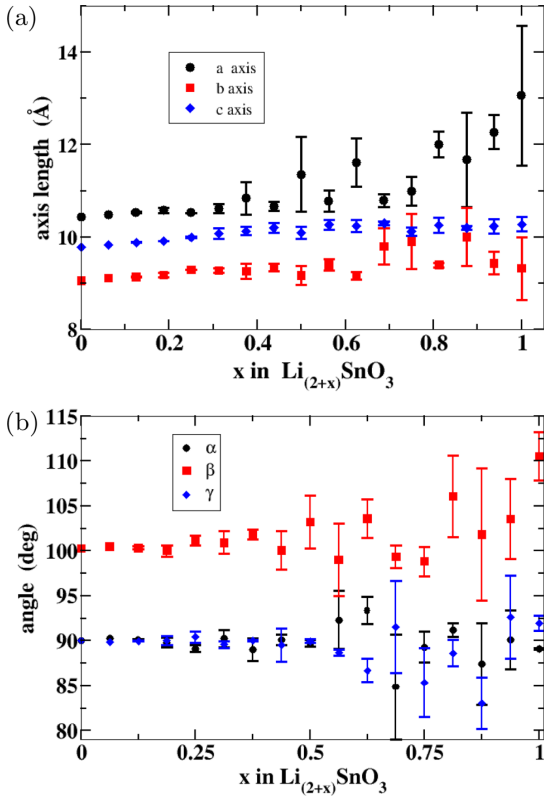
FIG. 21. Average cell dimensions (a) and angles (b) for $Li_{2+x}SnO_3$. Error bars are the standard deviation of the mean.
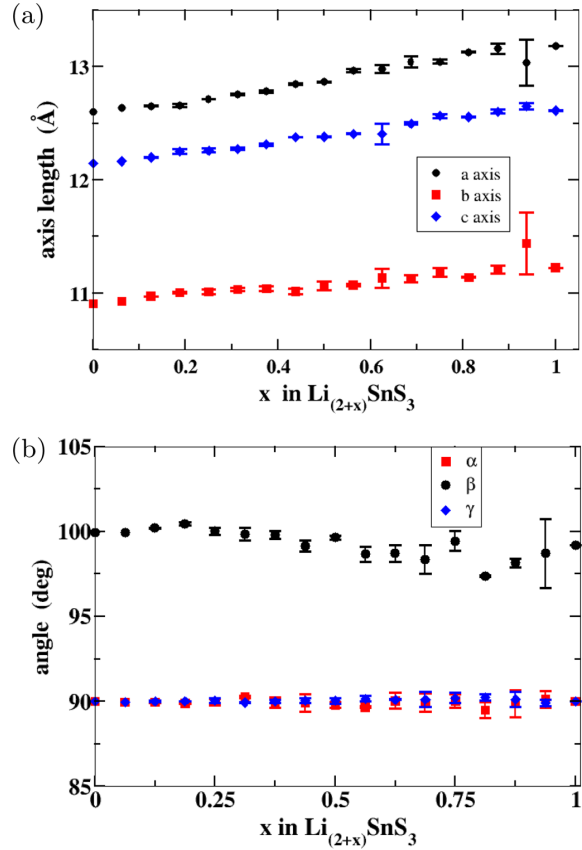
FIG. 22. Average cell dimensions (a) and angles (b) for $Li_{2+x}SnS_3$. Error bars are the standard deviation of the mean.

Simulations of surfaces and interfaces of these materials suggest that it is energetically favorable to add a small amount of excess Li at the surface, but the surfaces seem to be reactive when interfaced with Li metal. While a metastable interface of Li_2SnO_3/Li was found, displacing surface O atoms was found to lower the energy of the model interface. The modeled interface of Li_2SnS_3/Li found the likely formation of Li_2S and the breaking of Sn-S bonds. These simulations are very sensitive to the initial model geometries. Additional simulations would be needed to go beyond the qualitative observation that the interfaces are reactive with respect to Li metal.

ACKNOWLEDGMENTS

APPENDIX A: STRUCTURAL DETAILS

For completeness, the unique positions of the atoms within the conventional cells of Li_2SnO_3 and Li_2SnS_3 are listed in Table IV. The calculated fractional coordinates agree well with the experimental results. Additionally, after shifting the origin of the coordinate systems, the two materials are shown to have very similar fractional coordinates.

APPENDIX B: LITHIATION EFFECTS
ON CELL DIMENSION

The results presented here detail the lithiation studies discussed in Sec. V A. Figures 20, 21, and 22 show changes in volume and lattice parameters calculated from a random sampling of configurations in $2 \times 1 \times 1$ supercells. For $Li_{2+x}SnO_3$, two or more configurations were sampled for $x > 0.0625$. For $x = 1$, although there is only one ideal configuration for the interstitial lattice, the system is highly metastable such that a small displacement in the initial ideal configuration results in significantly different optimized lattice parameters. For $Li_{2+x}SnS_3$, two configurations were sampled for $0.0625 < x < 1$. For this system, the results for each concentration are relatively insensitive to the initial configurations of interstitial placements. The points on the graphs represent simple averages and the error bars represent the standard deviations of the mean from the those averages.

[1] R. M. Hazen and L. W. Finger, Am. Mineral. **63**, 289 (1978).

[2] G. Kreuzburg, F. Stewner, and R. Hoppe, Z. Anorg. Allg. Chem. **379**, 242 (1971).

[3] A. Kuhn, T. Holzmann, J. Nuss, and B. V. Lotsch, J. Mater. Chem. A **2**, 6100 (2014).

[4] J. A. Brant, D. M. Massi, N. A. W. Holzwarth, J. H. MacNeil, A. P. Douvalis, T. Bakas, S. W. Martin, M. D. Gross, and J. A. Aitken, Chem. Mater. **27**, 189 (2015).

[5] Y.-C. Chen, M. Huo, Y. Liu, T. Chen, C.-C. Leng, Q. Li, Z.-L. Sun, and L.-J. Song, Chin. Phys. Lett. **32**, 017102 (2015).

[6] G. Vitins, G. Kizane, A. Lusis, and J. Tiliks, J. Solid State Electrochem. **6**, 311 (2002).

[7] L. Teo, M. Buraidah, A. Nor, and S. Majid, Ionics **18**, 655 (2012).

[8] I. A. Courtney and J. R. Dahn, J. Electrochem. Soc. **144**, 2045 (1997).

[9] D. Zhang, S. Zhang, Y. Jin, T. Yi, S. Xie, and C. Chen, J. Alloys Compd. **415**, 229 (2006).

[10] Q. Wang, Y. Huang, Y. Zhao, W. Zhang, and Y. Wang, Surf. Interface Anal. **45**, 1297 (2013).

[11] T.-J. Kim, C. Kim, D. Son, M. Choi, and B. Park, J. Power Sources **167**, 529 (2007).

[12] A. Pedersen and M. Luisier, ACS Appl. Mater. Interfaces **6**, 22257 (2014).

[13] P. Hohenberg and W. Kohn, Phys. Rev. **136**, B864 (1964).

[14] W. Kohn and L. J. Sham, Phys. Rev. **140**, A1133 (1965).

[15] P. E. Blöchl, Phys. Rev. B **50**, 17953 (1994).

[16] N. A. W. Holzwarth, A. R. Tackett, and G. E. Matthews, Comput. Phys. Commun. **135**, 329 (2001).

[17] P. Giannozzi, S. Baroni, N. Bonini, M. Calandra, R. Car, C. Cavazzoni, D. Ceresoli, G. L. Chiarotti, M. Cococcioni, I. Dabo, A. D. Corso, S. de Gironcoli, S. Fabris, G. Fratesi, R. Gebauer, U. Gerstmann, C. Gougoussis, A. Kokalj, M. Lazzeri, L. Martin-Samos, N. Marzari, F. Mauri, R. Mazzarello, S. Paolini, A. Pasquarello, L. Paulatto, C. Sbraccia, S. Scandolo, G. Sclauzero, A. P. Seitsonen, A. Smogunov, P. Umari, and R. M. Wentzcovitch, J. Phys.: Condens. Matter **21**, 395502 (2009).

[18] J. P. Perdew and Y. Wang, Phys. Rev. B **45**, 13244 (1992).

[19] The choice of LDA functional was made based on previous investigations [23,24,38–41] of similar materials which showed that provided that the lattice constants are scaled by a correction factor of 1.02, the simulations are in good agreement with experiment, especially lattice vibrational frequencies and heats of formation.

[20] H. Jónsson, G. Mills, and K. W. Jacobsen, in *Classical and Quantum Dynamics in Condensed Phase Simulations*, edited by B. J. Berne, G. Ciccotti, and D. F. Coker (World Scientific, Singapore, 1998), pp. 385–404.

[21] G. Henkelman, B. P. Uberuaga, and H. Jónsson, J. Comput. Phys. **113**, 9901 (2000).

[22] G. Henkelman and H. Jónsson, J. Comput. Phys. **113**, 9978 (2000).

[23] N. D. Lepley, N. A. W. Holzwarth, and Y. A. Du, Phys. Rev. B **88**, 104103 (2013).

[24] Z. D. Hood, C. Kates, M. Kirkham, S. Adhikari, C. Liang, and N. A. W. Holzwarth, Solid State Ionics **284**, 61 (2015).

[25] A. R. Tackett, N. A. W. Holzwarth, and G. E. Matthews, Comput. Phys. Commun. **135**, 348 (2001).

[26] OpenDX – The Open Source Software Project Based on IBM's Visualization Data Explorer; http://www.opendx.org.

[27] A. Kokalj, J. Mol. Graphics Modell. **17**, 176 (1999); computer code available at http://www.xcrysden.org.

[28] A. Kokalj, Comput. Mater. Sci. **28**, 155 (2003).

[29] K. Momma and F. Izumi, J. Appl. Cryst. **44**, 1272 (2011); computer code available at http://jp-minerals.org/vesta/en/.

[30] T. Hahn (ed.), *International Tables for Crystallography, Volume A: Space-group Symmetry*, 5th rev. ed. (Kluwer, Berlin, 2002).

[31] N. V. Tarakina, T. A. Denisova, L. G. Maksimova, Y. V. Baklanova, A. P. Tyutyunnik, I. F. Berger, V. G. Zubkov, and G. Van Tendeloo, Z. Kristallogr. Suppl. **30**, 375 (2009).

[32] Z. Wang, Y. Ren, T. Ma, W. Zhuang, S. Lu, G. Xu, A. Abouimrane, K. Amine, and Z. Chen, RSC Adv. **6**, 31559 (2016).

[33] A. R. West, *Basic Solid State Chemistry*, 2nd ed. (John Wiley & Sons, New York, 1999).

[34] W. Hayes and A. M. Stoneham, *Defects and Defect Processes in Nonmetallic Solids* (John Wiley and Sons, New York, 1985).

[35] M. K. Aydinol, A. F. Kohan, G. Ceder, K. Cho, and J. Joannopoulos, Phys. Rev. B **56**, 1354 (1997).

[36] D. de Fontaine, in *Solid State Physics*, Vol. 47 (Academic Press, Cambridge, 1994), pp. 33–176.

[37] J. Langer, D. L. Smiley, A. D. Bain, G. R. Goward, and M. Wilkening, J. Phys. Chem. C **120**, 3130 (2016).

[38] Y. A. Du and N. A. W. Holzwarth, Phys. Rev. B **76**, 174302 (2007).

[39] N. A. W. Holzwarth, N. D. Lepley, and Y. A. Du, J. Power Sources **196**, 6870 (2011).

[40] Y. A. Du and N. A. W. Holzwarth, Phys. Rev. B **81**, 184106 (2010).

[41] K. Senevirathne, C. S. Day, M. D. Gross, A. Lachgar, and N. A. W. Holzwarth, Solid State Ionics **233**, 95 (2013).

58

Appendix B

First principles molecular dynamics of Li$_4$SnS$_4$

Li$_4$SnS$_4$ and Li$_4$SnSe$_4$: Simulations of Their Structure and Electrolyte Properties

Ahmad Al-Qawasmeh, Jason Howard,* and N. A. W. Holzwarth**,z

Department of Physics, Wake Forest University, Winston-Salem, North Carolina 27109-7507, USA

Recent experimental literature reports the solid state electrolyte properties of Li$_4$SnS$_4$ and Li$_4$SnSe$_4$, identifying interesting questions regarding their structural details and motivating our first principles simulations. Together with Li$_4$GeS$_4$, these materials are all characterized by the orthorhombic space group *Pnma* and are found to be isostructural. They have a ground state crystal structure (denoted Li$_4$SnS$_4^0$) having interstitial sites in void channels along the *c*-axis. They also have a meta-stable structure (denoted Li$_4$SnS$_4^*$) which is formed by moving one fourth of the Li ions from their central sites to the interstitial positions, resulting in a 0.5 Å contraction of the *a* lattice parameter. Relative to their ground states, the meta-stable structures are found to have energies 0.25 eV, 0.02 eV, and 0.07 eV for Li$_4$GeS$_4^*$, Li$_4$SnS$_4^*$, and Li$_4$SnSe$_4^*$, respectively. Consistent with these simulation results, the ground state forms for Li$_4$GeS$_4^0$, Li$_4$SnS$_4^0$ and Li$_4$SnSe$_4^0$ and the meta-stable form for Li$_4$SnS$_4^*$ have been reported in the experimental literature. In addition, simulations of Li ion migration in these materials are also investigated.

Recently, there has been significant progress in developing stable solid electrolytes with high ionic conductivity,[1] which has been identified as a key to improving battery technologies.[2] Recent literature[3–7] reports the use of Li$_4$SnS$_4$ and related materials as relatively stable solid electrolytes for use in all-solid-state Li batteries. Kaib, Haddadpour, et al.[3] and Kaib, Bron, et al.[5] synthesized Li$_4$SnS$_4$ and Li$_4$SnSe$_4$, showing that pure materials could be obtained by removing water or methanol from solution based preparations, and comparing their structures and ionic conductivities. MacNeil et al.[4] used high temperature solid state techniques to synthesize Li$_4$SnS$_4$ and made a detailed structural analysis to show it to be isostructural with Li$_4$GeS$_4$. Sahu et al.[6] showed that Li$_4$SnS$_4$ and its alloys with Li$_3$AsS$_4$ have reasonable ionic conductivity (10^{-5}–10^{-4} S/cm at room temperature) with comparatively more air-stability than other sulfide electrolytes. Park et al.[7] demonstrated favorable conductivity and stability properties of Li$_4$SnS$_4$ and its alloys with LiI.

From this literature, some interesting questions arise regarding crystal structures and mechanisms for ion mobility. In order to address these questions, we use first principles methods to examine the ideal crystal forms and defect structures of Li$_4$SnS$_4$ and the structurally and chemically related materials Li$_4$GeS$_4$ and Li$_4$SnSe$_4$. For each of these materials, we identify two closely related structures – an ideal ground state structure and an ideal meta-stable structure. The simulations show that the meta-stable structural form is most accessible to Li$_4$SnS$_4$ of the three materials studied. The simulations are extended to study mechanisms of Li ion migration in both Li$_4$SnS$_4$ and Li$_4$SnSe$_4$ and are related to the experimental results reported in the literature.

Computational Methods

The computational methods used in this work are based on density functional theory (DFT),[8,9] using the projected augmented wave (PAW)[10] formalism. The PAW basis and projector functions were generated by the ATOMPAW[11] code and the crystalline materials were modeled using the QUANTUM ESPRESSO[12] and ABINIT[13] packages. Visualizations were constructed using the *XCrySDEN*,[14,15] and *VESTA*[16] software packages.

*Electrochemical Society Student Member.
**Electrochemical Society Member.
zE-mail: natalie@wfu.edu

The exchange correlation function is approximated using the local-density approximation (LDA).[17] The choice of LDA functional was made based on previous investigations[18–20] of similar materials which showed that, provided that the lattice constants are scaled by a correction factor of 1.02, the simulations are in good agreement with experiment, especially lattice vibrational frequencies and heats of formation. The partial densities of states were calculated as described in previous work,[20,21] using weighting factors based on the charge within the augmentation spheres of each atom with radii $r_c^{Li} = 1.6$, $r_c^{Sn} = 2.3$, $r_c^{S} = 1.7$, and $r_c^{Se} = 2.3$ in bohr units. The reported partial densities of states curves $< N^a(E) >$ were averaged over the atomic sites of each type *a*.

The calculations were well converged with plane wave expansions of the wave function including $|\mathbf{k} + \mathbf{G}|^2 \leq 64$ bohr^{-2}. Calculations for the conventional unit cells were performed using a Brillouin-zone sampling grid of $4 \times 8 \times 8$. Simulations of Li ion migration were performed at constant volume in supercells constructed from the optimized conventional cells extended by $1 \times 2 \times 2$ and a Brillouin-zone sampling grid of $2 \times 2 \times 2$. In modeling charged defects (Li ion vacancies or interstitials), the system was assumed to remain electrically insulating and a uniform background charge was added in order to evaluate the electrostatic interactions. The minimum energy path for Li ion migration was estimated using the "nudged elastic band" (NEB) method[22–24] as programmed in the QUANTUM ESPRESSO package, using 5 images between each metastable configuration. For each minimum energy path, the migration energy, E_m was determined as the energy difference between the lowest and highest energy of the path. The "formation energies" E$_f$ for producing neutral defects in the form of vacancy-interstitial pairs were calculated for the same supercells. The molecular dynamics simulations were performed at constant volume in neutral $1 \times 2 \times 2$ supercells using further reduced convergence parameters, including a reduced plane wave expansion cutoff of $|\mathbf{k} + \mathbf{G}|^2 \leq 49$ bohr^{-2} and a Brillouin-zone sampling grid of $1 \times 1 \times 1$. The simulations were performed for a microcanonical ensemble with a time integration step of $\Delta t = 3.6 \times 10^{-15}$ s for simulation temperatures less than 900 K. For simulation temperatures greater than 900 K, the time integration step was reduced to $\Delta t = 2.4 \times 10^{-15}$ s. This resulted in total energy conservation within 0.1 eV throughout the simulation. The simulations were carried out for durations between 3-8 pico seconds. After an equilibration delay of approximately 0.1 ps, the temperature of the simulation was determined from the averaged kinetic energy of the ions. The
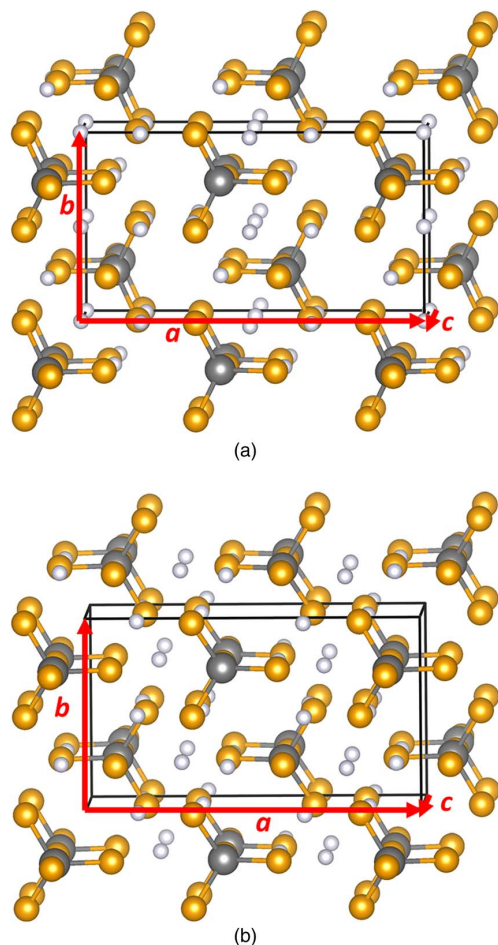
Figure 1. Ball and stick models of (a) $Li_4SnS_4^0$ and (b) $Li_4SnS_4^*$. Li, Sn, and S are represented by light gray, dark gray, and orange balls respectively. The red arrows indicate the *a*, *b*, and *c* lattice vectors.

simulated temperatures ranged between 550 K and 1000 K, well below the melting temperature of 1231 K reported by MacNeil et al.[4]

Simulated Crystal Structures

There are two reported analyses of the crystal structure of Li_4SnS_4.[3,4] The two analyses agree that the structure is characterized by the space group *Pnma* (No. 62 in the International Table of Crystallography[25]), but differ slightly in the reported lattice constants and the fractional coordinates of one of the Li sites.[4] The structural analysis of MacNeil et al.[4] was measured at room temperature and is perfectly ordered. However, the structural analysis of Kaib, Haddadpour, et al.,[3] was measured at the temperatures in the range 100–193 K, and instead of the Li sites found by MacNeil et al. at the Wyckoff labeled 4*a* positions, fractionally occupied 8*d* Li sites are found.

We computationally investigated both structures, finding that the ordered structure analyzed by MacNeil et al.[4] to be the ground state structure which we denote as "$Li_4SnS_4^0$". Simulations of ordered approximations to the disordered structure of Kaib, Haddadpour, et al.[3] find a meta-stable structure which we denote as "$Li_4SnS_4^*$" having an energy 0.02 eV/formula unit higher in energy than the ground state structure. Ball and stick drawings of the two structures are shown in Fig. 1. The corresponding calculated and measured lattice constants are listed in Table I and the calculated and measured fractional coor-

Table I. Comparison of lattice parameters for Li_4SnS_4 and related compounds in their ground state and meta-stable structures. Calculated parameters are scaled by factor of 1.02 to correct for systematic LDA error. Measured parameters are listed in parentheses. The relative energies *E* for the ground state and meta-stable structures are also listed in units of eV per formula unit.

	$Li_4GeS_4^0$	$Li_4GeS_4^*$
a (Å)	14.01 (14.06)[a]	13.49
b (Å)	7.74 (7.75)[a]	7.79
c (Å)	6.12 (6.15)[a]	6.30
E (eV/FU)	0.00	0.25
	$Li_4SnS_4^0$	$Li_4SnS_4^*$
a (Å)	14.25 (14.31)[a]	13.81 (13.81)[b]
b (Å)	7.86 (7.90)[a]	7.93 (7.96)[b]
c (Å)	6.31 (6.33)[a]	6.41 (6.37)[b]
E (eV/FU)	0.00	0.02
	$Li_4SnSe_4^0$	$Li_4SnSe_4^*$
a (Å)	14.98 (14.93)[c]	14.48
b (Å)	8.26 (8.22)[c]	8.38
c (Å)	6.62 (6.60)[c]	6.86
E (eV/FU)	0.00	0.07

[a]Ref. 4.
[b]Ref. 3.
[c]Ref. 5.

dinates are listed in Table II. In addition to results for Li_4SnS_4, results for Li_4GeS_4 and Li_4SnSe_4 are also listed in these tables.

Interestingly, the main difference between the simulated structures of $Li_4SnS_4^0$ and $Li_4SnS_4^*$ is that four Li's per unit cell occupy different void regions between the SnS_4 tetrahedra. In the $Li_4SnS_4^0$ structure, the special Li ions occupy sites at the center and boundaries of the unit cell having multiplicity and Wyckoff label 4*a*. In the $Li_4SnS_4^*$ structure, the special Li ions instead occupy sites interior to the unit cell having multiplicity and Wyckoff label 4*c*. In order to avoid confusion of this site with the other fully occupied 4*c* Li site of these structures, we use the symbol *c′* to refer to this site. While the simulated fractional coordinates of the special Li ions for this 4*c′* site do not agree with the two 8*d* fractionally occupied coordinates found by Kaib, Haddadpour, et al.,[3] the optimized lattice constants are in excellent agreement, as shown in Table I. It is interesting to note that the lattice constants for these ideal structures are characterized by a contraction of the *a* lattice parameter by approximately 0.5 Å for the meta-stable structure relative to the ground state structure, while the changes to the other lattice parameters are in the neighborhood of 0.1 Å. This lattice contraction is energetically significant; the energy difference between $Li_4SnS_4^*$ calculated with the lattice constants of $Li_4SnS_4^0$ relative to Li_4SnS_4 calculated with its optimized lattice constants is 0.03 eV/formula unit. We should also point out that the original X-ray analysis of Kaib, Haddadpour, et al.,[3] for the $Li_4SnS_4^*$ structure was performed at low temperatures (100–193 K) while the X-ray analysis of MacNeil et al.[4] was performed at room temperature. It is our experience that lattice constants typically change with temperature by less than 0.1 Å, so that the lattice constant differences between the $Li_4SnS_4^0$ and $Li_4SnS_4^*$ structures should not be attributed to temperature alone. In addition, Sahu et al.[6] report room temperature X-ray analysis for $Li_4SnS_4^*$ consistent with an expansion of the lattice by approximately 0.02 Å.

Because of its low atomic number, the X-ray signal for Li positions is notoriously small so that it is reasonable to ask whether the simulated $Li_4SnS_4^*$ structure might be compatible with the structural data reported by Kaib, Haddadpour, et al.,[3] even if the site analysis differs. Using the Mercury software package,[26] with the structural data from experiment and simulations we compare the computed X-ray patterns for the structures of $Li_4SnS_4^0$ and $Li_4SnS_4^*$ in Fig. 2. We see that the patterns for $Li_4SnS_4^0$ and $Li_4SnS_4^*$ are distinguishable and that there

Table II. Comparison of fractional coordinates of unique atomic positions for Li_4SnS_4 and related compounds in their ground state and meta-stable structures, using orientation and origin choice given in Ref. 4. The second column lists the site multiplicity and Wyckoff label. We use the notation c' to denote the special Li site which characterizes the meta-stable structures. Measured parameters are listed in square brackets when available.

Atom	Site	$Li_4GeS_4^0$ (x, y, z)	$Li_4GeS_4^*$ (x, y, z)
Li	$4a$	(0.000, 0.000, 0.000) [(0.000, 0.000, 0.000)][a]	–
Li	$4c'$	–	(0.260, 0.250,-0.001)
Li	$4c$	(0.412, 0.250, 0.127) [(0.412, 0.250, 0.129)][a]	(0.429, 0.250, 0.216)
Li	$8d$	(0.177, 0.000, 0.186) [(0.178, 0.000, 0.192)][a]	(0.147,-0.023, 0.139)
Ge	$4c$	(0.089, 0.250, 0.645) [(0.089, 0.250, 0.649)][a]	(0.097, 0.250, 0.620)
S	$4c$	(0.084, 0.250, 0.277) [(0.086, 0.250, 0.291)][a]	(0.105, 0.250, 0.261)
S	$8d$	(0.158, 0.010, 0.780) [(0.157, 0.015, 0.779)][a]	(0.177, 0.019, 0.761)
S	$4c$	(0.437, 0.250, 0.728) [(0.439, 0.250, 0.731)][a]	(0.434, 0.250, 0.810)

Atom	Site	$Li_4SnS_4^0$ (x, y, z)	$Li_4SnS_4^*$ (x, y, z)
Li	$4a$	(0.000, 0.000, 0.000) [(0.000, 0.000, 0.000)][a]	–
Li	$4c'$	–	(0.287, 0.250, 0.003) [-][b]
Li	$4c$	(0.410, 0.250, 0.124) [(0.409, 0.250, 0.126)][a]	(0.429, 0.250, 0.359) [(0.430, 250, 0.338)][b]
Li	$8d$	(0.176, 0.003, 0.178) [(0.178, 0.004, 0.179)][a]	(0.158,-0.004, 0.149)[(0.160, 0.005, 0.154)][b]
Sn	$4c$	(0.093, 0.250, 0.640) [(0.092, 0.250, 0.642)][a]	(0.090, 0.250, 0.633) [(0.087, 0.250, 0.635)][b]
S	$4c$	(0.080, 0.250, 0.255) [(0.083, 0.250, 0.267)][a]	(0.092, 0.250, 0.256) [(0.091, 0.250, 0.263)][b]
S	$8d$	(0.152,-0.005, 0.787) [(0.161, 0.001, 0.784)][a]	(0.158,-0.004, 0.149) [(0.167, 0.007, 0.767)][b]
S	$4c$	(0.430, 0.250, 0.732) [(0.432, 0.250, 0.766)][a]	(0.423, 0.250, 0.748) [(0.424, 0.250, 0.736)][b]

Atom	Site	$Li_4SnSe_4^0$ (x, y, z)	$Li_4SnSe_4^*$ (x, y, z)
Li	$4a$	(0.000, 0.000, 0.000) [(0.000, 0.000, 0.000)][c]	–
Li	$4c'$	–	(0.282, 0.250, 0.002)
Li	$4c$	(0.413, 0.250, 0.118) [(0.412, 0.250, 0.106)][c]	(0.428, 0.250, 0.358)
Li	$8d$	(0.175, 0.003, 0.178) [(0.178, 0.005, 0.180)][c]	(0.157, -0.006, 0.147)
Sn	$4c$	(0.094, 0.250, 0.639) [(0.092, 0.250, 0.643)][c]	(0.090, 0.250, 0.630)
Se	$4c$	(0.080, 0.250, 0.252) [(0.082, 0.250, 0.264)][c]	(0.093, 0.250, 0.250)
Se	$8d$	(0.162,-0.008, 0.785) [(0.161,-0.002, 0.784)][c]	(0.177, 0.005, 0.770)
Se	$4c$	(0.430, 0.250, 0.725) [(0.432, 0.250, 0.728)][c]	(0.422, 0.250, 0.750)

[a]Ref. 4.
[b]Ref. 3, omitting fractionally occupied Li position.
[c]Ref. 5.

seems to be good agreement between our simulated structures and the corresponding X-ray results. While it would be better to compare the simulated diffraction patterns directly with the experimental data, the good agreement between the simulations and the fitted results from experiment shown in Fig. 2 is encouraging. It is interesting to note that two other groups[6,7] have recently reported preparations of Li_4SnS_4 using relatively low temperature processing similar to that of Kaib, Haddadpour, et al.[3] Both of these studies report X-ray diffrac-
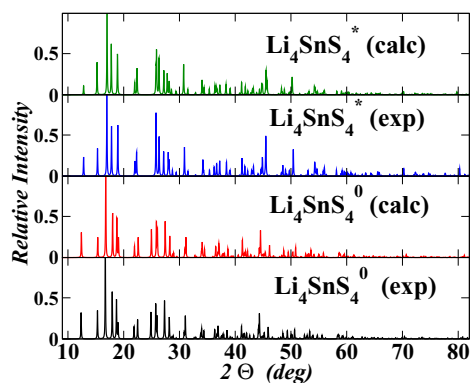

Figure 2. X-ray diffraction patterns generated by the Mercury software package[26] assuming an X-ray wavelength of $\lambda = 1.54056$ Å, comparing simulation (calc) and experimental (exp) results for the $Li_4SnS_4^0$ and $Li_4SnS_4^*$ structures. The structural parameters from experiment were taken from Ref. 4 for $Li_4SnS_4^0$ and from Ref. 3 for $Li_4SnS_4^*$.

tion patterns, presumably measured at room temperature, which show strong similarity to the patterns for $Li_4SnS_4^*$ shown in Fig. 2. Presumably, the ground state $Li_4SnS_4^0$ structure is accessible using the higher temperature processes described by MacNeil et al.[4]

It is interesting to ask the question whether the structurally and chemically similar material Li_4GeS_4 behaves in a similar way. The simulation results for the the $Li_4GeS_4^0$ and $Li_4GeS_4^*$ structures are listed in Table I and in Table II together with available experimental values. The fractional coordinates are very similar to those of Li_4SnS_4. However, in this case, we would predict that the meta-stable $Li_4GeS_4^*$ structure is less likely to form since its energy is predicted to be 0.25 eV/formula unit higher in energy than the ground state energy. The investigation was also extended to Li_4SnSe_4 which was recently synthesized by Kaib, Bron, et al.[5] using relatively high temperature techniques. These authors find Li_4SnSe_4 to take the "ground state" $Li_4SnSe_4^0$ structure. Our simulations find that the meta-stable $Li_4SnSe_4^*$ to have an energy of 0.07 eV/formula unit higher in energy than the ground state structure, suggesting that it is less likely than $Li_4SnS_4^*$ to form at room temperature. The results are listed in Table I and in Table II.

Electronic Structure Results

In order to gain a qualitative understanding of the electronic structure of the various forms of of these materials, it is helpful to analyze the partial densities of states which are shown in Fig. 3. The partial density of states of $Li_4GeS_4^0$ in its ground state structure was previously presented in Ref. 27. While, density functional theory is known to systematically underestimate the band gaps, the relative band gaps are usually well represented. For these materials, Li_4GeS_4 has a computed bandgap of 2.1 eV, while the computed band gaps for Li_4SnS_4 and Li_4SnSe_4 are 2.2 eV and 1.6 eV respectively. For both of these
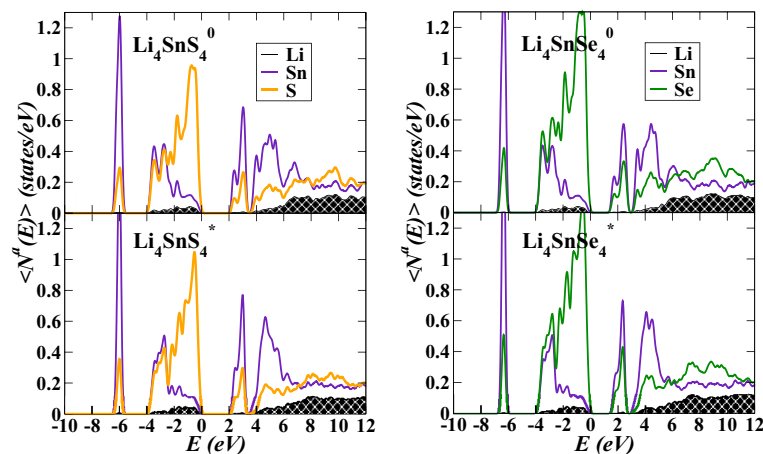
Figure 3. Partial densities of states for $Li_4SnS_4^0$ and $Li_4SnS_4^*$ (a) and $Li_4SnSe_4^0$ and $Li_4SnSe_4^*$ (b), separately indicating contributions from Li, Sn, S, and Se sites.

materials the upper part of the valence band is dominated by chalcogenide states while the conduction band is dominated by Sn $5s$ states forming a narrow band below the Sn $5p$ states. The results for Li_4SnS_4 presented in Fig. 3 are consistent with the results previously reported by MacNeil et al.[4] The partial densities of states for the ground state and meta-stable structures have nearly indistinguishable partial density of states curves. The materials are clearly insulating with band gaps expected to be larger than 2 eV found in the present study due to the systematic gap underestimation known for LDA calculations.

Another result from the electronic structure calculations is the total energies which approximate the internal energies at zero temperature. These can be used to study the stability of the materials relative to various possible reactions such as those listed in Table III. If the effects of zero point motion and finite temperature are small, the results can be related to experimental enthalpies. The values listed in this table correspond to the ground state structures of $Li_4SnCh_4^0$. Results for the meta-stable form of $Li_4SnCh_4^*$ can be determined by adding 0.02 eV or 0.07 eV for Ch=S or Ch=Se, respectively. Reaction 1 listed in Table III corresponds to the enthalpy of formation referenced to the standard states of the elements[28] including Li in the bcc structure, Sn in the diamond structure, S in the orthorhombic structure,[29] and Se in the trigonal structure.[30] Reaction 2 listed in Table III corresponds to decomposition into two binary materials. Li_2S and Li_2Se both form in the fluorite structure, while SnS_2 and $SnSe_2$ both form in the hexagonal CdI_2 structure. Our simulations indicate that the two reactions have opposite sign, meaning that Li_4SnS_4 is more stable than its binary products, while Li_4SnSe_4 is less stable. Reaction 3 listed in Table III involves two new materials with the stoichiometry Li_2SnCh_3. Recently, Brant et al.[31] synthesized and characterized Li_2SnS_3, finding it to have a densely packed layered structure. The electronic structure results indicate that Li_2SnS_3 together with excess Li_2S is more stable than Li_4SnS_4. Li_2SnSe_3 was recently synthesized by Kaib, Bron, et al.[5], characterized by one dimensional chains of SnS_4 tetrahedra. The electronic structure results indicate that this material together with excess Li_2Se has about the same stability as Li_4SnSe_4.

Figure 4. Ball and stick model of ground state structure of $Li_4SnS_4^0$ and $Li_4SnSe_4^0$ using the same ball convention and viewpoint as in Fig. 1(a). Distinct vacancy sites are indicated with their Wyckoff labels a_i, c_i, and d_i. Interstitial sites are colored green and are labeled I_i. Possible vacancy and interstitialcy trajectories are indicated with transparent purple and green arrows respectively.

Defect Structures and Ion Migration Paths in $Li_4SnS_4^0$, $Li_4SnS_4^*$, $Li_4SnSe_4^0$, and $Li_4SnSe_4^*$.

Point defects were modeled at fixed volume in $1 \times 2 \times 2$ supercells. For the ground state structure of $Li_4SnS_4^0$ and $Li_4SnSe_4^0$, there are three distinct Li ion vacancy sites which can be uniquely labeled by the Wyckoff letters a_i, c_i, and d_i as visualized in Fig. 4. The vacancy energies are listed in Table IV relative to the most stable vacancy at an a site.

Vacancy migration in $Li_4SnSe_4^0$ was previously studied by Kaib, Bron, et al.[5] who showed that a sequence of hops of the vacancy between the sites $a_1 \rightarrow c_1 \rightarrow d_1 \rightarrow a_2 \ldots$ results in net ion motion

Table III. Estimates of various reaction energies (in eV) for Li_4SnCh_4 for the calcogens Ch=S and Ch=Se based on total energy calculations. In each case the ground state structures of $Li_4SnCh_4^0$ was assumed; the structures of the products are mentioned in the text of the manuscript.

	Reaction	Ch=S	Ch=Se
1	$Li_4SnCh_4 \rightarrow 4Li + Sn + 4Ch$	−9.99	−8.94
2	$Li_4SnCh_4 \rightarrow 2Li_2Ch + SnCh_2$	−0.09	0.04
3	$Li_4SnCh_4 \rightarrow Li_2Ch + Li_2SnCh_3$	0.17	−0.01

Table IV. Relative energies (in eV) of vacancies in the ground state structures of $Li_4SnS_4^0$ and $Li_4SnSe_4^0$ calculated in $1 \times 2 \times 2$ supercells. The vacancy sites are indicated by their Wyckoff site labels with the zero energy chosen at the a site.

Vacancy label	$Li_4SnS_4^0$	$Li_4SnSe_4^0$
a	0.00	0.00
c	0.30	0.20
d	0.26	0.16

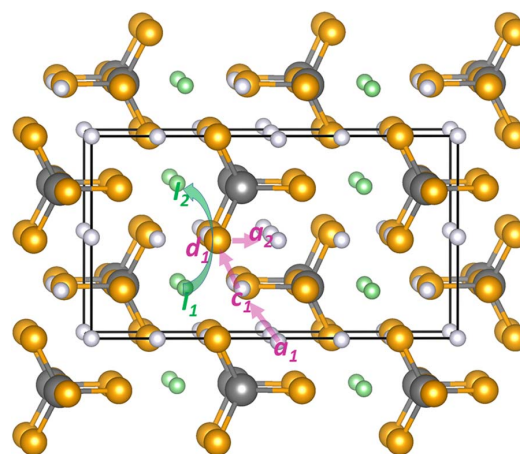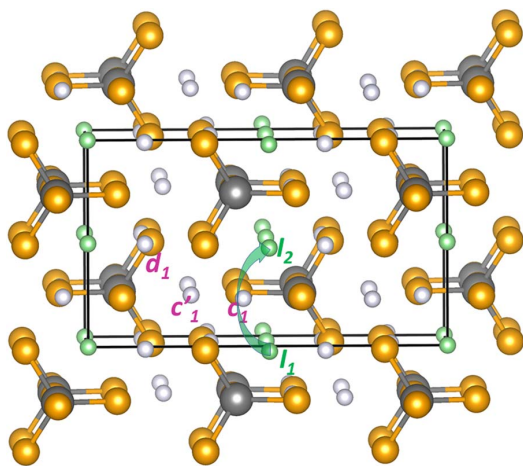**Figure 5.** Ball and stick model of ground state structure of $Li_4SnS_4^*$ and $Li_4SnSe_4^*$ using the same ball convention and viewpoint as in Fig. 1(b). Distinct vacancy sites are indicated with their Wyckoff labels c_i', c_i, and d_i. Interstitial sites are colored green and are labeled I_i. Possible interstitialcy trajectories are indicated with transparent green arrows.
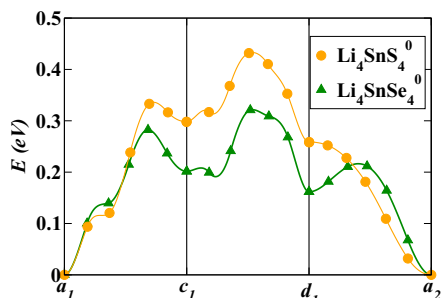

Figure 6. NEB calculated energy path diagram for Li ion vacancy migration in $Li_4SnS_4^0$ and $Li_4SnSe_4^0$. The vacancy site labels correspond to the diagram in Fig. 4.

in the b and c directions in the crystal as illustrated in Fig. 4. The corresponding energies along this path as calculated using the NEB method are shown in Fig. 6 and tabulated in Table V. From Table V we see that the vacancy hopping distances d are slightly smaller and the path energies are somewhat larger for $Li_4SnS_4^0$ compared with $Li_4SnSe_4^0$. The bottleneck of this process occurs during the $c_1 \rightarrow d_1$ step, resulting in the estimated migration energies of $E_m = 0.46$ eV and $E_m = 0.32$ eV for $Li_4SnS_4^0$ and $Li_4SnSe_4^0$, respectively. Another vacancy migration path for this involves vacancy hopping between the sites $a \rightarrow c \rightarrow a \rightarrow c \dots$ resulting in net migration along the b axis. The estimated migration energy for this path is $E_m = 0.33$ eV and $E_m = 0.28$ eV for $Li_4SnS_4^0$ and $Li_4SnSe_4^0$, respectively. We also investigated vacancy migration mechanisms along the a axis. The bottleneck for a axis vacancy migration involves hops between

Table V. NEB calculated migration energies (E_m) and ideal distances (d) for vacancy migration in $Li_4SnS_4^0$ and $Li_4SnSe_4^0$. Migration energies are referenced to a vacancy at the a site.

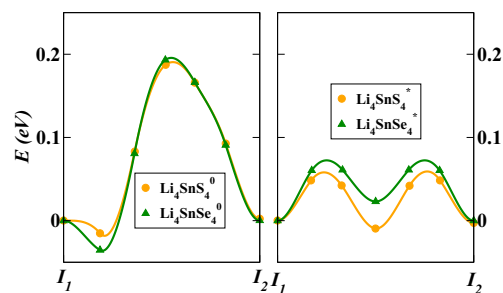|	$Li_4SnS_4^0$		$Li_4SnSe_4^0$	
	E_m (eV)	d (Å)	E_m (eV)	d (Å)
$a \rightarrow c$	0.33	3.3	0.28	3.5
$c \rightarrow d$	0.46	3.6	0.32	3.8
$d \rightarrow a$	0.26	2.8	0.21	2.9

Figure 7. NEB calculated energy path diagram for Li ion migration with an interstitialcy mechanism as shown in Fig. 4 for $Li_4SnS_4^0$ and $Li_4SnSe_4^0$ and as shown in Fig. 5 for $Li_4SnS_4^*$ and $Li_4SnSe_4^*$.

nearest neighbor d sites which raise the estimated migration energies substantially above the migration barriers along the b and c axes. In general there is good agreement between our calculated results for $Li_4SnSe_4^0$ and the corresponding results of Kaib, Bron, et al.,[5] within a small descrepancy of 0.03 eV or less.

For the meta-stable structure of $Li_4SnS_4^*$, only the c' site vacancy is stable. Calculations initialized with vacancies on c or d sites relax to a vacancy on nearby c' site. For the meta-stable structure of $Li_4SnSe_4^*$, the story is slightly different. For that system, the c' site vacancy is again the most stable. Calculations initialized with vacancies on a c site relax to a vacancy on a nearby c' site. Calculations initialized with vacancies on a d site are meta-stable with considerable distortion, having an energy of 0.24 eV above the energy of the c' site vacancy. We did not investigate vacancy migration mechanisms in the meta-stable structures.

Another important mechanism for ion migration involves interstitial sites. For the ground state structures of $Li_4SnS_4^0$ and $Li_4SnSe_4^0$ there is one main interstitial site located in the void regions between SnS_4 or $SnSe_4$ tetrahedra as shown in Fig. 4 which happens to be the c' Li site of the meta-stable $Li_4SnS_4^*$ and $Li_4SnSe_4^*$ structures. Correspondingly, for the meta-stable structures of $Li_4SnS_4^*$ and $Li_4SnSe_4^*$ the one main interstitial site is located in the void regions which happens to be the a site of the ground state structures as shown in Fig. 5. For both structures, migration between these interstitial sites occurs most efficiently using an "interstitialcy" mechanism. An interstitialcy mechanism is one in which an interstitial ion moves into a host lattice site as that host lattice ion moves to an adjacent interstitial site. The resulting migration processes for $Li_4SnS_4^0$ and $Li_4SnSe_4^0$, with an intermediate d host lattice site, and for $Li_4SnS_4^*$ and $Li_4SnSe_4^*$, with an intermediate c host lattice site, are illustrated with the green arrows in Figs. 4 and 5 and the corresponding NEB energy paths are shown in Fig. 7.

From the energy path diagram shown in Fig. 7, it is evident that the interstitialcy mechanism results in the lowest migration barrier for all of the structures investigated and is predicted to dominate migration processes. For electrolytes in the so-called "intrinsic" regime, the NEB estimate of the activation energy E_A^{NEB} for conductivity is related to the migration energy E_m and the formation energy E_f to form a vacancy and interstitial pair according to

$$E_A^{NEB} = E_m + \frac{1}{2}E_f. \quad [1]$$

A summary of results including optimal calculated values of E_A^{NEB} from Eq. 1 and available experimental values are listed in Table VI. For the ground state structures of $Li_4SnS_4^0$ and $Li_4SnSe_4^0$ the calculated optimal values of E_f were obtained for vacancies on an a site moving to the nearest interstitial site $I c'$ which corresponds to the site we've called c' in the meta-stable structures. The calculated values of E_f are 0.27 eV and 0.36 eV for $Li_4SnS_4^0$ and $Li_4SnSe_4^0$, respectively. The corresponding estimates of the activation energies E_A^{NEB} are 0.3 eV and 0.4 eV for $Li_4SnS_4^0$ and $Li_4SnSe_4^0$, respectively. To the best of our

Table VI. Activation energies for ion migration for ground state and meta-stable state structures of Li$_4$SnS$_4$ and Li$_4$SnSe$_4$. Calculated migration energies E_m were determined from NEB calculations of the interstitialcy mechanism shown in Fig. 7. Formation energies E_f for interstitial-vacancy pairs, calculated activation energies E_A^{NEB} based on Eq. 1 and literature values of the activation energy E_A^{exp} are also listed. For comparison, the calculated activation energies E_A^{trace} and their error estimates associated with the Arrhenius temperature dependence of the simulated "tracer" diffusion coefficients $D^{trace}(T)$ are also listed here and will be discussed in the Molecular dynamics section.

	E_m (eV)	E_f (eV)	E_A^{NEB} (eV)	E_A^{exp} (eV)	E_A^{trace} (eV)
Li$_4$SnS$_4^0$	0.19	0.27	0.3		0.24 ± 0.06
Li$_4$SnS$_4^*$	0.06	0.15	0.1	0.41[a]	0.25 ± 0.04
Li$_4$SnSe$_4^0$	0.20	0.36	0.4	0.45[b]	0.23 ± 0.1
Li$_4$SnSe$_4^*$	0.07	0.15	0.1		0.08 ± 0.01

[a]Ref. 3.
[b]Ref. 5.

knowledge, there are no published conductivity measurements for the Li$_4$SnS$_4^0$ material, but Li$_4$SnSe$_4^0$ has been well studied by Kaib, Bron, et al.[5] Our NEB calculated result for Li$_4$SnSe$_4^0$ is in disagreement with the value of 0.6 eV calculated by Kaib, Bron, et al.,[5] but is in better agreement with the value of $E_A = 0.45$ eV deduced from fitting the temperature dependence of the experimental conductivity measurements in the same study.

For the meta-stable structures of Li$_4$SnS$_4^*$ and Li$_4$SnSe$_4^*$, the calculated optimal values of E_f were obtained for vacancies on an c' site moving to the nearest interstitial site Ia which corresponds to the a site in the ground state structures. The calculated values of E_f are 0.15 eV for both Li$_4$SnS$_4^*$ and Li$_4$SnSe$_4^*$, resulting in estimates of the activation energies E_A^{NEB} of 0.1 eV for both materials. This result is not in agreement with the value of $E_A = 0.41$ eV obtained from fitting the temperature dependence of the experimental conductivity measured by Kaib, Haddadpour, et al.[3]

Molecular Dynamics Simulations

In studying the ion migration mechanisms for the Li$_4$SnCh$_4^0$ and Li$_4$SnCh$_4^*$ structures, we find the Li ion motions to be highly correlated presumably due to a complicated energy landscape. For example, in creating single defects in an otherwise perfect lattice, we found some of the configurations to be unstable. For example, in the Li$_4$SnS$_4^0$ structure, a d site vacancy is unstable relative to a vacancy on the nearest a site Li. In the Li$_4$SnS$_4^*$ structure a d site vacancy is unstable relative to a vacancy on the nearest c' site Li. The NEB analysis discussed in the previous section was unable to completely explain the conductivity results. In order to get additional information about the migration processes, we performed molecular dynamics simulations using the QUANTUM ESPRESSO[12] code. While the NEB method gives insight about the probability of individual hops of the migrating Li ions, molecular dynamics simulations provide information about the motions of the ensemble of ions within the simulation cell. As shown by Mo, Ong, and others,[32–35] one way to improve the configuration sampling of the simulations is to perform the simulations at elevated temperatures. The expectation (although unproven) is that the behaviors of the materials at room temperature can be estimated from the extrapolated simulation results.

Figure 8 shows a visualization of the Li mobility with a ball and stick model of the crystals with superposed Li positions at 136 time steps at intervals of 0.05 ps. It is apparent from these diagrams that at the relatively low simulation temperatures of $T = 635$ K and $T = 656$ K there is substantial motion of all of the Li ions. In addition to the vacancy and interstitialcy mechanisms studied by the NEB analysis as discussed above, several other pathways for Li ion motion are evident.

In order to better analyze the molecular dynamics simulations, it is convenient to define a site occupancy factor as a function of time $s_i(t)$ where i denotes the site type. For the ground state structure, the sites were labeled according to their host site type (a, c, or d) or the interstitial site type (Ic'). For the meta-stable state structure, the sites were labeled according to their host site type (c', c, or d) or the interstitial site type (Ia). The site label i was determined from the

closest Li position of the perfect lattice relative to the instantaneous position of each Li. For convenience, the site occupancy factors were normalized to unity at full occupancy and followed the sum rule:

$$\sum_i s_i(t) \frac{n_i}{N} = 1, \qquad [2]$$

where n_i denotes the multiplicity of the site and N denotes the total number of Li sites. For the materials in this study, $n_d/N = 2n_j/N$, where j indexes the a, c, or c' sites and d denotes the d site type. As shown in Fig. 9, the instantaneous site occupancy factors $s_i(t)$ are very noisy and it is convenient to define a time averaged site occupancy parameter

$$\langle s_i \rangle_t \equiv \frac{1}{t} \int_0^t s_i(t') dt'. \qquad [3]$$

As shown in Fig. 9, $\langle s_i \rangle_t$ tends to an asymptotic value at long times.

It is interesting to study the asymptotic time averaged site occupancy factors $\langle s_i \rangle_{t \to \infty} \equiv \langle s_i \rangle$ as a function of simulation temperatures for the four materials as shown in Fig. 10. These values were determined from the final time step of each simulation which was between 3 and 8 ps. The values of $\langle s_i \rangle$ for Li$_4$SnS$_4^0$ and Li$_4$SnSe$_4^0$ structures show relative small values (<0.5) for the interstitial Ic' site and relative large values (>0.75) for the host lattice sites (a, c, and d), indicating a relatively well-ordered structure. On the other hand for the Li$_4$SnS$_4^*$ and Li$_4$SnSe$_4^*$ structures, the interstitial sites (Ia) are substantially occupied (>0.5) throughout the temperature range, indicating relatively disordered structures.

It is possible to use molecular dynamics results in a more quantitative analysis of ionic conductivity following the approach implemented by Mo, Ong, and others.[32–35] For a molecular dynamics simulation at temperature T with resultant ion trajectories $\{\mathbf{r}_i(t)\}$ as a function of time t, one can calculate the mean squared displacement and use Einstein's expression to determine the diffusion constant $D_{trace}(T)$:[36]

$$\left\langle \frac{1}{6N} \sum_{i=1}^N |\mathbf{r}_i(t) - \mathbf{r}_i(t_0)|^2 \right\rangle = D_{trace}(T)[t - t_0] + C. \qquad [4]$$

Here the summation over i denotes the N Li ion positions $\{\mathbf{r}_i(t)\}$ in the simulation cell and C denotes a constant. In order to improve the sampling of the simulation, the incremental distance is averaged over the initial times t_0 as implied by the angular brackets in the expression. As pointed out by Murch,[37–39] the temperature dependent diffusion constant $D_{trace}(T)$ calculated from the mean squared displacement in this way approximates the diffusion of tracked particles such that can experimentally realized in radioactive tracer experiments. Since diffusion takes place near equilibrium, it is reasonable to also assume that the diffusion coefficient has an Arrhenius temperature dependence[40]

$$D_{trace}(T) = D_{trace}(0) e^{-E_A^{trace}/kT}, \qquad [5]$$

where $D_{trace}(0)$ denotes the diffusion coefficient at 0 K, E_A^{trace} denotes the activation energy for diffusion, and k denotes the Boltzmann constant.
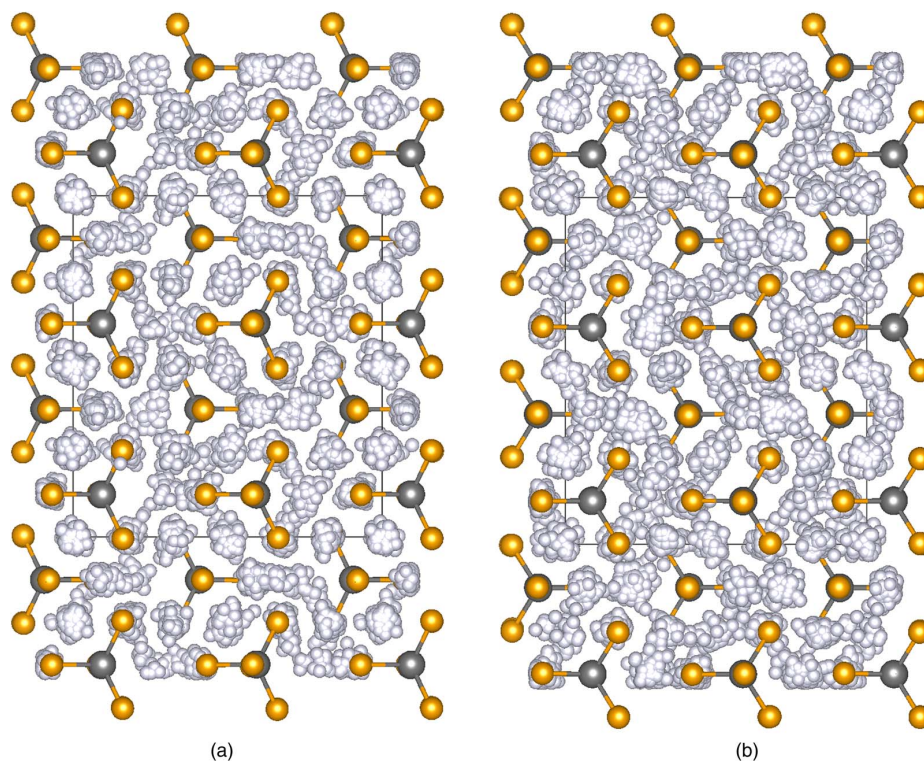
Figure 8. Ball and stick diagrams of molecular dynamics simulations for $Li_4SnS_4^0$ at $T = 635$ K (a) and $Li_4SnS_4^*$ at $T = 656$ K (b). Initial Sn and S positions are represented by gray and orange balls respectively. Li positions of the initial configuration and 136 subesquent positions at time intervals of 0.05 ps are indicated with gray balls. Simulations were performed using microcanonical ensembles (constant energy and volume) in $1 \times 2 \times 2$ supercells. The viewpoint is a projection down the c-axis.

The temperature dependent direct-current ionic conductivity is related to $D_{trace}(T)$ by the equation[38]

$$\sigma(T) = \frac{\rho q^2}{kT} \frac{D_{trace}(T)}{H},$$ [6]
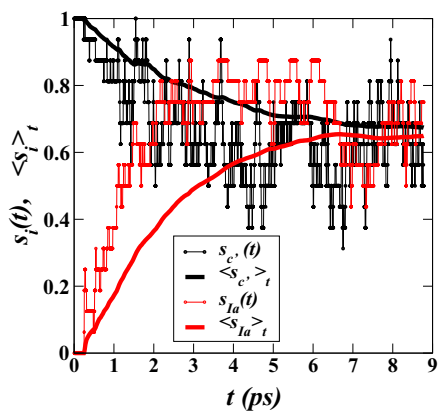
Figure 9. Instantaneous and time averaged site occupancy factors for molecular dynamics simulation of $Li_4SnS_4^*$ at a temperature of $T = 830$ K.
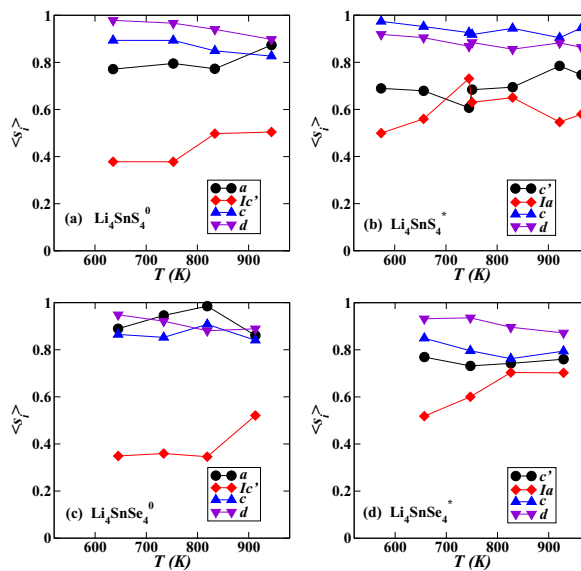
Figure 10. Asymptotic time averaged site occupancy factors $\langle s_i \rangle$ for (a) $Li_4SnS_4^0$, (b) $Li_4SnS_4^*$, (c) $Li_4SnSe_4^0$ and (d) $Li_4SnSe_4^*$ evaluated at various simulation temperatures.
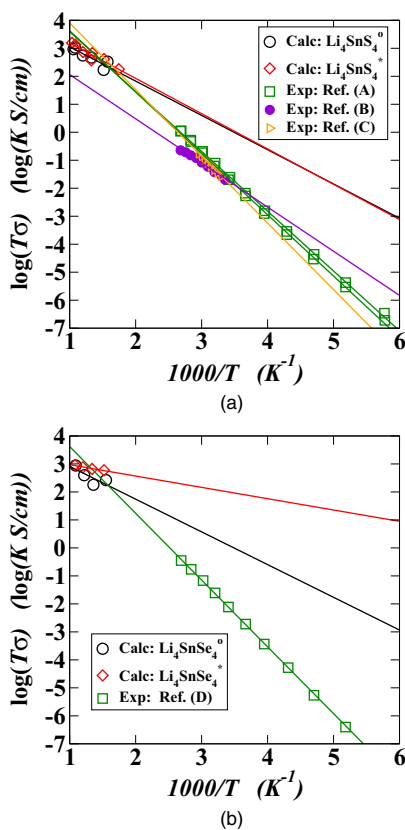
Figure 11. Plots of the ionic conductivity in terms of $\log(T\sigma)$ of Li_4SnS_4 (a) and Li_4SnSe_4 (b). The calculated values were evaluated using Eq. 6 with $H = 1$. The experimental values for $Li_4SnS_4^*$ were taken from Refs. 3 (A), 6 (B), and 7 (C), while experimental results for $Li_4SnSe_4^0$ were taken from Ref. 5 (D). All of the experimental values were analyzed from the published graphs using digitizing software. The lines represent least squares fits to the calculated results or the digitized experimental values.

where ρ denotes the number of mobile ions (Li) per unit volume, q denotes the charge of each Li ion. The factor H is known as the Haven ratio[41] which takes into account so called correlation effects. For example, the conductivity due to an interstitialcy process which involves the concerted motion of interstitial and host ions as discussed above, is not well modeled by the mean squared displacements of independent ions. If the temperature dependence of the Haven ratio H were trivial, the activation energy for tracer diffusion E_A^{trace} would also approximate the activation energy of the conductivity according to Eq. (6). A simulation to estimate the Haven ratio[42] is beyond the scope of the present work. On the other hand, comparing a calculation of the conductivity using Eq. (6) assuming $H = 1$, with experiment, can provide information on the Haven ratios for these materials.

Figure 11 summarizes the simulation results in comparison with experimental conductivity measurements. The conductivity of $Li_4SnS_4^*$ was measured by 3 independent groups,[3,6,7] showing very similar results. The small differences among the experimental conductivity results shown in Fig. 11a may be due to digitization errors. The digitized data from these experiments are consistent with the Arrhenius activation energy of $E_A^{exp} = 0.4 \pm 0.1$ eV. The simulation results reported here should be regarded as preliminary, due to the relatively small number of configurations sampled. Previous work of this sort[32–35] was based on simulation times 10-100 times as long as our 3-8 ps simulations. For these reasons, the least squares fit lines

through the simulated results for $\log(T\sigma)$ versus $1000/T$ should be considered with large error bars.

Mindful of the limitations, it is nevertheless interesting to analyze the simulation results obtained in this study. Despite the differences in their site occupancies, the computed tracer diffusion behaviors of $Li_4SnS_4^0$ and $Li_4SnS_4^*$ shown in Fig. 11a were found to be similar. The magnitudes of the high temperature simulated conductivities is in the range of the extrapolated experimental conductivities. By fitting a straight line through the simulated conductivities, the deduced values of the tracer activation energies are $E_A^{trace} = 0.24 \pm 0.06$ eV and 0.25 ± 0.04 eV for $Li_4SnS_4^0$ and $Li_4SnS_4^*$ respectively as listed in Table VI. The reported errors of the activation energies are likely underestimates, since they include only errors due to the linear fit and not the additional sampling errors of the simulation. However, these errors suggest that the activation energies for Li ion diffusion in these materials may differ by as much as 0.1 eV. While the tracer diffusion result for $Li_4SnS_4^0$ is consistent with the NEB result, the tracer diffusion result for $Li_4SnS_4^*$ is not in agreement either with experiment or with the NEB estimate for the activation energies. For the selenide materials shown in Fig. 11b, the magnitudes of the high temperature simulated conductivities are again in the range of the extrapolated experimental conductivity. However, in contrast with sulfide materials, the deduced values of the tracer activation energies are distinct; $E_A^{trace} = 0.23 \pm 0.1$ eV and 0.08 ± 0.01 eV for $Li_4SnSe_4^0$ and $Li_4SnSe_4^*$ respectively as listed in Table VI. The activation energy for tracer diffusion in $Li_4SnSe_4^0$ is smaller than both the values obtained from experimental conductivity measurements and from the NEB calculations. However, the computed E_A^{trace} value for $Li_4SnSe_4^*$ happens to agree well with the NEB estimate of the activation energy E_A^{NEB} which was based on an idealized interstitialcy mechanism. In future work, the molecular dynamics simulations could be improved by reducing the sampling errors in terms of the finite size effects, increasing the simulation times, and considering multiple initial configurations. Additionally, it may be important to go beyond the constant volume simulations and to include the effects of lattice expansion. For example, in the Li_4SnS_4 system, the lattice contraction accounts for an energy gain of 0.03 eV/formula unit. One can guess that the constant volume simulations might bias the systems to result in distinct configurations at high temperature. Perhaps more realistic representations of the volumetric variations with temperature could be used to investigate possible transitions between the structural forms. In addition to these possible numerical improvements, some of the discrepancies of the measured and simulated conductivities come from the Haven ratio which is expected to be non-trivial for these materials due to the importance of the interstitialcy mechanism.

Conclusions

Our simulations identify ideal ground state structures for $Li_4GeS_4^0$, $Li_4SnS_4^0$, and $Li_4SnSe_4^0$ and ideal meta-stable structures $Li_4GeS_4^*$, $Li_4SnS_4^*$, and $Li_4SnSe_4^*$. The meta-stable structures differ from the ground state configurations by the removal of the a site Li's to the so-called c' sites and the contraction of the a axis lattice parameter by approximately 0.5 Å. The ground state structures have been experimentally reported for $Li_4GeS_4^0$, $Li_4SnS_4^0$, and $Li_4SnSe_4^0$ in References 4, 4, and 5, respectively. Our ideal meta-stable structure is consistent with the structure of $Li_4SnS_4^*$ reported by Reference 3 and corroborated by References 6 and 7.

Based on these ideal structures, Li ion migration processes were computationally examined for $Li_4SnS_4^0$, $Li_4SnS_4^*$, $Li_4SnSe_4^0$, and $Li_4SnSe_4^*$. Considering simple defects and NEB analysis, we find interstitialcy mechanisms in all of these materials to provide efficient motion of the Li ions primarily along the b and c lattice directions. The small "formation energy" involved with moving a Li ion from a host lattice site into an interstitial site resulting in a interstitial-vacancy pair, $E_f = 0.15$ eV for both $Li_4SnS_4^*$ and $Li_4SnSe_4^*$ implies that these structures are likely to be disordered at relatively low temperatures as suggested by the original analysis of Kaib, Haddadpour, et al.[3] The

simulations indicate that the corresponding formation energy is larger for the ground state structures, where $E_f = 0.27$ eV for $Li_4SnS_4^0$ and $E_f = 0.36$ eV for $Li_4SnSe_4^0$, suggesting that these structures are likely to remain ordered at relatively low temperatures. At the present time, experimental measurements of the activation energy for ion conductivity are available only for $Li_4SnSe_4^0$ and $Li_4SnS_4^*$. As shown in Table VI, the NEB estimate of E_A^{NEB} for $Li_4SnSe_4^0$ is in reasonable agreement with experiment assuming an interstitialcy mechanism. On the other hand, the NEB estimate of E_A^{NEB} for $Li_4SnS_4^*$ is not in good agreement with experiment, presumably because significant contributions from more complicated configurations than the pure interstitialcy mechanism are important of ion migration in this case. Molecular dynamics simulations performed at temperatures of $T = 600K$ and higher indicate that there is significant motion of all of the Li ions including appreciable occupancy of the interstitial sites for all of the structures. Plots of the site occupancy parameters from the molecular dynamics simulations shown in Fig. 10 are consistent with the notion that the ground state structures remain more ordered for a larger temperature range than do the meta-stable structures. Sequences of the molecular dynamics steps identify the interstitialcy mechanism as well as more complicated motions which contribute to the Li ion mobility. While these molecular dynamics studies, provide interesting insight into the properties of these materials, further work is needed to reconcile the calculated tracer diffusion simulations to quantitative estimates of the ion conductivity as shown in Fig. 11. In principle if the numerical accuracy and physical approximations could be improved, it would be reasonable to attribute the difference between the tracer diffusion simulations and the conductivity measurements to the Haven ratio. However, the error bars of the present work are too large to make this connection at the present time.

The simulations suggest that both Li_4SnS_4 and Li_4SnSe_4 have two ideal phases. The current literature suggests that the ground state structure is accessible by higher temperature processing while the meta-stable structure is formed at lower temperatures. For $Li_4SnS_4^0$, MacNeil et al.[4] report their highest synthesis temperature as 1023 K, while for $Li_4SnS_4^*$, Sahu et al.[6] report the highest synthesis temperature as 723 K. Understanding how to control the physical realization of these two phases, and possibly observing the phase transition might be of interest for future investigations.

References

1. Y. Wang, W. D. Richards, S. P. Ong, L. J. Miara, J. C. Kim, Y. Mo, and G. Ceder, *Nature Materials*, **14**, 1026 (2015).
2. J. Li, C. Ma, M. Chi, C. Liang, and N. J. Dudney, *Advanced Energy Materials*, **5**, 1401408 (2015).
3. T. Kaib, S. Haddadpour, M. Kapitein, P. Bron, C. Schrder, H. Eckert, B. Roling, and S. Dehnen, *Chemistry of Materials*, **24**, 2211 (2012).
4. J. H. MacNeil, D. M. Massi, J.-H. Zhang, K. A. Rosmus, C. D. Brunetta, T. A. Gentile, and J. A. Aitken, *Journal of Alloys and Compounds* (2013).
5. T. Kaib, P. Bron, S. Haddadpour, L. Mayrhofer, L. Pastewka, T. T. Jrvi, M. Moseler, B. Roling, and S. Dehnen, *Chemistry of Materials*, **25**, 2961 (2013).
6. G. Sahu, Z. Lin, J. Li, Z. Liu, N. Dudney, and C. Liang, *Energy Environ. Sci.*, **7**, 1053 (2014).
7. K. H. Park, D. Y. Oh, Y. E. Choi, Y. J. Nam, L. Han, J.-Y. Kim, H. Xin, F. Lin, S. M. Oh, and Y. S. Jung, *Advanced Materials*, **28**, 1874 (2016).
8. P. Hohenberg and W. Kohn, *Physical Review*, **136**, B864 (1964).
9. W. Kohn and L. J. Sham, *Physical Review*, **140**, A1133 (1965).
10. P. E. Blöchl, *Phys. Rev. B*, **50**, 17953 (1994).
11. N. A. W. Holzwarth, A. R. Tackett, and G. E. Matthews, *Computer Physics Communications*, **135**, 329 (2001), available from the website http://pwpaw.wfu.edu.
12. P. Giannozzi, S. Baroni, N. Bonini, M. Calandra, R. Car, C. Cavazzoni, D. Ceresoli, G. L. Chiarotti, M. Cococcioni, I. Dabo, A. D. Corso, S. de Gironcoli, S. Fabris, G. Fratesi, R. Gebauer, U. Gerstmann, C. Gougoussis, A. Kokalj, M. Lazzeri, L. Martin-Samos, N. Marzari, F. Mauri, R. Mazzarello, S. Paolini, A. Pasquarello, L. Paulatto, C. Sbraccia, S. Scandolo, G. Sclauzero, A. P. Seitsonen, A. Smogunov, P. Umari, and R. M. Wentzcovitch, *J. Phys.: Condens. Matter*, **21**, 394402 (19pp) (2009), available from the website http://www.quantum-espresso.org.
13. X. Gonze, B. Amadon, P. M. Anglade, J. M. Beuken, F. Bottin, P. Boulanger, F. Bruneval, D. Caliste, R. Caracas, M. Cote, T. Deutsch, L. Genovese, P. Ghosez, M. Giantomassi, S. Goedecker, D. R. Hamann, P. Hermet, F. Jollet, G. Jomard, S. Leroux, M. Mancini, S. Mazevet, M. J. T. Oliveira, G. Onida, Y. Pouillon, T. Rangel, G. M. Rignanese, D. Sangalli, R. Shaltaf, M. Torrent, M. J. Verstraete, G. Zerah, and J. W. Zwanziger, *Computer Physics Communications*, **180**, 2582 (2009), code is available at the website http://www.abinit.org.
14. A. Kokalj, *Journal of Molecular Graphics and Modelling*, **17**, 176 (1999), code available at the website http://www.xcrysden.org.
15. A. Kokalj, *Computational Materials Science*, **28**, 155 (2003).
16. K. Momma and F. Izumi, *Applied Crystallography*, **44**, 1272 (2011), code available from the website http://jp-minerals.org/vesta/en/.
17. J. P. Perdew and Y. Wang, *Phys. Rev. B*, **45**, 13244 (1992).
18. Y. A. Du and N. A. W. Holzwarth, *Phys. Rev. B*, **76**, 174302 (14 pp) (2007).
19. Y. A. Du and N. A. W. Holzwarth, *Phys. Rev. B*, **81**, 184106 (15pp) (2010).
20. Z. D. Hood, C. Kates, M. Kirkham, S. Adhikari, C. Liang, and N. A. W. Holzwarth, *Solid State Ionics*, **284**, 61 (2015).
21. N. D. Lepley, N. A. W. Holzwarth, and Y. A. Du, *Phys. Rev. B*, **88**, 104103 (11 pp) (2013).
22. H. Jónsson, G. Mills, and K. W. Jacobsen, in *Classical and Quantum Dynamics in Condensed Phase Simulations*, edited by B. J. Berne, G. Ciccotti, and D. F. Coker (World Scientific, Singapore, 1998) pp. 385.
23. G. Henkelman, B. P. Uberuaga, and H. Jónsson, *J. Chem. Phys.*, **113**, 9901 (2000).
24. G. Henkelman and H. Jónsson, *J. Chem. Phys.*, **113**, 9978 (2000).
25. T. Hahn, ed., *International Tables for Crystallography, Volume A: Space-group symmetry, Fifth revised edition* (Kluwer, 2002) ISBN 0-7923-6590-9. The symmetry labels used in this work are all based on this reference.
26. "Mercury 3.5.1", (2014), developed and distributed by the Cambridge Crystallographic Data Centre http://www.ccdc.cam.ac.uk/mercury/.
27. A. Al-Qawasmeh and N. A. W. Holzwarth, *Journal of the Electrochemical Society*, **163**, A2079 (2016).
28. D. R. Lide, ed., *CRC Handbook of Chemistry and Physics, 90th Edition* (CRC Press, Taylor & Francis Group, 2009) ISBN 13: 978-1-4200-9084-0.
29. S. J. Rettig and J. Trotter, *Acta Cryst. C*, **43**, 2260 (1987).
30. R. Keller, W. B. Holzapfel, and H. Schulz, *Physical Review B*, **16**, 4404 (1977).
31. J. A. Brant, D. M. Massi, N. A. W. Holzwarth, J. H. MacNeil, A. P. Douvalis, T. Bakas, S. W. Martin, M. D. Gross, and J. A. Aitken, *Chemistry of Materials*, **27**, 189 (2015).
32. Y. Mo, S. P. Ong, and G. Ceder, *Chemistry of Materials*, **24**, 15 (2012).
33. S. P. Ong, Y. Mo, W. D. Richards, L. Miara, H. S. Lee, and G. Ceder, *Energy & Environmental Science*, **6**, 148 (2013).
34. Z. Zhu, I.-H. Chu, Z. Deng, and S. P. Ong, *Chemistry of Materials*, **27**, 8318 (2015).
35. Y. Deng, C. Eames, J.-N. Chotard, F. Lalre, V. Seznec, S. Emge, O. Pecher, C. P. Grey, C. Masquelier, and M. S. Islam, *Journal of the American Chemical Society*, **137**, 9136 (2015).
36. J. M. Haile, *Molecular Dynamics Simulations* (John Wiley & Sons, Inc., 1992).
37. G. E. Murch, *Philosophical Magazine A*, **45**, 685 (1982).
38. G. E. Murch, *Solid State Ionics*, **7**, 177 (1982).
39. G. E. Murch, *J. Phys. Chem. Solids*, **46**, 53 (1985).
40. J. Maier, *Physical Chemistry of Ionic Materials* (John Wiley & Sons, Ltd., 2004).
41. K. Compaan and Y. Haven, *Trans. Faraday Soc.*, **54**, 1498 (1958).
42. B. J. Morgan and P. A. Madden, *Physical Review Letters*, **112** (2014).

Appendix C

First principles simulations of Li$_2$OHCl

Fundamental aspects of the structural and electrolyte properties of Li$_2$OHCl from simulations and experiment

Jason Howard,[1] Zachary D. Hood,[2,3] and N. A. W. Holzwarth[1,*]

[1]*Department of Physics, Wake Forest University, Winston-Salem, NC 27109-7507, USA*
[2]*Center for Nanophase Materials Sciences, Oak Ridge National Laboratory, Oak Ridge, TN 37831, USA*
[3]*School of Chemistry and Biochemistry, Georgia Institute of Technology, Atlanta, GA 30332, USA*

Solid-state electrolytes that are compatible with high-capacity electrodes are expected to enable the next generation of batteries. As a promising example, Li$_2$OHCl was reported to have good ionic conductivity and to be compatible with a lithium metal anode even at temperatures above 100 °C. In this work, we explore the fundamental properties of Li$_2$OHCl by comparing simulations and experiments. Using calculations based on density functional theory, including both static and dynamic contributions through the quasiharmonic approximation, we model a tetragonal ground state, which is not observed experimentally. An ordered orthorhombic low-temperature phase was also simulated, agreeing with experimental structural analysis of the pristine electrolyte at room temperature. In addition, comparison of the ordered structures with simulations of the disordered cubic phase provide insight into the mechanisms associated with the experimentally observed abrupt increase in ionic conductivity as the system changes from its ordered orthorhombic to its disordered cubic phase. A large Haven ratio for the disordered cubic phase is inferred from the computed tracer diffusion coefficient and measured ionic conductivity, suggesting highly correlated motions of the mobile Li ions in the cubic phase of Li$_2$OHCl. We find that the OH bond orientations participate in gating the Li ion motions which might partially explain the predicted Li-Li correlations.

I. INTRODUCTION

The drive to produce all-solid-state batteries has led to exploration of novel solid-state materials that can replace traditional liquid electrolytes. There are many factors that determine whether a material can be used in an electrochemical cell, with one of the most important being that it is a very good ionic conductor. With the demand for batteries to have large energy and volumetric densities, all solid-state lithium ion batteries are very promising. In a battery, the electrolyte functions to allow transport of the energy storing ion between the electrodes while preventing the passage of electrons. This allows for the electrons to be passed through an external circuit and do work. An efficient mechanism that often results in high mobility of the "working" ion involves lattice structures with fractionally occupied (disordered) sites for the working ion.

Recently, two independent experimental investigations [1,2] showed that introducing defects into the disordered phase of crystalline Li$_2$OHCl can enhance its Li ion conductivity, suggesting this system to be very promising as an electrolyte material for all solid-state Li ion batteries. Earlier studies reported that Li$_2$OHCl and related materials have a low-temperature orthorhombic structure [3,4] having low ionic conductivity and a high-temperature cubic structure [3–5] having increased ionic conductivity. The temperature of the phase transition has been reported [1,4] to be approximately 35 °C, depending upon sample preparation. In fact, very little is known about the low-temperature phase of Li$_2$OHCl other than its reported [3,4] orthorhombic structure. In this work, we report a detailed experimental and computational study of pure Li$_2$OHCl in both its low- and high-temperature structures

in order to understand their fundamental properties and their relationships to the electrolyte capabilities of this material.

II. METHODS

A. Computational methods

In this work, computations were based on density functional theory [6,7] using the projector augmented wave (PAW) formalism [8]. The ATOMPAW code [9] was used to generate the PAW basis and projector functions, and the solid-state materials were modeled with periodic boundary conditions using the QUANTUM ESPRESSO software package [10]. The software packages VESTA [11] and XCRYSDEN [12] were used for visualizations of structural properties at the atomic level, and FINDSYM [13] helped in space-group analysis of the structures. MATLAB [14] was used in the quasiharmonic analysis of the Helmholtz free energy on a three-dimensional grid of lattice parameters. It was also used in visualizing histograms of the OH orientations.

The exchange-correlation functional was approximated using the local-density approximation [15] (LDA). The choice of LDA functional was made based on previous investigations [16–18] of similar materials which showed that provided that the lattice constants are scaled by a correction factor of 1.02, the simulations are in good agreement with experiment, especially lattice vibrational frequencies and heats of formation.

In general, self-consistent field and structural optimization calculations were well converged with a plane-wave expansion of wave vectors and reciprocal lattice vectors including $|\mathbf{k} + \mathbf{G}|^2 \leqslant 64$ Ry. However, a larger plane-wave expansion including $|\mathbf{k} + \mathbf{G}|^2 \leqslant 90$ Ry was needed for using density functional perturbation theory, which involves evaluating derivatives with respect to atomic displacements [19–21],

for the simulations of the phonon modes, as discussed in Sec. III A 2. For converging the electronic structures of the tetragonal and orthorhombic structures, zone-centered **k**-point grids of $12 \times 12 \times 12$ and $12 \times 12 \times 6$ were used, respectively. The total energy tolerance of the self-consistent field calculations was set to 10^{-12} Ry and the resulting forces were converged within 7×10^{-4} eV/Å. The phonon density of states was calculated with an energy convergence parameter of 10^{-14} Ry for the density functional perturbation self-consistent cycles. The interatomic force constants were calculated from density functional perturbation theory using $3 \times 3 \times 3$ and $3 \times 3 \times 2$ zone-centered phonon **q**-point grids for the tetragonal and octahedral structures, respectively. The resultant force constants were then interpolated to evaluate the phonon density of states using the finer **q**-point mesh of $10 \times 10 \times 10$ and $10 \times 10 \times 5$ for the tetragonal and orthorhombic structures, respectively. The acoustic sum rule was imposed along the diagonal elements of the dynamical matrices [21] at $q = 0$.

In order to simulate the disordered cubic structures, the numerical accuracy of the calculations could be relaxed while ensuring that energy differences were calculated with errors less than 7×10^{-4} eV/formula-unit. The plane-wave expansion included $|\mathbf{k} + \mathbf{G}|^2 \leqslant 45$ Ry and the energy tolerance of the self-consistent field was set to 10^{-8} Ry. For simulations based on supercell sizes $2 \times 2 \times 2$, $3 \times 3 \times 3$, $4 \times 4 \times 4$, and $5 \times 5 \times 5$, using the corresponding zone-centered **k**-point sampling grids of $3 \times 3 \times 3$, $2 \times 2 \times 2$, $1 \times 1 \times 1$, and $1 \times 1 \times 1$, respectively. The molecular dynamics simulations were performed using $3 \times 3 \times 3$ supercells using a single zone-centered **k** point to sample the Brillouin zone. A time step of 0.96 fs was used for all simulations. Each simulation was done using the microcanonical ensemble (NVE). The temperature was controlled by initializing the atoms of the relaxed supercell with Boltzmann distribution of velocities corresponding to twice the target temperature. We found that within the first 0.03 ps of the simulation run, the temperature typically dropped to approximately its target temperature. Simulations were carried out for 60–135 ps. Throughout the simulations, we found that the total energy remained constant except for a small drift per formula unit of 6×10^{-7} eV/fs and a corresponding positive drift in the simulation temperature.

B. Experimental methods

In previous work [1], the "fast-cooled" samples of Li_2OHCl were reported. In this work, we focus on "slow-cooled" samples in order to make it easier to compare with model calculations. The synthesis of slow-cooled Li_2OHCl was based on the methods previously reported [1]. All reagents were dried under vacuum at 90 °C for 4 h prior to use. LiOH (Sigma Aldrich, $\geqslant 98\%$) and LiCl (Sigma Aldrich, $\geqslant 99\%$) were mixed in a nickel crucible and sealed with a copper gasket in a bomb reactor inside of an argon-filled glove box. The reactor was heated to 350 °C for 24 h at a rate of 25 °C/h, then slowly cooled to 250 °C at 8 °C/h, maintained at 250 °C for 24 h, and then cooled to room temperature at 25 °C/h. The material was then hand ground with a mortar and pestle for 10 min and ball milled (8000M Spex Mixer Mill) using a mixture of 3 and 5 mm Y-ZrO$_2$ ball milling media in a 1:25

(solid electrolyte: media) mass ratio in a HDPE vial. Due to the sensitivity of Li_2OHCl to moist air, all processes were completed under argon.

Identification of the crystalline phase for Li_2OHCl was conducted on a PANalytical X'pert Pro Powder Diffractometer with CuK α radiation ($\lambda = 1.54056$ Å). Powder samples were dispersed on quartz slides and sealed with Kapton® films. High-temperature x-ray diffraction (XRD) scans were conducted with an Anton Paar XRK 900 Hot Stage which was heated to 200 °C at 2 °C/min; the temperature was maintained for 20 min prior to collecting crystallographic data. Rietveld refinements and analysis of crystallographic data were completed with HIGHSCORE PLUS, which is a software package provided through PANanalytical.

Slow-cooled Li_2OHCl was cold pressed at 300 MPa in an airtight cell designed by our group with Al/C blocking electrodes for all electrochemical impedance spectroscopy (EIS) measurements (Bio-Logic, VSP). EIS measurements were measured between 1 mHz and 1 MHz with an amplitude of 100.0 mV in a temperature-controlled chamber. For Arrhenius measurements, the temperature control chamber was ramped from 25 °C to 200 °C and allowed to equilibrate for 2 h before EIS measurements were collected.

III. CRYSTAL STRUCTURE

A. Low-temperature structures of Li$_2$OHCl

1. Static lattice simulations

By static lattice simulations we mean simulations performed by assuming that the atomic positions are time independent, with no effects of quantum lattice vibrations taken into account. These results are obtained by optimizing the total energy with respect to atomic positions and simulation cell parameters within self-consistent density functional calculations.

One goal of the simulations is to make accurate models of the available experimental results. Information about the low-temperature structure of Li_2OHCl from experimental evidence can be summarized as follows. Below temperatures of approximately 35 °C, Schwering *et al.* [4] reported the structure of Li_2OHCl to be orthorhombic. The analyzed lattice constants were given as $a = 3.8220(1)$ Å, $b = 7.9968(2)$ Å, and $c = 7.7394(2)$ Å, and the space group $Amm2$ (#38) [22] was suggested. While the fractional coordinates of the atoms were not reported, the experimental study of the phase transition indicated the low-temperature phase to be ordered. The x-ray diffraction pattern of samples of the low-temperature phase of "fast-cooled" samples were also recently reported by Hood *et al.* [1], and analogous results for "slow-cooled" samples are presented in this work.

From this evidence, we carried out a computational structure search to determine the ground-state structure of Li_2OHCl. Several candidate structures were optimized using the density functional theory methods described in Sec. II A. The candidate structures were based on ordered variations of the cubic structure found in the literature [3]. As a result of this computational search, we found the lowest-energy structure to have a tetragonal lattice characterized by the space group $P4mm$ (#99) as shown in Fig. 1(a). (For convenience
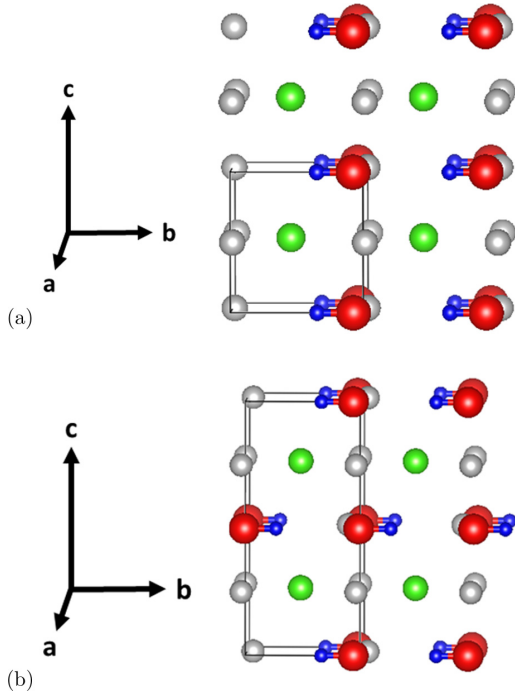
FIG. 1. Ball and stick representations of the computationally optimized structures of Li_2OHCl in the (a) tetragonal structure [space group $P4mm$ (#99), rotated by $90°$ about the a axis from the standard orientation] and (b) orthorhombic structure [space group $Pmc2_1$ (#26)]. For both structures, green balls represent Cl, red O, blue H, and silver Li.

in making structural comparisons, we rotated the standard lattice orientation by $90°$ about the a axis.) This ground-state structure has all of the OH groups oriented along the b axis and is very closely related to an ordered form of the high-temperature cubic structure which will be discussed in Sec. III B. The optimized lattice constants and fractional atomic coordinates are given in Table I.

The challenge introduced by this DFT ground-state structure is to reconcile the determined tetragonal structure with the experimental findings [1,4] of an orthorhombic structure. One variation of the ground-state structure that could give

TABLE I. DFT ground-state structure of Li_2OHCl having tetragonal structure with space group $P4mm$ (#99), using the nonstandard coordinates $x \to x$, $y \to z$, and $z \to -y$. The lattice constants (scaled by 1.02 to correct for the systematic LDA error) are $a = c = 3.794$ Å and $b = 3.578$ Å. The columns below list the atomic species, the multiplicity and Wyckoff label, and the fractional coordinates.

Atom	Wyckoff	x	y	z
O	$1a$	0.000	0.925	0.000
H	$1a$	0.000	0.654	0.000
Cl	$1b$	0.500	0.439	0.500
Li	$2c$	0.500	0.015	0.000

TABLE II. DFT metastable state structure of Li_2OHCl having orthorhombic structure with space group $Pmc2_1$ (#26). The lattice constants (scaled by 1.02 to correct for the systematic LDA error) are $a = 3.831$ Å, $b = 3.617$ Å, and $c = 7.985$ Å. The columns below list the atomic species, the multiplicity and Wyckoff label, and the fractional coordinates.

Atom	Wyckoff	x	y	z
O	$2a$	0.000	−0.024	0.000
H	$2a$	0.000	0.699	0.000
Cl	$2b$	0.500	0.500	0.250
Li	$2a$	0.000	0.001	0.250
Li	$2b$	0.500	0.086	0.000

rise to the orthorhombic structure is that the OH groups have a more complex orientational configuration compared with uniform alignment along the b axis. A structure search found a candidate orthorhombic structure having a DFT energy of 0.02 eV/FU (eV per formula unit) higher than the ground-state structure. Other distinct candidate orthorhombic structures were less stable by at least 0.1 eV/FU. This orthorhombic structure was found by optimizing the structure obtained by doubling the c axis of the tetragonal unit cell and coordinating the OH groups in opposite directions along the b axis. This structure has the space-group symmetry $Pmc2_1$ (#26). A visualization of this structure is shown in Fig. 1(b) and the lattice coordinates and fractional coordinates are given in Table II.

Although this candidate structure can explain the experimental observation of an orthorhombic unit cell, the computed lattice constants of $a = 3.831$ Å, $b = 3.617$ Å, and $c = 7.985$ Å (scaled by 1.02 to account for the systematic LDA error) are not in good agreement with the x-ray results measured in this work for the slow-cooled samples, nor the results reported by Schwering *et al.* [4], which correspond to $a = 3.8697$ Å, $b = 3.8220$ Å, and $c = 7.9968$ Å, presumably measured at room temperature. (Note that we assume that the mapping of the lattice convention used by Schwering *et al.* [4] to our convention corresponds to $a \to b$, $b \to c$, and $c/2 \to a$). Specifically, a significant discrepancy (of 5%) occurs for the optimized b-axis lattice constant. Similar difficulties in computing lattice constants associated with OH bonds using DFT-LDA for structural relaxation have been reported in the literature [23]. These observations motivated an extension of our simulations beyond the static lattice treatment.

2. Quasiharmonic simulations

The static lattice simulations described above are based on a purely classical treatment of the atomic nuclear positions. More realistically, the quantum mechanical physics of lattice vibrations can have significant effects on the structural properties of materials [24]. Within the context of a canonical ensemble, the appropriate thermodynamic energy is the Helmholtz free energy $F(T,a,b,c)$ as a function of temperature T and volume, which depends on the lattice parameters a, b, and c. (Note that in the present case, the experimental evidence suggests that it is sufficient to restrict consideration to orthorhombic structures, but in principle the

analysis could be extended to consider variations in the lattice angles α, β, and γ as well.) It is important to note that it is the Helmholtz free energy that is appropriate for this analysis (instead of the Gibbs free energy) because PV is small ($\sim 10^{-5}$ eV) at atmospheric pressures for these systems.

Within the Born-Oppenheimer approximation [25], the static lattice simulations well approximate the internal energy of the system due to the static nuclei and the corresponding total electronic energy $U_{\text{SL}}(a,b,c)$ for each set of lattice parameters a, b, and c. In principle, for each set of lattice parameters a, b, and c, the static lattice internal energy of a system can have a temperature dependence through its electronic degrees of freedom. However, for an ordered and electronically insulating material, it is reasonable to assume that the static lattice Helmholtz free energy is approximately temperature independent and dominated by the internal energy so that

$$F_{\text{SL}}(T,a,b,c) \approx U_{\text{SL}}(a,b,c). \tag{1}$$

Also within the framework of the Born-Oppenheimer approximation, the contributions of the lattice vibrations are energetically additive so that a reasonable approximation to the Helmholtz free energy can be determined from

$$F_{\text{QH}}(T,a,b,c) = U_{\text{SL}}(a,b,c) + F_{\text{vib}}(T,a,b,c), \tag{2}$$

where the subscript QH indicates the quasiharmonic approximation [21,26,27] and the vibrational Helmholtz free energy $F_{\text{vib}}(T,a,b,c)$ is evaluated at fixed lattice constants a,b,c using the harmonic approximation. Since we are examining ordered structures, it is not necessary to include effects of configurational entropy.

The quasiharmonic approximation [26] is based on the idea of calculating the vibrational Helmholtz free energy $F_{\text{vib}}(T,a,b,c)$ on a grid of lattice constants. For each set of lattice constants, the harmonic phonon spectrum is determined in terms of the phonon density of states $g(\omega,a,b,c)$:

$$g(\omega,a,b,c) = \frac{V}{(2\pi)^3} \int d^3q \sum_{\nu=1}^{3N} \delta(\omega - \omega_\nu(\mathbf{q},a,b,c)). \tag{3}$$

Here, V denotes the volume of the unit cell which contains N atoms. The integral over the phonon wave vectors $\mathbf{q}$ is taken over the Brillouin zone. For each $\mathbf{q}$, there are $3N$ normal mode frequencies ω_ν which contribute to the phonon density of states. These normal mode frequencies are determined from the eigenvalues of the dynamical matrix determined from the harmonic perturbations of the atomic positions $\tau_i(\mathbf{R}) = \tau_i^0 + \mathbf{R} + \mathbf{u}_i(\mathbf{R})$ for each atom i in each unit cell translated from the central cell by lattice translation $\mathbf{R}$. Here, τ_i^0 denotes the equilibrium position of the ith atom relative to the origin of the unit cell and $\mathbf{u}_i(\mathbf{R})$ denotes its harmonic displacement in cell $\mathbf{R}$.

Examples of the calculated phonon densities of states for two different sets of lattice constants a, b, and c are given in Fig. 2. The two sets of lattice constants were chosen as those that optimize the Helmholtz free energy at the temperature $T = 61$ and 301 K as will be explained later.
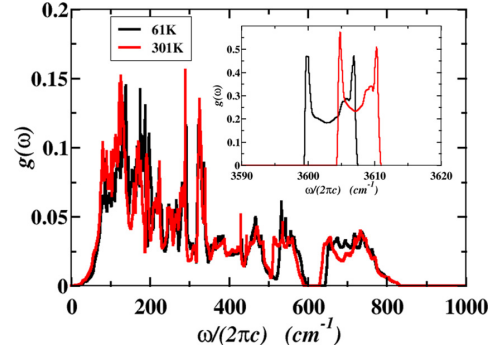

FIG. 2. Plots of $g(\omega,a,b,c)$ for two different sets of lattice parameters for the orthorhombic phase of Li$_2$OHCl. The sets of lattice parameters chosen for these plots correspond to optimal parameters found in this work. The inset shows the contributions to $g(\omega,a,b,c)$ from the high-frequency contributions on an expanded scale, corresponding to the stretching of the OH bonds.

For each set of lattice constants, a, b, and c, the static lattice internal energy corresponds to

$$U_{\text{SL}}(a,b,c) \equiv U_{\text{SL}}\big(a,b,c,\{\tau_i^0\}\big). \tag{4}$$

The Hessian matrix of the static lattice internal energy corresponds to the "analytic" part of the dynamical matrix expressed in terms of atoms i and j (with masses M_i and M_j) in the unit cell and displacement directions α and β [20,24]:

$$\tilde{D}_{i\alpha,j\beta}^{an}(\mathbf{q},a,b,c) = \frac{1}{\sqrt{M_i M_j}} \sum_{\mathbf{R}} e^{i\mathbf{q}\cdot\mathbf{R}} \frac{\partial^2 U_{\text{SL}}\big(a,b,c,\{\tau_i^0\}\big)}{\partial u_{i\alpha}(\mathbf{0})\partial u_{j\beta}(\mathbf{R})}. \tag{5}$$

Here, the summation over $\mathbf{R}$ represents the summation over all lattice translations. The evaluation of the Hessian includes both contributions from valence electron response and from the ions (nuclei and frozen core electrons) of the system evaluated within the QUANTUM ESPRESSO code [10]. For a phonon mode having wave vector $\mathbf{q}$, it can be assumed that the displacement can be expressed in terms of a complex amplitude vector according to

$$\mathbf{u}_i(\mathbf{R}) = \tilde{\mathbf{u}}_i(\mathbf{q})e^{i\mathbf{q}\cdot\mathbf{R}}. \tag{6}$$

In terms of these amplitudes, the valence electron response contributions are evaluated using density functional perturbation theory [19–21]. In ionic materials, such as in this study, the full dynamical matrix $\tilde{D}_{i\alpha,j\beta}(\mathbf{q},a,b,c)$ has an additional "nonanalytic" term representing coupling of the phonon modes near $\mathbf{q} \approx 0$ with an electromagnetic field [20,21], which is also evaluated in the QUANTUM ESPRESSO code [10]. Once the dynamical matrix is evaluated for each set of lattice parameters, it can be diagonalized to find the normal mode frequencies $\omega_\nu(\mathbf{q},a,b,c)$ and their corresponding amplitudes $A_{i\alpha}^\nu(\mathbf{q},a,b,c)$:

$$\sum_{j\beta} \tilde{D}_{i\alpha,j\beta}(\mathbf{q})A_{j\beta}^\nu(\mathbf{q},a,b,c) = \omega_\nu^2(\mathbf{q},a,b,c)A_{i\alpha}^\nu(\mathbf{q},a,b,c). \tag{7}$$

From the phonon density of states, the vibrational Helmholtz free energy is given by [24]

$$F_{\text{vib}}(T,a,b,c) = k_B T \int_0^\infty \ln\left[2\sinh\left(\frac{\hbar\omega}{2k_B T}\right)\right]$$
$$\times\, g(\omega,a,b,c)\, d\omega, \qquad (8)$$

where k_B denotes the Boltzmann constant. In order to analyze the various contributions, the corresponding vibrational internal energy is given by

$$U_{\text{vib}}(T,a,b,c) = \frac{\hbar}{2}\int_0^\infty \omega\coth\left(\frac{\hbar\omega}{2k_B T}\right) g(\omega,a,b,c)\, d\omega, \qquad (9)$$

and the vibrational entropy can be determined from

$$S_{\text{vib}}(T,a,b,c) = \frac{U_{\text{vib}}(T,a,b,c) - F_{\text{vib}}(T,a,b,c)}{T}. \qquad (10)$$

At each temperature T it is possible to minimize the Helmholtz free energy to determine the optimal lattice parameters $a(T)$, $b(T)$, and $c(T)$ for each structure

$$F_{\text{min}}(T) = \min_{(a,b,c)} F_{\text{QH}}(T,a,b,c), \qquad (11)$$

by interpolating the values of $F_{\text{QH}}(T,a,b,c)$ evaluated on the lattice constant grid.

In practice, for each system, the grid of lattice constants must be chosen to contain the minimum of the free energy. For analyzing the tetragonal structure of Li_2OHCl, a $4 \times 4 \times 4$ grid was chosen with a uniform grid spacing of approximately 0.095 Å. The range of lattice constants in Å units was $3.720 \leqslant a$ or $c \leqslant 4.006$, and $3.508 \leqslant b \leqslant 3.794$. For the orthorhombic structure of Li_2OHCl, a $5 \times 6 \times 5$ grid was chosen with a uniform grid spacing of approximately 0.073 Å. For this case, the range of lattice constants in Å units was $3.659 \leqslant a \leqslant 3.952$, $3.466 \leqslant b \leqslant 3.833$, and $7.725 \leqslant c \leqslant 8.017$. For each grid point of the lattice constants, the static lattice internal energy $U_{\text{SL}}(a,b,c)$ was determined by optimizing the internal atomic coordinates within the self-consistent density functional formalism. In order to ensure that the optimized structure corresponded to an equilibrium configuration, it was helpful to repeat the optimization with initial atomic coordinates differing slightly from the configurations shown in Fig. 1 with the use of random noise. It was found that for the orthorhombic structure, stable structures could be obtained by adding the noise only along the b axis. With this added precaution, it was possible to perform the harmonic phonon calculations at each grid point of the lattice constants without finding any imaginary (unstable) vibrational modes, indicating the validity of the quasiharmonic approximation for these systems and thus determining the phonon density of states $g(\omega,a,b,c)$.

The results of these calculations proved to be interesting in several aspects. First, in analyzing the optimized Helmholtz free energies per formula unit for the tetragonal phase and orthorhombic phase shown in Fig. 3, it is shown that the tetragonal phase is predicted to be thermodynamically favorable relative to the orthorhombic phase in the temperature range from 0 to 425 K. It is important to note the sensitivity to the crossing point of the free energies in Fig. 3 to a small
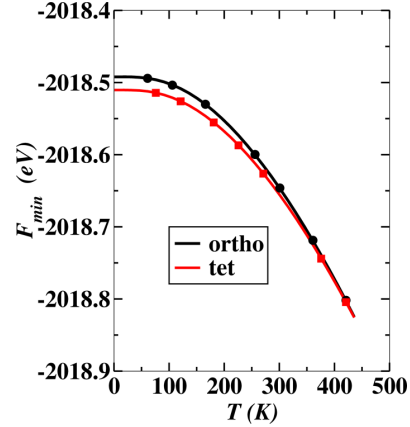

FIG. 3. Optimized Helmholtz free energy F_{min} (eV/FU) as a function of temperature T (K) computed for the tetragonal (red line) and orthorhombic (black line) structures of Li_2OHCl. The solid lines were determined by interpolation of the grid values, while the symbols represent values of $F_{\text{min}}(T)$ recalculated at the minimum lattice constants for the given temperature. The zero of energy (specifically for U_{SL}) is arbitrary but consistent throughout this paper.

error in the calculation. A relative error of ± 0.01 eV shifts the crossing point of the relative free energies by $\sim\pm 100$ K. While there is a large error bar on the transition temperature, the simulations suggest that the tetragonal phase should be thermodynamically stable at low temperatures. In fact, to the best of our knowledge, the tetragonal phase has not been reported in the experimental literature nor in the experimental x-ray analyses of this work. Since the tetragonal structure requires all of the OH groups to be aligned in the same direction, perhaps there are kinetic reasons which disfavor the tetragonal structure.

It is also interesting to look at the temperature dependence of the optimized lattice parameters $a(T)$, $b(T)$, and $c(T)$ for the tetragonal and orthorhombic phases as shown in Fig. 4. The lattice parameters for the tetragonal phase are continuous, and show a gentle increase in the lattice parameters across the temperature range. The lattice parameters for the orthorhombic phase are also continuous with a more rapid increase in $b(T)$ and smaller rapid decrease in $a(T)$ at T 150 K. Table III lists some typical values of the low-temperature and room-temperature optimized lattice parameters for both the tetragonal and orthorhombic phases. Comparing the low-temperature results computed within the quasiharmonic approximation with the corresponding static lattice results, we see that effects of lattice vibrations are to generally increase the lattice constants with largest increase occurring along the b axis which is the axis along which the OH bonds are aligned in these structures. The simulated lattice constants for the orthorhombic structure at room temperature in the quasiharmonic approximation are closer to the experimental results compared with the static lattice simulations.

To compare the theoretical x-ray diffraction with experiment, the atomic coordinates of orthorhombic structure were relaxed at the predicted room-temperature lattice constants; these atomic coordinates were used in a simulation cell with
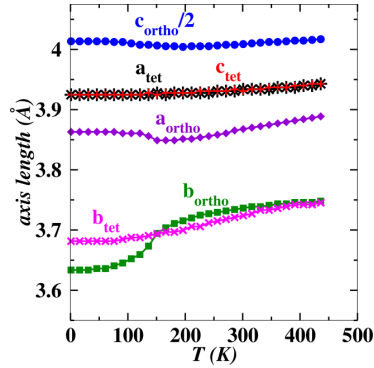
FIG. 4. Comparison of each of the lattice parameters as a function of temperature, calculated by optimizing $F_{min}(T)$ at each temperature and by multiplying by 1.02 to account for the systematic LDA error, comparing both the theoretical tetragonal and orthorhombic structures.

the theoretical corrected lattice parameters from Table III to produce theoretical x-ray diffraction patterns to compare with experiment. A comparison is shown in Fig. 5 with the orthorhombic structure before the quasiharmonic corrections, the room-temperature x-ray diffraction for the theoretical quasiharmonic corrected coordinates and lattice parameters from Table III, theoretical coordinates with experimental lattice parameters from Table III, and the experimental x-ray diffraction in this work. It is apparent that the x-ray diffraction for the theoretical atomic coordinates with experimental lattice parameters from this work is in good agreement with the experimental diffraction peaks measured in this work, while the purely theoretical quasiharmonic peaks are in reasonable agreement. It is noted that the quasiharmonic correction does improve the comparison with experiment. Its biggest effect is to increase the b lattice parameter by 0.1 Å relative to the static lattice value, while the experimental

TABLE III. Summary of low-temperature and room-temperature lattice parameters (in Å units) for Li$_2$OHCl calculated from the quasiharmonic approach defined in Eq. (11), scaled by a factor of 1.02 to account for the systematic LDA error. Results for both the tetragonal (tet) and orthorhombic (ortho) phases are tabulated at low temperature and at room temperature and compared with static lattice (SL) results. The simulation results are compared with experiment.

	a (Å)	b (Å)	c (Å)
tet SL	3.79	3.58	3.79
tet at $T = 106$ K	3.92	3.69	3.92
tet at $T = 271$ K	3.93	3.71	3.93
ortho SL	3.83	3.62	7.98
ortho at $T = 106$ K	3.86	3.65	8.02
ortho at $T = 271$ K	3.86	3.73	8.02
Experiment[a]	3.8697(1)	3.8220(1)	7.9968(2)
Experiment[b]	3.8749(8)	3.8257(8)	7.999(1)

[a]From Schwering in Ref. [4], mapping the reported values for the $c/2$, a, and b axes into the a, b, and c axes of this work.
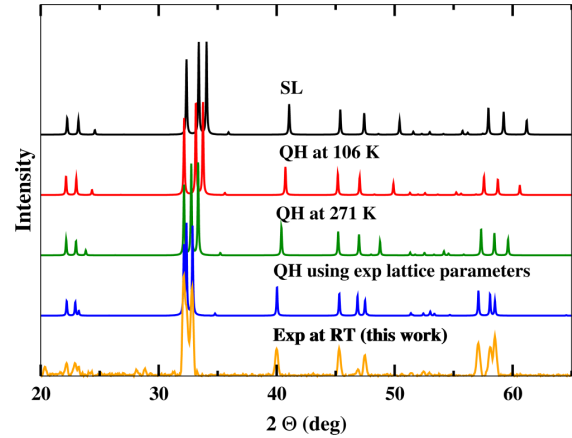[b]Measured in this work at $T = 294.25$ K.

FIG. 5. Comparison of simulated and experimental x-ray diffraction ($\lambda = 1.54056$ Å) patterns for the orthorhombic structure of Li$_2$OHCl. Black (top) shows the simulated result corresponding to the static lattice approximation. Red and green curves (upper middle) show the simulated result corresponding to the quasiharmonic approximation at 106 and 271 K, respectively. Blue curve (lower middle) was derived using the lattice parameters measured in this work and the fractional coordinates of the quasiharmonic simulations at 271 K. Orange (bottom) curve represents experimental measurements in this work.

b-axis lattice parameter is 0.2 Å larger than the static lattice value. The corresponding computed fractional coordinates for the orthorhombic structure were found to be insensitive to experiment, with the largest change occurring for the H site and for one of the Li sites which vary by approximately 0.01 fractional units along the b axis between $T = 106$ and 271 K.

In order to get more information about these results, it is helpful to look at separate contributions to the free energy. Figure 6 shows the static lattice internal energy $U_{SL}(a(T),b(T),c(T))$, the vibrational internal energy in the quasiharmonic approximation [according to Eq. (9)] $U_{vib}(T,a(T),b(T),c(T))$, and the vibrational entropy in the quasiharmonic approximation [according to Eq. (10)] $S_{vib}(T,a(T),b(T),c(T))$ [as represented by $-T S_{vib}(T,a(T),b(T),c(T))$, in parts (a), (b), and (c), respectively]. In comparing the internal energies U_{SL} and U_{vib} for the tetragonal and orthorhombic structures as a function of temperature, it is seen that both of these increase with increasing T. The static lattice internal energy $U_{SL}(a(T),b(T),c(T))$ differs for the two structures by 0.02 eV or more throughout the temperature range. The vibrational internal energy $U_{vib}(T,a(T),b(T),c(T))$ for the tetragonal structure is slightly larger than that of the orthorhombic structure by 0.005 eV or less throughout the temperature range. The difference in the vibrational entropies $S_{vib}(T,a(T),b(T),c(T))$ for the two structures becomes larger at higher temperatures, with the orthorhombic structure having higher entropy. The orthorhombic structure has a steeper rise in its static lattice internal energy but at higher temperatures, the larger entropy means that eventually the $-T S$ contribution of the phonon free energy lowers the total free energy of the orthorhombic structure below that of the tetragonal structure.
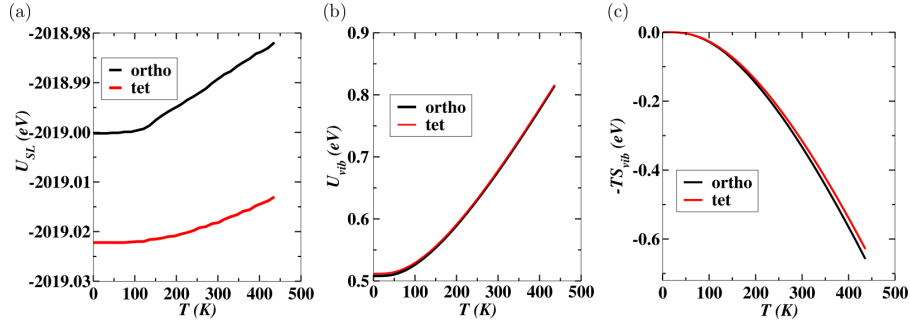
FIG. 6. Plots of thermodynamic quantities for the theoretical tetragonal and orthorhombic structures. Black is orthorhombic and red is tetragonal for all plots. Part (a) shows $U_{SL}(a(T),b(T),c(T))$ determined from the static lattice DFT total energies at the optimized lattice constants for temperature T. The zero of energy for U_{SL} is arbitrary, but consistent throughout this paper. (b) Shows the vibrational internal energy $U_{vib}(T,a(T),b(T),c(T))$. (c) Shows the vibrational entropy contribution in terms of $-T\,S_{vib}(T,a(T),b(T),c(T))$.

For example, our calculations find that at $T = 300$ K, $-T[S_{vib}(\text{ortho}) - S_{vib}(\text{tet})] = -0.02$ eV. The increase in entropy for the orthorhombic structure can be attributed to a shift in the phonon density of states to lower frequencies in the frequency range of $0 \leqslant \omega/(2\pi c) \leqslant 1000$ cm^{-1} as shown in Fig. 2.

Having found a reasonable model for the orthorhombic phase of Li$_2$OHCl, it is useful to focus on some of the details of the computational results for that system. One interesting feature of the computed orthorhombic phase is a predicted abrupt but continuous change of the b-axis parameter near $T = 150$ K as shown in Fig. 4. To investigate this further, contour plots of the free energy $F_{QH}(T,a,b,c)$, with the c axis

fixed at the predicted value for that temperature and in the entire plane of the interpolated results for the a and b axes, are presented in Fig. 7. The results show that going from low to high temperature, there is an expansion/elongation of the free energy minimum at the transition followed by a recentering and steepening of the minimum.

B. High-temperature structures of Li$_2$OHCl

The phase transition of Li$_2$OHCl has been observed [4] at temperatures above 35 °C, changing between the orthorhombic structure to cubic structure with heating. Hysteresis has been observed during the heating and cooling cycles. Evidence from
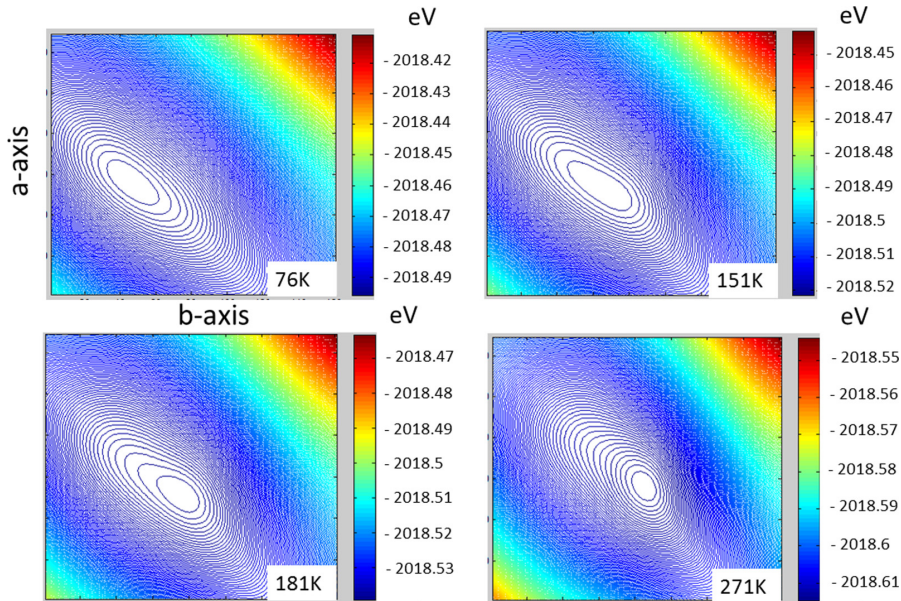
FIG. 7. Contour plots of the computed Helmholtz free energy $F(T,a,b,c(T))$ of the orthorhombic structure for four representative temperatures T. For each T, the plot spans the full grid of points in the a-b plane at the optimized value of $c(T)$. The vertical axis corresponds to the a axis which spans the range $3.659 \leqslant a \leqslant 3.952$ Å, the horizontal to the b axis which spans the range between $3.466 \leqslant b \leqslant 3.833$ Å.

TABLE IV. Fractional coordinates and site occupancies for the cubic $Pm\bar{3}m$ (#221) structure of Li_2OHCl. The columns below list the atomic species, the multiplicity and Wyckoff label, the fractional coordinates, and their occupancy factors as determined by Ref. [3]. The H coordinates were not determined.

Atom	Wyckoff	x	y	z	occ.
O	$1a$	0	0	0	1
Cl	$1b$	$\frac{1}{2}$	$\frac{1}{2}$	$\frac{1}{2}$	1
Li	$3d$	$\frac{1}{2}$	0	0	$\frac{2}{3}$

nuclear magnetic resonance (NMR) analysis [4] is consistent with the cubic structure being disordered as is consistent with the structure of the deuterated material, Li_2ODCl, which was analyzed by Eilbracht *et al.* [3] to have the space group $Pm\bar{3}m$ (#221). The corresponding atomic positions and their fractional occupancies are listed in Table IV. The lattice parameter of cubic Li_2OHCl was reported by Schwering *et al.* [4] to be $a = 3.9103(1)$ Å. A visualization of the unit cell indicating the fractional occupancy is shown in Fig. 8(a), while a model structure based on an optimized $5 \times 5 \times 5$ supercell is shown in Fig. 8(b).

In order to better understand the disordered system, several models were investigated. Supercells were prepared with lithium, oxygen, and chlorine at their ideal positions from Table IV, choosing two-thirds occupation of the lithium sites at random. The hydrogen sites were placed randomly on 4π

(a)

(b)

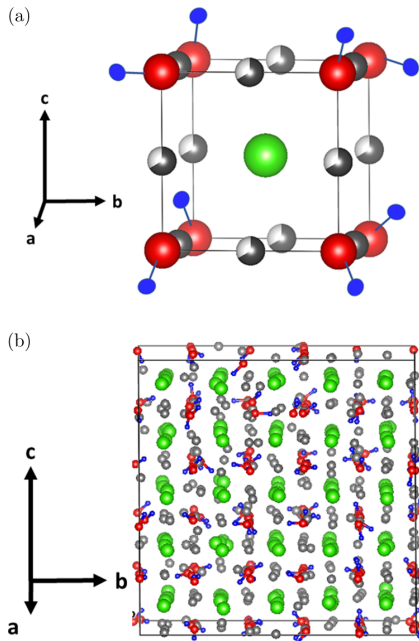FIG. 8. (a) Shows a possible structure for a unit cell of cubic Li_2OHCl with shaded white and gray balls indicating the partially occupied Li sites. (b) Shows an optimized structure for a $5 \times 5 \times 5$ supercell of the disorder structure. The Li, O, H, and Cl sites are indicated with silver, red, blue, and green balls, respectively.

solid angles corresponding to the surfaces of spheres about each oxygen site having radii equal to 1 Å, representing the bond length of OH. These supercells were initialized at the cubic lattice parameters reported by Schwering *et al.* [4] and then all cell dimensions and atomic positions allowed to relax. This was done for 20 examples of $2 \times 2 \times 2$, 10 examples of $3 \times 3 \times 3$, 3 examples of $4 \times 4 \times 4$, and 2 examples of $5 \times 5 \times 5$ supercells. A visualization of one of the relaxed $5 \times 5 \times 5$ supercells is shown in Fig. 8(b). All of the relaxed configurations show deviation from cubic symmetry; one expects that a typical small piece of disordered material will produce a noncubic strain. In the limit of large bulk these strains should average out giving the cubic structure. The average of the axis lengths and axis angles for the progressively larger supercells is shown in Figs. 9(a) and 9(b), respectively, with error bars indicating the standard deviation (as distinct from the standard deviation of the mean). The results show that the standard deviation of the results gets smaller as the cell size increases; this is is indicative of the disordered model going to cubic in the large supercell limit. The average of the axes for the $5 \times 5 \times 5$ supercell is taken as the estimate for the theoretical disordered cubic lattice parameter, which is 3.87 Å compared to the 3.91 Å reported by Schwering *et al.* [4].

As a further check on the simulated structure, the diffraction pattern for the the $5 \times 5 \times 5$ optimized supercell model shown Fig. 8(b) is compared with simulated x-ray pattern generated using the lattice parameters given by Schwering *et al.* [4] and with the experimental x-ray pattern measured in this work. Note that the lattice constant measured in this work is $a = 3.9083(1)$ Å at $T = 323.15$ K and $a = 3.9345(1)$ Å at $T = 473.15$ K which compares well with the value $a = 3.9103(1)$ Å reported by Schwering *et al.* [4]. The results are presented in Fig. 10. The agreement between the diffraction patterns is very good and shows that even with the large atomic relaxations relative to the ideal structure, the diffraction peaks are very sharp. In this case, the mobile species, Li^+ ions and H associated with OH groups, slightly perturb the less mobile diffracting species and have themselves very small diffraction cross sections.

IV. IONIC CONDUCTIVITY AND MOLECULAR DYNAMICS SIMULATIONS

The ionic conductivity versus temperature behavior of samples of Li_2OHCl for "slow-cooled" samples prepared in this study are presented as the red circles shown in Fig. 11. The results are similar to those presented in Ref. [1] for fast-cooled samples. The jump by more than a factor of 10 in the conductivity for temperatures near $T \approx 310$ K corresponds to the orthorhombic $\leftrightarrow$ cubic structural change. A similar but larger conductivity jump for samples of Li_2OHCl was reported by Schwering *et al.* [4].

Molecular dynamics simulations were carried out to better understand both the lithium ion diffusion and conductivity and the structural properties of the cubic phase of Li_2OHCl. The simulations were carried out for two unique starting configurations constructed as described in Sec. III B for $3 \times 3 \times 3$ supercells. For these simulations, the cubic lattice parameters were taken from the experimental parameters [4], reduced
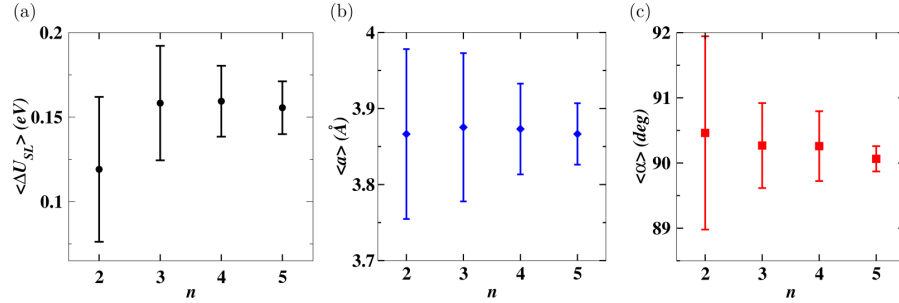
FIG. 9. Summary of results for optimized models of Li_2OHCl in its disordered cubic structures plotted as a function of n used to construct $n \times n \times n$ supercells in each case. The average value is indicated with a filled symbol and the error bars in the plots indicate the standard deviation. (a) $\langle \Delta U_{SL} \rangle$ denotes the average static lattice internal energy per cubic unit cell of the model configuration relative to the corresponding internal energy in the tetragonal phase. (b) $\langle a \rangle$ denotes the average cubic lattice parameter. (c) $\langle \alpha \rangle$ denotes the average lattice angle.

by 2% to approximate the LDA correction. The molecular dynamics simulations were carried out at constant volume in the manner described in the Methods section (Sec. II A) for the target temperatures in the range of $T = 300$–600 K which resulted in 14 molecular dynamics samples at computed temperatures in the range of $T = 350$–700 K. As discussed in further detail below, the simulations for one of the initial configurations configurations was carried out for approximately 120 ps, while the other configuration was carried out for approximately 60 ps. The similarity of analyzed results from the two initial configurations at equivalent temperatures suggest some degree of sampling convergence. Of course, it is always the case that the molecular dynamics results would benefit from longer simulation times. On the other hand, the analysis shows that during the simulation runs at even for the lowest-temperature simulations, 354 and 396 K, there are 5 and 17 hopping events, respectively. This indicates the presence of

low-energy activation barriers for hopping in this disordered system. These events were counted by assigning each Li to its nearest lattice site according to the simulation data of each run and then counting the number of discrete site transitions during the simulation.

Based on Kubo's analysis of the fluctuation-dissipation theorem in the context of evaluating transport properties of materials, the conductivity σ of a system is related to the averaged correlation function of current density $\mathbf{J}(t)$ of the system [28,29]

$$\sigma = \frac{V}{3k_B T} \int_0^\infty \langle \mathbf{J}(t) \cdot \mathbf{J}(0) \rangle dt. \tag{12}$$

In this expression, V represents the volume of the simulation cell, k_B is the Boltzmann constant, and T is the temperature. The angular brackets indicate ensemble averaging over initial configurations and the evaluation averages the diagonal of the conductivity tensor. For a system having ions of charge eQ_i
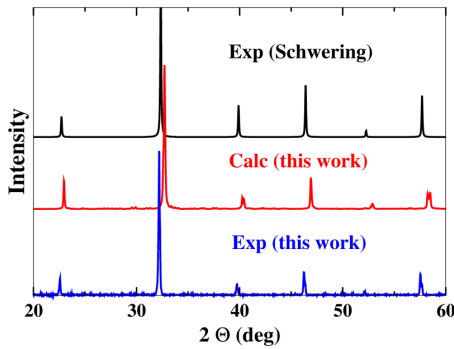
FIG. 10. X-ray diffraction ($\lambda = 1.54056$ Å) results of the cubic phase of Li_2OHCl, comparing simulated and measured intensities as a function of 2Θ (deg). The top plot was generated using the lattice parameters given by Schwering *et al.* [4] and fractional coordinates of the ideal disordered lattice. The second plot is the diffraction pattern generated from the $5 \times 5 \times 5$ optimized supercell model shown Fig. 8(b) and the bottom plot is an experimental x-ray pattern measured at $T = 323.15$ K for a slow-cooled sample synthesized in this work.
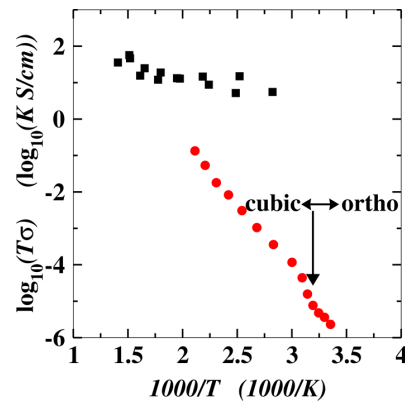
FIG. 11. Red circles correspond to the measured relationship between ionic conductivity σ (S/cm) and temperature T (in K) for slow-cooled samples of Li_2OHCl plotted as $\log_{10}(T\sigma)$ versus $1000/T$. The black squares correspond to the simulated conductivity inferred from tracer diffusion values according to Eq. (20) in terms of $\log_{10}(T\sigma H_r)$ versus $1000/T$.

and instantaneous particle velocities $\dot{\mathbf{R}}_i(t)$, the current density is given by

$$\mathbf{J}(t) = \frac{e}{V} \sum_{i=1}^{N} Q_i \dot{\mathbf{R}}_i(t), \tag{13}$$

where the summation over particles i includes all N ions in the simulation cell. By integrating Eq. (12) over time, the conductivity can be expressed in terms of the instantaneous particle positions $\mathbf{R}_i(t)$ in the form [29,30]

$$\sigma = \frac{e^2}{6V k_B T} \lim_{t \to \infty} \frac{1}{t} \langle |\mathbf{p}(t)|^2 \rangle, \tag{14}$$

where the charge moment vector is given by

$$\mathbf{p}(t) \equiv \sum_{i=1}^{N} Q_i [\mathbf{R}_i(t) - \mathbf{R}_i(0)]. \tag{15}$$

Here, the angular brackets indicate ensemble averaging over initial configurations. In practice, it is expected that only the motions of the Li ions (with charge eQ_{Li}) make significant contributions to the current density, while the current density contributions from the other ions of the system are expected to average to 0. Including only the Li ion contributions to the squared moment vector using Li ion labels ($i = 1, 2, \ldots, M$), we can approximate

$$|\mathbf{p}(t)|^2 \approx Q_{\mathrm{Li}}^2 [\Delta_{\mathrm{self}}(t) + \Delta_{\mathrm{cross}}(t)], \tag{16}$$

where

$$\Delta_{\mathrm{self}}(t) \equiv \sum_{i=1}^{M} |[\mathbf{R}_i(t) - \mathbf{R}_i(0)]|^2 \tag{17}$$

and

$$\Delta_{\mathrm{cross}}(t) \equiv \sum_{i=1}^{M} \sum_{j \neq i = 1}^{M} [\mathbf{R}_i(t) - \mathbf{R}_i(0)] \cdot [\mathbf{R}_j(t) - \mathbf{R}_j(0)]. \tag{18}$$

The independent ion contribution $\langle \Delta_{\mathrm{self}}(t) \rangle$ determines the tracer diffusion coefficient D^* according to [29]

$$D^* = \frac{1}{6M} \lim_{t \to \infty} \frac{1}{t} \langle \Delta_{\mathrm{self}}(t) \rangle. \tag{19}$$

In practice, D^* is estimated from linear fits of computed values of $\Delta_{\mathrm{self}}(t)$ or, equivalently, to the mean-squared displacements (MSD) in the molecular dynamics simulations. The tracer diffusion coefficient D^* can also be measured experimentally [31–33]. In order to relate the Li ion tracer diffusion to the Li ion conductivity, it is convenient to define [29]

$$\sigma = \frac{M}{V} \frac{e^2 Q_{\mathrm{Li}}^2 D^*}{k_B T H_r}. \tag{20}$$

Here, the Haven ratio (H_r) [31,34] is a measure of the correlation of the conducting ions which also measures the discrepancy between the measured ionic conductivity and the one that would be estimated from the tracer diffusion coefficient used in the Nernst-Einstein relation. If the long time limit of the ensemble average of the ion cross correlation term in the squared charge moment vector $\langle \Delta_{\mathrm{cross}}(t) \rangle$ is zero,

$H_r = 1$. The molecular dynamics runs in this study were analyzed for their tracer diffusion coefficients $D^*(T)$ and using Eq. (20) assuming $H_r = 1$. The results are plotted together with the experimental conductivity in terms of $\log_{10}(T\sigma)$ in Fig. 11. In evaluating Eq. (20), we have assumed that $Q_{\mathrm{Li}} = 1$ which is consistent with the calculated Born effective charge [20] on a Li site.

The comparison in Fig. 11 between the calculated results from calculated tracer diffusion coefficients and the experimental measurements of ionic conductivity suggest that this system has a very large value of the Haven ratio $H_r \gg 1$. As mentioned above, the molecular dynamics simulations may have some statistical errors, particularly at the lower temperatures. However, our analysis suggests that longer simulation times would not change the qualitative evidence for the large Haven ratio. The results also suggest that the Haven ratio is temperature dependent, varying between $H_r(T = 470 \text{ K}) \approx 1 \times 10^2$ and $H_r(T = 310 \text{ K}) \approx 2 \times 10^5$. According to the analysis derived from the Kubo formalism, we see that in order to achieve $H_r > 1$ the long time ensemble average of $\langle \Delta_{\mathrm{cross}}(t) \rangle$ must be less than zero, which can occur when correlated ions hop in opposite directions. Analyzing our molecular dynamics simulations at the lower-temperature runs, we see evidence of $\langle \Delta_{\mathrm{cross}}(t) \rangle < 0$, however, we do not have enough statistics within the current simulations to make a quantitative analysis of this term. It is documented [35] that while the independent ion contribution $\langle \Delta_{\mathrm{self}}(t) \rangle$ is accessible within molecular dynamics simulations, the ion pair correlation contribution $\langle \Delta_{\mathrm{cross}}(t) \rangle$ is very difficult to converge. Typically, Haven ratios for lattice systems are less than 1 [29]. A few recent reports of computed Haven ratios in other electrolytes find $H_r < 1$ [36,37]. On the other hand, there have been a few reports of large Haven ratios for proton diffusion [38] and for simulations of Ag migration in phases of AgI [39]. In both of these cases, correlated motions of the active ion could be proposed. In cubic Li_2OHCl, we expect that the Li ion motions are correlated through their interaction with the neighboring OH orientations. For example, we find that there seems to be a preference for the OH groups to be oriented toward the Li vacancy sites, as discussed further below.

The diffusion coefficient and conductivity are temperature dependent. It is often the case that the tracer diffusion coefficient has an Arrhenius form for the temperature dependence:

$$D^*(T) = D_0^* e^{-E_a/(k_B T)}, \tag{21}$$

where E_a measures the activation energy for the process. Fitting the simulated tracer diffusion results to Eq. (21), we estimate $E_a^{\mathrm{tracer}} = 0.12 \pm 0.02$ eV. Fitting the measured $\log(T\sigma)$ versus $1/T$ results in the temperature range 330–500 K, we estimate that the corresponding conductivity activation energy for the cubic phase is $E_a^{\sigma} = 0.70 \pm 0.02$ eV. A closer examination of the measured $\log(T\sigma)$ plots shows a small deviation from pure Arrhenius behavior similar to a system reported in the literature which was modeled as having a distribution of activation barriers due to configurational disorder [40]. For cubic Li_2OHCl, due to the disorder in Li ion sites and OH orientations, it seems reasonable that there would be a distribution of local activation barriers for site hopping. The large difference between the calculated E_a^{tracer} and E_a^{σ}
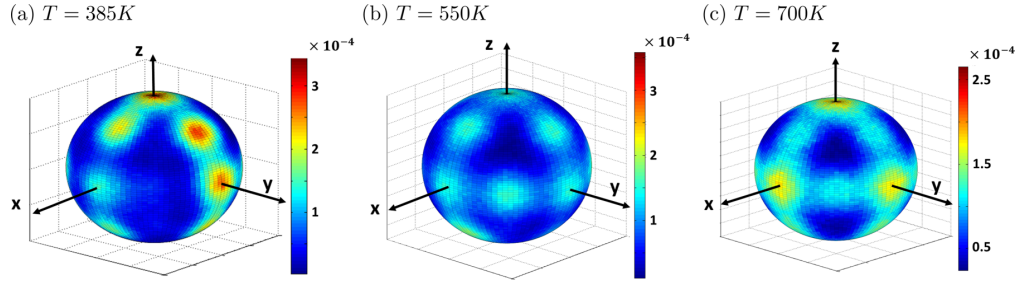
FIG. 12. Plots of the probability densities for OH angles $\mathcal{A}(\theta,\phi)$ at three representative temperatures evaluated from histograms of the molecular dynamics simulations.

implies that the mechanisms involved in the two processes are quite different, as is consistent with the notion that the Li ion motions are correlated during conductivity measurements.

One important characteristic of the cubic structure of Li_2OHCl compared with the orthorhombic phase is the variation in the OH bond directions. Our analysis of the quantum effects of H from the quasiharmonic treatment of lattice vibrations suggests that the rotations of OH bonds may have significant quantum contributions, which is beyond the purview of this study. However, the molecular dynamics simulations do provide a classical treatment of the OH orientations within the various ensembles studied as a function of temperature. For one of the prepared $3 \times 3 \times 3$ supercells of the cubic structure and a set of simulations at three representative temperatures, the atomic configurations at each time step were used to make histograms of the OH bond angles, $\mathcal{A}(\theta,\phi)$, in terms of θ, measured with respect to the lattice **c** axis, and ϕ, measured with respect to the lattice **a** axis. In order to interpret $\mathcal{A}(\theta,\phi)$ as a probability density of finding the OH bonds at each θ and ϕ orientation, it has been normalized over the unit sphere. In Fig. 12, plots of $\mathcal{A}(\theta,\phi)$ are presented, in terms of their projection onto the unit sphere, for simulations at $T = 385$, 550, and 700 K in Figs. 12(a), 12(b), and 12(c), respectively. In principle, these plots should exhibit the cubic symmetry of the system in the ergodic limit of the simulation. For the lowest-temperature simulation of $T = 385$ K, we expect the asymmetry shown in the plot is due to the fact that the system is moving more slowly and sampling fewer configurations. The results for $\mathcal{A}(\theta,\phi)$ evaluated at $T = 385$ and at 550 K suggest that OH bonds are equally likely to be oriented along the $\langle 100 \rangle$ and $\langle 110 \rangle$ directions. At the highest temperature analyzed, the probability density is more diffuse, but suggests that the OH bonds are likely to be concentrated within {110} planes; there is a minimum probability of the bond to oriented along the $\langle 111 \rangle$ directions.

Comparing the structural diagrams for the tetragonal and orthorhombic phases (Fig. 1) and the cubic phase (Fig. 8), it is apparent that the orientation of the OH bonds in Li_2OHCl affects the Li ion positions. One way to visualize the motion of the Li ions and the H orientations is to construct a time superposed structural diagram as shown in Fig. 13. These figures were constructed from a molecular dynamics simulation at $T = 640$ K by keeping the Cl and O sites at their initial positions while snapshots of the Li and H positions were superposed for time intervals of 15 fs during 3.5 ps. Figure 13

shows this time superposed diagram from two vantage points: the first in Fig. 13(a) shows the entire simulation cell, and the second in Fig. 13(b) shows the slice made by the black rectangular box in Fig. 13(a) turned about the a axis to face the viewer. In both Figs. 13(a) and 13(b), the black oval encloses a lithium hopping event. The hopping event observed is consistent with the direct site hopping mechanism that was proposed by Li, Zhou, *et al.* [2] in their study of similar systems. While in this time superposed diagram, the time sequence of motions is lost, the concentration of hydrogen positions (blue) near the sites corresponding to Li ion vacancies (represented by black boxes) shown in Fig. 13(b) suggests correlation between the two. The time sequence arrows in the diagram also lend further support to the notion that OH orientations act to "gate" the Li ion hops.

In order to get further insight into the Li ion dynamics in the cubic phase of Li_2OHCl, it is convenient to define a quantitative parameter to gain insight into the time dependence of the occupation of the available Li sites. In the structure section, it was shown how the Li site disorder implies the lithiums being randomly distributed in space across the available sites, giving a $\frac{2}{3}$ spatial average of the lithium site occupancy. For each site i, it is convenient to define an average occupancy parameter:

$$\langle S_i(t) \rangle_{\text{time}} \equiv \frac{1}{t} \int_0^t S_i(t') dt', \tag{22}$$

where

$$S_i(t) \equiv \begin{cases} 1 & \text{if site } i \text{ is occupied at time } t, \\ 0 & \text{if site } i \text{ is not occupied at time } t. \end{cases} \tag{23}$$

For this purpose, each Li was assigned to the closest lattice site. In time, as the Li ion hops between all sites with equal probability, we expect that the asymptotic value of the average occupancy parameter is

$$\lim_{t \to \infty} (\langle S_i(t) \rangle_{\text{time}}) = \frac{2}{3}. \tag{24}$$

In order to monitor the Li ion hopping as a function of time t, it is convenient to define the following ergodicity measure:

$$E_m(t) = \left\langle \left| \frac{2}{3} - \langle S_i(t) \rangle_{\text{time}} \right| \right\rangle_{\text{sites}}. \tag{25}$$

For our system, initialized with random occupation of the fractionally occupied Li sites, $E_m(t=0) = \frac{4}{9}$. As the sim-
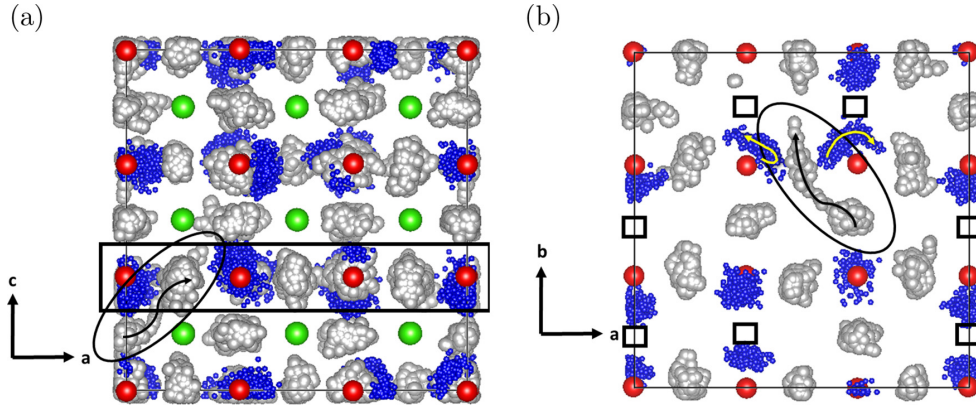
FIG. 13. Time superposed structural diagram of molecular dynamics simulation at $T = 640$ K using the same ball conventions as used in Fig. 8. Cl and O sites are represented at their initial positions and no OH bonds are drawn. Small black boxes indicate Li vacancy positions. Snapshots of the Li and H positions at 15-fs time intervals within the 3.5-ps simulations are superposed in the diagram. A black oval encloses Li site hops which have been completed during the simulation. The curved black arrows indicate the time sequence of the Li motion with the arrow tip corresponding to the latest time. The curved yellow arrows similarly indicate the time sequence of the H motions. (a) Shows the entire simulation cell projected on to the **a-c** plane. (b) Shows a slice of the simulation indicated by the black rectangle in (a), projected onto the **a-b** plane.

ulation proceeds with Li hopping events, we expect that $E_m(t)$ will decrease in time. Because of the asymptotic value of the average occupancy parameter noted in Eq. (24), the asymptotic value of the ergodicity measure must be $E_m(t \to \infty) = 0$. The behavior of $E_m(t)$ for the molecular dynamics simulations gives information about the Li ion hopping events and a measure of their ergodicity, as illustrated in Fig. 14 for the molecular dynamics simulations with two initial configurations. For our simulations, $E_m(t)$ does decrease with time, but within the simulation times of the current work, the asymptotic limit has not been reached even at the highest simulation temperatures. The values of $E_m(t)$ were averaged over initial times, so that the early times in the plot have better statistics. The results show that the higher-temperature simulations have increased ion hopping as expected, but the lower-temperature simulations need much longer times to achieve equivalent values of $E_m(t)$.

V. SUMMARY AND CONCLUSIONS

In this work, the structural and electrolyte properties of Li_2OHCl are examined. By comparing theoretical results to slow-cooled pristine samples of Li_2OHCl, a reasonable model of the low-temperature orthorhombic structure is found. The quasiharmonic approximation is found to improve the agreement of the simulations with experiment. A theoretical ground-state tetragonal structure is also found that has not been experimentally observed.

Structural calculations of the disordered cubic phase are in good agreement with experiment, particularly for large $(5 \times 5 \times 5)$ supercells. Moreover, the comparison of models of the ordered structures to the cubic structure can be described in terms of the availability of new sites for Li ion motion related to the OH bond directions. This is consistent to the abrupt change in ionic conductivity observed at the phase transition. Molecular dynamics simulations of tracer diffusion
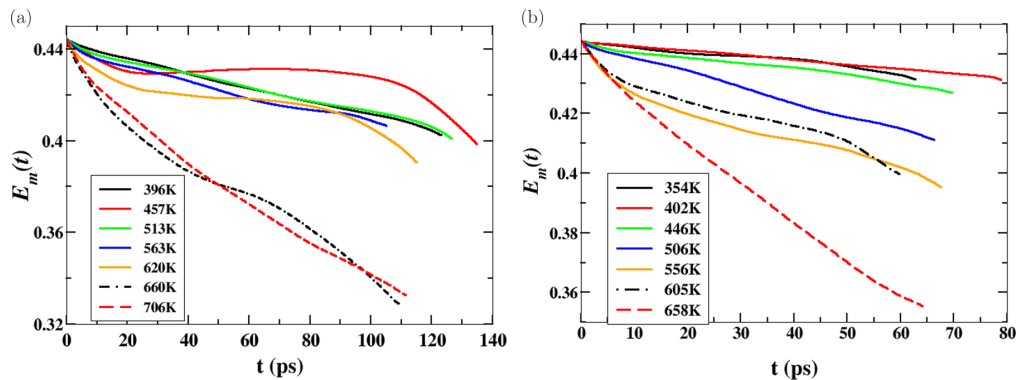

FIG. 14. (a), (b) Show plots of $E_m(t)$ as defined in Eq. (25) for two different initial configurations of cubic Li_2OHCl modeled in $3 \times 3 \times 3$ simulation cells. The legends list the average temperature of each simulation.

in the cubic phase are used to estimate ionic conductivity assuming no correlations among the mobile ion motions. The results show a large discrepancy with the experimental ionic conductivity measurement. The discrepancy gives evidence of a large temperature-dependent Haven ratio, indicating highly correlated Li ion motion. Molecular dynamics simulations also give evidence of a relationship between the OH orientations toward vacant Li sites. The OH bond orientations are suggested to participate in a gating mechanism for Li ion conduction. For analyzing the results, an ergodicity measure has been defined which goes to zero when all of the available Li sites have achieved their average occupation.

The combined experimental and computational study of well-formed Li_2OHCl structures should help inform the further development of this material as an electrolyte for all solid-state Li ion batteries as discussed in the recent literature [1,2].

[1] Z. D. Hood, H. Wang, A. Samuthira Pandian, J. K. Keum, and C. Liang, J. Am. Chem. Soc. **138**, 1768 (2016).

[2] Y. Li, W. Zhou, S. Xin, S. Li, J. Zhu, X. Lü, Z. Cui, Q. Jia, J. Zhou, Y. Zhao, and J. B. Goodenough, Angew. Chem., Int. Ed. **55**, 9965 (2016).

[3] C. Eilbracht, W. Kockelmann, D. Hohlwein, and H. Jacobs, Phys. B (Amsterdam) **234**, 48 (1997).

[4] G. Schwering, A. Hönnerscheid, L. van Wüllen, and M. Jansen, Chem. Phys. Chem. **4**, 343 (2003).

[5] P. Hartwig, A. Rabenau, and W. Weppner, J. Less-Common Met. **78**, 227 (1981).

[6] P. Hohenberg and W. Kohn, Phys. Rev. **136**, B864 (1964).

[7] W. Kohn and L. J. Sham, Phys. Rev. **140**, A1133 (1965).

[8] P. E. Blöchl, Phys. Rev. B **50**, 17953 (1994).

[9] N. A. W. Holzwarth, A. R. Tackett, and G. E. Matthews, Comput. Phys. Commun. **135**, 329 (2001), available from the website http://pwpaw.wfu.edu.

[10] P. Giannozzi, S. Baroni, N. Bonini, M. Calandra, R. Car, C. Cavazzoni, D. Ceresoli, G. L. Chiarotti, M. Cococcioni *et al.*, J. Phys.: Condens. Matter **21**, 395502 (2009), available from the website http://www.quantum-espresso.org.

[11] K. Momma and F. Izumi, Appl. Crystallogr. **44**, 1272 (2011), code available from the website http://jp-minerals.org/vesta/en/.

[12] A. Kokalj, J. Mol. Graphics Modell. **17**, 176 (1999), code available at the website http://www.xcrysden.org.

[13] H. T. Stokes and D. M. Hatch, J. Appl. Crystallogr. **38**, 237 (2008), available from the webpage http://iso.byu.edu/iso/isotropy.php.

[14] MATLAB, The MathWorks, Inc., Natick, Massachusetts, United States.

[15] J. P. Perdew and Y. Wang, Phys. Rev. B **45**, 13244 (1992).

[16] Y. A. Du and N. A. W. Holzwarth, Phys. Rev. B **76**, 174302 (2007).

[17] Y. A. Du and N. A. W. Holzwarth, Phys. Rev. B **81**, 184106 (2010).

[18] Z. D. Hood, C. Kates, M. Kirkham, S. Adhikari, C. Liang, and N. A. W. Holzwarth, Solid State Ionics **284**, 61 (2015).

[19] X. Gonze and J.-P. Vigneron, Phys. Rev. B **39**, 13120 (1989).

[20] P. Giannozzi, S. de Gironcoli, P. Pavone, and S. Baroni, Phys. Rev. B **43**, 7231 (1991).

[21] S. Baroni, S. de Gironcoli, A. Dal Corso, and P. Giannozzi, Rev. Mod. Phys. **73**, 515 (2001).

[22] *International Tables for Crystallography, Volume A: Space-Group Symmetry, Fifth Revised Edition*, edited by T. Hahn (Kluwer, Dordrecht, 2002). The symmetry labels used in this work are all based on this reference.

[23] K. Azuma, T. Oda, and S. Tanaka, Comput. Theor. Chem. **963**, 215 (2011).

[24] A. Maradudin, *Theory of Lattice Dynamics in the Harmonic Approximation, Second Edition*, Solid State Physics: Supplement, Vol. 3 (Academic, New York, 1971).

[25] M. Born and K. Huang, *Dynamical Theory of Crystal Lattices* (Oxford University Press, Oxford, 1954).

[26] S. Baroni, P. Giannozzi, and E. Isaev, Rev. Mineral. Geochem. **71**, 39 (2010).

[27] C. Lee and X. Gonze, Phys. Rev. B **51**, 8610 (1995).

[28] R. Kubo, J. Phys. Soc. Jpn. **12**, 570 (1957).

[29] G. Murch, Solid State Ionics **7**, 177 (1982).

[30] J. M. Haile, *Molecular Dynamics Simulation: Elementary Methods* (Wiley, New York, 1992).

[31] Y. Haven and B. Verkerk, Physics and Chemistry of Glasses **6**, 38 (1965).

[32] S. Takai, K. Yoshioka, H. Iikura, M. Matsubayashi, T. Yao, and T. Esaka, Solid State Ionics **256**, 93 (2014).

[33] N. Kuwata, X. Lu, T. Miyazaki, Y. Iwai, T. Tanabe, and J. Kawamura, Solid State Ionics **294**, 59 (2016).

[34] K. Campaan and Y. Haven, Trans. Faraday Soc. **54**, 1498 (1958).

[35] M. J. Castiglione and P. A. Madden, J. Phys.: Condens. Matter **13**, 9963 (2001).

[36] A. Marcolongo and N. Marzari, Phys. Rev. Mater. **1**, 025402 (2017).

[37] X. He, Y. Zhu, and Y. Mo, Nat. Commun. **8**, 15893 (2017).

[38] M. Spaeth, K. Kreuer, J. Maier, and C. Cramer, J. Solid State Chem. **148**, 169 (1999).

[39] B. J. Morgan and P. A. Madden, Phys. Rev. Lett. **112**, 145901 (2014).

[40] C. Bischoff, K. Schuller, S. P. Beckman, and S. W. Martin, Phys. Rev. Lett. **109**, 075901 (2012).

Appendix D

Kinetic Monte Carlo study of convergence properties of transport coefficients as guide to first principles molecular dynamics of Li_2OHCl

Analysis of the statistical and convergence properties of ionic transport coefficients with application to the solid electrolyte Li$_2$OHCl

Jason Howard[1] and N. A. W. Holzwarth[1, *]

[1]*Department of Physics, Wake Forest University, Winston-Salem, NC 27109-7507 USA*

(Dated: April 24, 2018)

The challenge of computing ionic transport coefficients from first principles is to achieve the necessary convergence with respect to system size, simulation time, and configurational sampling. Unfortunately current computer resources are not yet available for such convergence studies at the fully first principles level. In this work, a lattice kinetic Monte Carlo is used to study the convergence properties of transport coefficients, using the Li sub-lattice of the Li ion electrolyte Li$_2$OHCl as an example system. The specific transport coefficients representing tracer diffusion, effective diffusion, and mobility are carefully studied for their convergence properties. The ion pair correlations of the effective diffusion is also recast as a sum over events which allows for a detailed study of the nature of the correlation in terms of time and spatial separation which may be used to reduce the standard deviation. As an example, the analysis of the statistical properties of the tracer and effective diffusion are used to perform informed first principles simulations of Li$_2$OHCl. These simulations provide further evidence for anti-correlated Li-ion motion as predicted in a previous study.

I. INTRODUCTION

Renewed technological interest in discovering crystalline solid electrolytes,[1] has inspired the use of first principles computational methods for studying the properties of these materials, especially in simulating their ionic transport.[2,3] For ionic conductors whose conductivity mechanisms involve significant correlations among the mobile ions, it is computationally challenging to accurately simulate the transport properties. One such system that has received attention from several research efforts is Li$_2$OHCl and related compounds.[4–8] For this material in its disordered cubic phase, it has been suggested[7] that the mobile Li ions have correlated motion.

In fact, the notion of correlations affecting ionic conductivity is not new. Fifty years ago, the study of ionic conductivity for simple mechanisms and structures included corresponding estimates of correlation effects in terms of the Haven ratios.[9–12] More recently, the development of solid electrolyte materials for all-solid-state-battery technology has inspired new interest in accurate analysis and simulation of ionic conductivity with more complicated mechanisms and structures,[13,14] for which the estimate of the Haven ratio is much more challenging. In order to gain insight into the convergence issues associated with evaluating ionic conductivity, we have analyzed an efficient and simple model based on a lattice kinetic Monte Carlo approach.[15]

The remainder of the paper is organized as follows. The general formalism for evaluating ionic transport coefficients is reviewed in Sec. II. The details of the lattice kinetic Monte Carlo method are presented in Sec. III. The specific results of this work are based on the lattice structure appropriate to describing the disordered cubic phase of Li$_2$OHCl, but can be adapted to disordered lattice models more generally. Sec. IV presents the detailed results of statistical and convergence properties of the lattice kinetic Monte Carlo simulations of the ionic transport parameters. In Sec. V A the lattice kinetic Monte Carlo results are further analyzed in terms of temporal and spatial correlations. First principles simulations of this system are contrasted with the lattice kinetic Monte Carlo results in Sec. V B. Sec. VI contains the summary and conclusions.

II. FORMALISM

There are several alternative methods of simulating ionic conductivity in solids.[12] For example, Kubo[16] showed that the fluctuation-dissipation theorem can be used in the absence of an explicit electrical field to evaluate transport properties of materials. The diagonal components of the conductivity tensor, $\sigma_{\alpha\alpha}$, (where α denotes the cartesian components x, y, or z) is related to the time integral of the time auto correlation function of the current density $\mathbf{J}(t)$ vector components

$$\sigma_{\alpha\alpha}^{\text{Kubo}} = \frac{V}{k_B T} \int_0^\infty \langle J_\alpha(t_0 + \tau) J_\alpha(t_0) \rangle_{t_0} d\tau. \qquad (1)$$

In this expression, V represents the volume of the simulation cell, k_B is the Boltzmann constant, and T is the temperature. The $\langle \rangle_{t_0}$ brackets indicate ensemble averaging over initial configurations at time t_0 and the evaluation averages the $\alpha\alpha$ component of the conductivity tensor. For a system having ions of charge eQ_i and instantaneous particle velocities $\dot{\mathbf{R}}_i(t)$, the current density vector is given by

$$\mathbf{J}(t) = \frac{e}{V} \sum_{i=1}^{N} Q_i \dot{\mathbf{R}}_i(t), \qquad (2)$$

where, in principle, the summation over particles i should include all ions in the simulation cell. However, in the following we will assume that it is a reasonable approximation that only the mobile ions need be included. We

will further simplify the analysis to assume that there are N mobile ions within the simulation cell, each with the same charge $Q_i = Q$. With these approximations and by evaluating the time integral in Eq. (1), the diagonal conductivity tensor components can be expressed in terms of the instantaneous particle positions $\{\mathbf{R}_i(t)\}$ in the form[12,17]

$$\sigma_{\alpha\alpha}^{\text{Kubo}} = \frac{e^2}{2Vk_BT} \lim_{\tau \to \infty} \frac{1}{\tau} \langle p_\alpha(t_0, \tau) p_\alpha(t_0, \tau) \rangle_{t_0}, \quad (3)$$

expressed in terms of components of the charge moment vector which has the expression

$$\mathbf{p}(t_0, \tau) \equiv Q \sum_{i=1}^{N} (\delta \mathbf{R}_i(t_0, \tau)), \quad (4)$$

using the shorthand notation

$$\delta \mathbf{R}_i(t_0, \tau) \equiv \mathbf{R}_i(t_0 + \tau) - \mathbf{R}_i(t_0). \quad (5)$$

In this work, we focus our attention on the diagonal x-components of the conductivity tensor. It is convenient to evaluate the square of the x-component of the moment vector as a sum of two types of contributions.

$$(p_x(t_0, \tau))^2 = Q^2(\Delta_{\text{sf}}(t_0, \tau) + \Delta_{\text{cr}}(t_0, \tau)), \quad (6)$$

Here the first "self-interaction" term includes the sum of the squares of the x-components of the displacements of each of the individual ions:

$$\Delta_{\text{sf}}(t_0, \tau) \equiv \Delta_{\text{sf}}^x(t_0, \tau) \equiv \sum_{i=1}^{N} (\delta X_i(t_0, \tau))^2. \quad (7)$$

The second "cross-interaction" term includes the sum of products of x-component displacements of all pairs of ions:

$$\Delta_{\text{cr}}(t_0, \tau) \equiv \Delta_{\text{cr}}^x(t_0, \tau) \equiv \sum_{i(\neq j)=1}^{N} \sum_{j=1}^{N} (\delta X_i(t_0, \tau) \delta X_j(t_0, \tau)). \quad (8)$$

The configuration average of the independent ion contribution $\langle \Delta_{\text{sf}}(t) \rangle_{t_0}$ determines the tracer diffusion coefficient D^{tracer} according to[12]

$$D^{\text{tracer}} = \lim_{\tau \to \infty} D^{\text{tracer}}(\tau), \quad \text{where}$$
$$D^{\text{tracer}}(\tau) \equiv \frac{1}{2N} \frac{1}{\tau} \langle \Delta_{\text{sf}}(t_0, \tau) \rangle_{t_0}. \quad (9)$$

Analogously, we can define a "cross" diffusion coefficient according to

$$D^{\text{cross}} = \lim_{\tau \to \infty} D^{\text{cross}}(\tau), \quad \text{where}$$
$$D^{\text{cross}}(\tau) \equiv \frac{1}{2N} \frac{1}{\tau} \langle \Delta_{\text{cr}}(t_0, \tau) \rangle_{t_0}. \quad (10)$$

The configuration average of the sum of "self" and "cross" interaction terms determines the effective diffusion coefficient according to[12]

$$D^{\text{effective}} = \lim_{\tau \to \infty} D^{\text{effective}}(\tau) \quad \text{where}$$
$$D^{\text{effective}}(\tau) \equiv D^{\text{tracer}}(\tau) + D^{\text{cross}}(\tau) \quad (11)$$

The ratio of the tracer and effective diffusion coefficients is known as the Haven ratio (H_r)[9–11,18] which provides a measure of the correlation of the conducting ions in terms of

$$\frac{1}{H_r} \equiv \frac{D^{\text{effective}}}{D^{\text{tracer}}} = 1 + \lim_{\tau \to \infty} \frac{\langle \Delta_{\text{cr}}(t_0, \tau) \rangle_{t_0}}{\langle \Delta_{\text{sf}}(t_0, \tau) \rangle_{t_0}}. \quad (12)$$

The diffusion coefficients are related to diagonal components of the ionic conductivity tensor through the Nernst-Einstein relationship as well as following from the Kubo formalism of Eq. (1):

$$\sigma_{xx}^{\text{Kubo}} = \frac{N}{V} \frac{e^2 Q^2 D^{\text{effective}}}{k_BT} = \frac{N}{V} \frac{e^2 Q^2 D^{\text{tracer}}}{k_BT H_r}. \quad (13)$$

An alternative analysis of ionic conductivity follows from the inverse Ohm's law as the response of the time averaged current density in the α direction to an electric field F_α.

$$\langle J_\alpha(t) \rangle_t = \sigma_{\alpha\alpha}^{\text{Ohm}} F_\alpha. \quad (14)$$

Using Eq. (2) in the the presence of an electric field in the x-direction within the linear response regime, the Ohmic conductivity can be estimated from

$$\sigma_{xx}^{\text{Ohm}} = \frac{eQN}{V} \langle \mu_x(t_0) \rangle_{t_0}, \quad (15)$$

where the ion mobility for a given initial configurations $\{\mathbf{R}_i(t_0)\}$ is given by

$$\mu_x(t_0) \equiv \lim_{F_x \to 0} \left(\frac{1}{F_x} \lim_{\tau \to \infty} \left(\frac{1}{\tau} \left(\frac{1}{N} \sum_{i=1}^{N} \delta X_i^{F_x}(t_0, \tau) \right) \right) \right). \quad (16)$$

Here the F_x superscript on the ion displacement is used to indicate the field dependence of the trajectory for this case. The corresponding effective diffusion coefficient associated with the ion mobility can be defined by

$$D_\mu^{\text{effective}} = \frac{k_BT \langle \mu_x(t_0) \rangle_{t_0}}{eQ}. \quad (17)$$

In order to accurately simulate ionic conductivity for a system using Eqs. (13) or (15), several numerical and physical approximations must be made. At the present time, the "state of the art" for simulating ionic conductivity[3,7,8,13,14] uses first-principles methods to evaluate forces between ions. However, while the physics of the particle interactions is well represented, convergence of the results with respect to simulation size and time may not be as well under control. In this work we focus on these convergence issues for a simplified model of the ionic forces.

III. CALCULATIONAL DETAILS

In order to to efficiently evaluate the expressions discussed in Sec. II, we used a lattice based kinetic

Monte Carlo approach.[19–21] The N mobile ion positions $\{\mathbf{R}_i(t)\}$ are calculated within a supercell lattice having N_T available sites, each with an average occupancy of $o = N/N_T < 1$ and each with ν nearest neighbor sites, at a series of "times" t_s. Here, we enumerate the steps $s = 1, 2, ...S$ with fixed time intervals $\delta\tau$ according to

$$t_s = t_0 + s\delta\tau. \qquad (18)$$

Here, $\delta\tau$ is an arbitrary time increment which does not affect the simulation. It can be related to a physical time with additional model considerations. The Monte Carlo algorithm used in this work is as follows.

1. At the initial time t_0, the sites are occupied using a random number generator to produce $\{\mathbf{R}_i(t_0)\}$.

2. For subsequent time steps, $s \geq 1$, the following procedure updates the positions to $\{\mathbf{R}_i(t_s)\}$.

    (a) A random number generator chooses one of the occupied sites $1 \leq j \leq N$.

    (b) A random number generator chooses a nearest neighbor to $\mathbf{R}_j(t_{s-1})$ among the ν possible choices.

    (c) If the chosen nearest neighbor is unoccupied, then site $\mathbf{R}_j(t_{s-1})$ is moved to that site to form a new position $\mathbf{R}_j(t_s)$ and the configuration is updated accordingly to form $\{\mathbf{R}_i(t_s)\}$.

    (d) Otherwise the configuration $\{\mathbf{R}_i(t_s)\}$ remains the same as for the previous time step.

Some practical details are noted as follows.

3. The algorithm can be modified on Step #2(c) by introducing an activation energy E_A so that for a system temperature of T, the update of $\mathbf{R}_j(t_s)$ the chosen and available site is made with a probability $\exp(-E_A/(k_B T))$.

4. Assuming ergodicity in the simulation, the data in the simulation can be used for analyzing multiple time sequences by shifting configurations at time t_s to the initial time t_0 by setting $\{\mathbf{R}_i(t_s)\} \rightarrow \{\mathbf{R}_i(t_0)\}$.

5. In order to relate the results for various simulation times and supercell sizes, the time counter s is related to a scaled time counter $\bar{s}$ as the average number of hops per ion in the simulation. While the time counter s is used within each simulation, the results are reported in terms of the scaled time counter $\bar{s}$. Explicitly, the scaled time counter is defined according to

$$\bar{s} = \frac{s(1-o)}{N}\mathrm{e}^{-E_A/kT}. \qquad (19)$$

For this simple model, the activation energy E_A is isotropic and configuration independent and therefore the temperature does not contribute to the
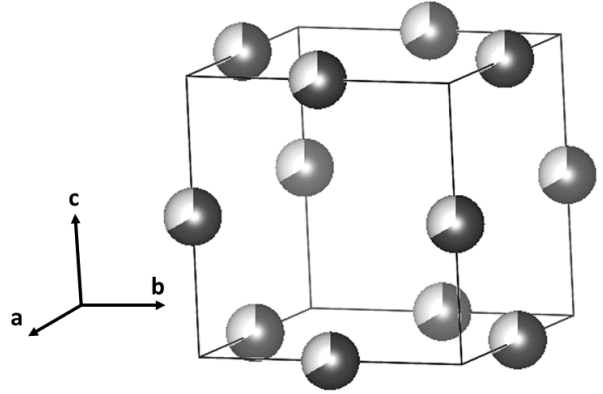

FIG. 1. Cubic unit cell for simulations in this study with the origin at lower back left corner is shown together with available Li sites indicated with two-thirds shaded volumes corresponding to their average occupancy. The fractional coordinates of the unique sites are Li(1) at $(\frac{1}{2}, 0, 0)$, Li(2) at $(0, \frac{1}{2}, 0)$, and Li(3) at $(0, 0, \frac{1}{2})$.

statistical and convergence properties of the simulations. In practice, simulations in the absence of a biasing electric field $\mathbf{F}$ are carried out in the limit of infinite temperature.

6. In order to model the mobility in the presence of an electric field $\mathbf{F}$ according to Eq. 15, the algorithm must be modified in the following way.[20] On a given time step t_s for Step #2c involving ion j, for a possible hop from nearest neighbor sites $\mathbf{R}_j(t_{s-1})$ to $\mathbf{R}_j(t_s)$, it assumed that the activation energy E_A is modified by

$$\epsilon \equiv -\frac{1}{2}eQ\mathbf{F} \cdot (\mathbf{R}_j(t_s) - \mathbf{R}_j(t_{s-1})). \qquad (20)$$

The definition of ϵ is such that for $Q > 0$, when the hop is along the field, the activation energy is slightly lowered. Now the update of $\mathbf{R}_j(t_s)$ is made with a probability $\exp(-(E_A + \epsilon)/(k_B T))$; otherwise the ion position is kept at its earlier position $\mathbf{R}_j(t_s) = \mathbf{R}_j(t_{s-1})$. In practice, the values were chosen such that $\epsilon/(k_B T) = 0.04$ and $E_A/(k_B T) = 1.45$ so that the linear approximation

$$\mathrm{e}^{-(E_A-\epsilon)/(k_B T)} - \mathrm{e}^{-(E_A+\epsilon)/(k_B T)}$$
$$\approx \frac{2\epsilon}{k_B T}\mathrm{e}^{-E_A/(k_B T)}, \qquad (21)$$

was sufficiently accurate and the Monte Carlo acceptance rate was efficient.

The lattice for this study is based on the Li sites available for the disordered cubic phase of Li_2OHCl which is a member of a family of promising solid electrolytes recently studied by our group and others,[4–8] as shown in Fig. 1. The three unique lattice sites within the cubic

unit cell are listed in the figure caption. In this case, each site has a probability of occupancy of $o = \frac{2}{3}$ and has 8 nearest-neighbors ($\nu = 8$). Missing from this model are the effects of the Cl^- ion located at fractional coordinate $(\frac{1}{2}, \frac{1}{2}, \frac{1}{2})$ and the effects of O located at the origin and associated with an OH^- ion. In practice, scaled units are used to measure displacement and time.

$$\delta X_i(t_0, \tau) \rightarrow \delta X_i(t_0, \bar{s})/(a/2) \equiv \delta X_i(t_0, \bar{s}), \qquad (22)$$

where $a/2$ is the hop length along the x-axis for a cubic unit cell of lattice constant a. For convenience, a was taken to be 2 within the Monte Carlo simulations. In the remainder of this paper, all diffusion constants are given in units of the square of the one-dimensional hop length per hop/ion.

IV. RESULTS

A. Statistical analysis of Monte Carlo simulations

There are several competing variables which effect the simulation results, including configuration sampling, number of simulation steps, and sample size. Because of the computational accessibility of the model, we can study each of these separately.

First we consider effects of the initial configurations $\{\mathbf{R}_i(t_0)\}$. In order to illustrate the sensitivity of the "self" $\Delta_{sf}(t_0, \bar{s})$ and "cross" $\Delta_{cr}(t_0, \bar{s})$ terms to the initial configurations, examples are shown in Fig. 2. These examples were generated using supercells of size $12 \times 12 \times 12$ units ($N = 3456$) for two different initial configurations $\{\mathbf{R}_i(t_0^l)\}$, plotted as a function of the scaled step counter $\bar{s}$. From this plot it is apparent that both initial configurations give the same result for $\Delta_{sf}(t_0^l, \bar{s})$ which tends to increase monotonically with time. By contrast, the $\Delta_{cr}(t_0, \bar{s})$ term varies widely as a function of the step counter $\bar{s}$ and very differently for the two different initial configurations. In order to highlight its sensitive behavior, the plots of $\Delta_{cr}(t_0, \bar{s})$ shown in Fig. 2 illustrates some of the extreme variations. For $\Delta_{cr}(t_0^1, \bar{s})$, the values are generally positive, while for $\Delta_{cr}(t_0^2, \bar{s})$ the values are generally negative.

In order to take advantage of statistical analyses of a general result Y_l from this study, it will be convenient to define a mean value and standard deviation according to[22]

$$\langle Y \rangle \equiv M_Y \equiv \frac{1}{L} \sum_{l=1}^{L} Y_l \quad \text{and} \quad \Sigma_Y \equiv \sqrt{\frac{1}{L} \sum_{l=1}^{L} (Y_l - M_Y)^2}, \qquad (23)$$

where L denotes the number of samples. From these values, it is often of practical interest to estimate the number of samples L_f needed to to ensure a fractional error of f. Assuming that the fractional error is well estimated by the ratio of the standard deviation of the
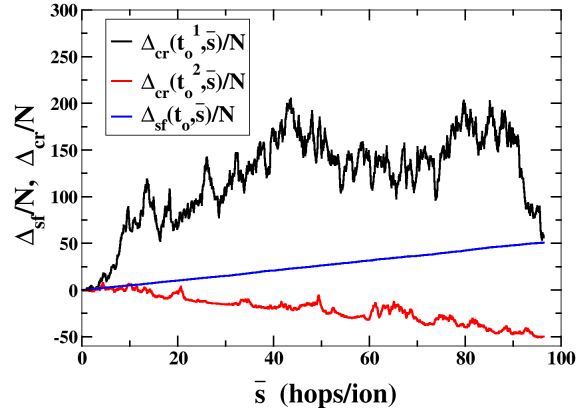

FIG. 2. Comparison of the squared displacement results for a supercell composed of $12 \times 12 \times 12$ units and two initial configurations $\{\mathbf{R}_i(t_0^1)\}$ and $\{\mathbf{R}_i(t_0^2)\}$. Plots illustrate the "self" term $\Delta_{sf}(t_0^l, \bar{s})/N$ and "cross" term $\Delta_{cr}(t_0^l, \bar{s})/N$ ($l = 1, 2$) contributions as functions of the scaled step counter $\bar{s}$. For the samples shown, the curves for $\Delta_{sf}(t_0^1, \bar{s})/N$ and $\Delta_{sf}(t_0^2, \bar{s})/N$ coincide, while the curves for $\Delta_{cr}(t_0^1, \bar{s})/N$ and $\Delta_{cr}(t_0^2, \bar{s})/N$ illustrate two extremes.

mean to the mean value, we can infer that

$$L_f \approx \left(\frac{\Sigma_Y / M_Y}{f} \right)^2, \qquad (24)$$

which follows from the statistical relationship[22] $\Sigma_{M_Y} = \Sigma_Y / \sqrt{L_f}$.

In order to visualize the statistical properties of the squared displacement functions, it is useful to consider histogram plots of their distributions. The simulations were carried out for a supercell composed of $12 \times 12 \times 12$ units ($N = 3456$) fixing the time interval of the simulation corresponding to $\bar{s}$=15 hops/ion. These distributions were generated from $L = 8 \times 10^5$ samples of the initial configurations $\{\mathbf{R}_i(t_0^l)\}$. Figures 3 and 4 show histograpms of $\Delta_{sf}(t_0^l, \bar{s})/(2N\bar{s})$ and $\Delta_{cr}(t_0^l, \bar{s})/(2N\bar{s})$, respectively. These plots show that the distribution for Δ_{sf} has a Gaussian like shape, while the distribution for Δ_{cr} is highly asymmetric. While not presented in a plot, we find that the histogram plot for the corresponding ion mobility $\mu_x(t_0^l)$ given by Eq. 16 also has a Gaussian shaped distribution.

The probability distribution for $Y_l = \Delta_{sf}(t_0^l, \bar{s})/(2N\bar{s})$ is highly localized with Gaussian shape with a mean value of $M_Y = 0.275$ and standard deviation of $\Sigma_Y = 0.007$. The probability distribution for $Y_l = \Delta_{cr}(t_0^l, \bar{s})/(2N\bar{s})$ shows a very asymmetric distribution with average value of $M_Y = 0.055$ and a large standard deviation of $\Sigma_Y = 0.452$. It is apparent from the shape of this probability distribution, that the difficulty in converging $\Delta_{cr}(t_0, \bar{s})$ comes from the non trivial number of large value con-
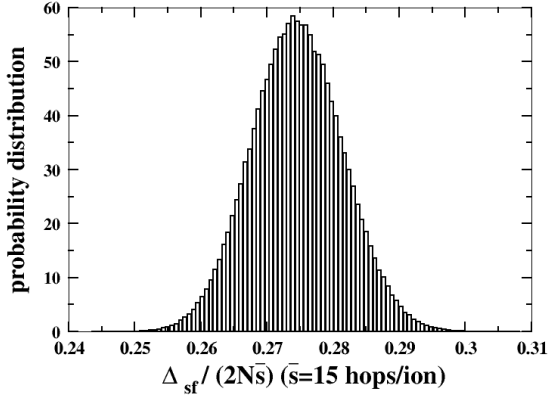
moment component p_x as defined in Eq. (6). The upper bound can be estimated from the value obtained when all of the hops are in the same direction which would result in the very rare upper bound value value of

$$\Delta_{cr} \leq N(N-1)\bar{s}^2. \qquad (26)$$

To better understand the shapes of the probability curves for the self and cross correlation terms, it is useful to consider the analogous quantities that can be derived from a one dimensional random walk. The trajectories of N independent random walkers $\{X_i^{RW}(t_s)\}$ can be used to compute Δ_{sf}^{RW} and Δ_{cr}^{RW} according to Eqs. (7) and (8), respectively. In order to ensure correspondence with our cubic model with $\bar{s} = 15$ hops per ion, the random walk simulations were performed for 10 steps, representing two-thirds of the hops along the x-axis. In calculating these numbers, care was taken to make sure that the their scaling is consistent with the corresponding cubic lattice model. The normalized probability distribution is presented in Fig. 4. For this one dimensional random walk, with $Y = \Delta_{cr}^{RW}/(2N\bar{s})$, the mean value and standard deviations are given by $M_Y = -4 \times 10^{-5}$ and $\Sigma_Y = 0.470$. The corresponding self term $Y = \Delta_{sf}^{RW}/(2N\bar{s})$ for this random walk have the mean value and standard deviation of $M_Y = 0.333$ and $\Sigma_Y = 0.008$, respectively. The numerical values for this one-dimensional random walk system are consistent with the textbook results. They differ from our three-dimensional cubic model system reflecting the effects of geometry and the effects of particle interactions due to site occupations.

Another important consideration is the behavior of the standard deviations of Δ_{sf}, Δ_{cr} and μ_x as a function of simulation size. We have considered supercell sizes of $n \times n \times n$ multiples of the unit cell for $2 \leq n \leq 16$. The ratios of standard deviations to mean values of Δ_{sf}, Δ_{cr} and μ_x are given in Fig. 5. These calculations were all performed at a fixed value of the effective hops $\bar{s}$ and are all well converged with respect to the number of initial configurations $\{\mathbf{R}_i(t_0^l)\}$. These plots show that the $\Sigma_Y/\langle Y \rangle$ ratios converge to 0 with increasing simulation cell size for both Δ_{sf} and μ_x. However, for Δ_{cr}, the $\Sigma_Y/\langle Y \rangle$ ratio seems to asymptote to a non-zero value for very large simulation cell sizes.

Finally we consider the behavior of the standard deviations of Δ_{sf}, Δ_{cr} and μ_x as a function of simulation time as measured by the scaled parameter $\bar{s}$. In order to carry out very long simulations, we consider small supercells composed of $2 \times 2 \times 2$ units with $0 < \bar{s} < 500$. Figure 6 shows that the ratio of $\Sigma_Y/\langle Y \rangle$ for $Y = \Delta_{cr}$ asymptotes to a value which is more than 20 times larger than that of $Y = \Delta_{sf}$. According to Eq. (24), this means that more than 400 times as many samples are needed to converge Δ_{cr} compared with Δ_{sf}.

We also examined the convergence of the standard deviation in simulating the mobility at different electric field strengths as shown in Fig. 7. This plot shows that the standard deviation ratio asymptotes to zero for $\bar{s} \to \infty$, although a larger field strength (within the linear
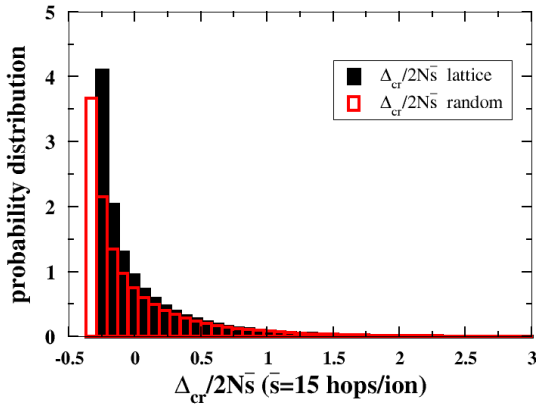

FIG. 3. Distribution of values of $\Delta_{sf}(t_0, \bar{s})/(2N\bar{s})$ at a fixed time interval $\bar{s}$ corresponding to $\bar{s} = 15$ hops/ion for a $12 \times 12 \times 12$ supercell ($N = 3456$). The probability distribution was constructed with 8×10^5 initial configurations and normalized to unity.

FIG. 4. Distribution of values of $\Delta_{cr}(t_0, \bar{s})/(2N\bar{s})$ at a fixed interval $\bar{s}$ corresponding to $\bar{s} = 15$ hops/ion for $12 \times 12 \times 12$ supercell ($N = 3456$). The probability distribution was constructed with 8×10^5 initial configurations and normalized to unity presented with filled black bars. The equivalent distribution for a one-dimensional random walk is represented with red-outlined bars for comparison.

tributions. While the probability density of these large value contributions is small, their contribution is significant. The range of values of Δ_{cr} can be estimated as follows. At the lower bound,

$$\Delta_{cr} \geq -\Delta_{sf}, \qquad (25)$$

which follows from the fact that the sum of $\Delta_{sf} + \Delta_{cr} \geq 0$, because of its proportionality to the squared length of the

FIG. 5. Ratios of standard deviations to mean values of Δ_{sf} and μ_x (left scale) and Δ_{cr} (right scale) as a function of the supercell size parameter n. For Δ_{sf} and Δ_{cr}, the calculations were performed at $\bar{s} = 15$ hops/ion. For μ_x the calculations were performed with 6 hops/ion on average along the field direction, corresponding approximately to $\bar{s} = 880$ hops/ion. The parameters $E_A/(k_B T)$ and $\epsilon/(k_B T)$ were taken as described in Sec. III.
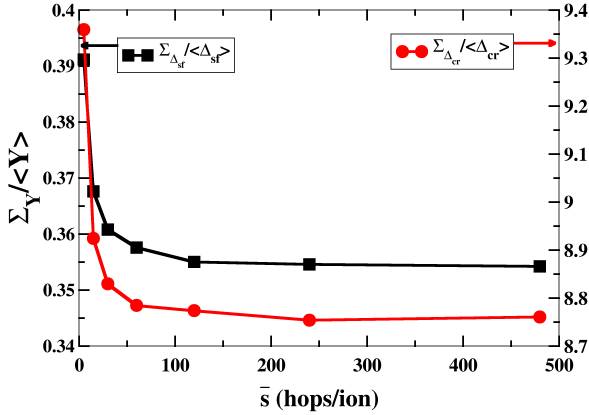

FIG. 7. Values of $\Sigma_Y/\langle Y \rangle$ for $Y = \mu_x$ as a function of $\bar{s}$ for very long simulations performed for $2 \times 2 \times 2$ supercells ($N = 16$). Results for two different values of field strength as measured by $\varepsilon/(k_B T)$ are presented. For both cases the same activation energy of $E_A/(k_B T) = 1.45$ was used.

FIG. 6. Values of $\Sigma_Y/\langle Y \rangle$ for $Y = \Delta_{\mathrm{sf}}$ (left scale) and for $Y = \Delta_{\mathrm{cr}}$ (right scale) as a function of $\bar{s}$ for very long simulations. Simulations were performed in $2 \times 2 \times 2$ supercells ($N = 16$).
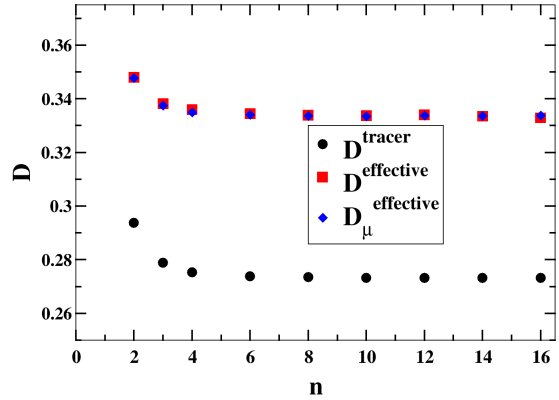
FIG. 8. Comparison of diffusion constants D^{tracer}, $D^{\mathrm{effective}}$, and $D_\mu^{\mathrm{effective}}$ calculated using Eqs. (9), (11), and (17), respectively as a function n representing the supercell multiplicity of $n \times n \times n$. All calculations were performed in the $\bar{s} \to \infty$ limit and are also well converged with respect to initial configurations $\{\mathbf{R}_i(t_0)\}$.

range) converges more rapidly.

B. Convergence of the transport coefficients

For evaluating the diffusion constants D^{tracer}, $D^{\mathrm{effective}}$, and $D_\mu^{\mathrm{effective}}$, it is necessary to carry out the simulations in the $\bar{s} \to \infty$ limit. These quantities are

shown in Fig. 8 as a function of of simulation cell size. Results also show that the results calculated using the Kubo formalism and the using the Ohm's law formalism are in very good agreement. The standard deviation of the results due to the averaging over initial configurations $\{\mathbf{R}_i(t_0)\}$ is too small to be seen on this scale.

In order to see the results in a little more detail, Fig. 9 shows the Haven ratio as defined in Eq. (12) as a function
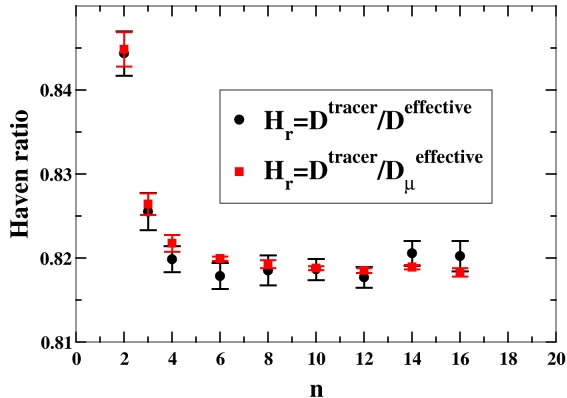
FIG. 9. Simulated values of the Haven ratio H_r as defined by Eq. (12) as a function of the simulation cell parameter n, comparing results calculated using the Kubo and Ohm's law methods. The error bars on the graph indicate the standard deviation of the mean of the value. The calculations were performed with $\bar{s} \to \infty$ and a large number of initial configurations.

TABLE I. Values of fitting parameters defined in Eq. (27) used for diffusion coefficients simulated with the kinetic Monte Carlo model for $n \times n \times n$ supercells.

n	D_∞	w
2	0.054	0.344
6	0.060	0.472

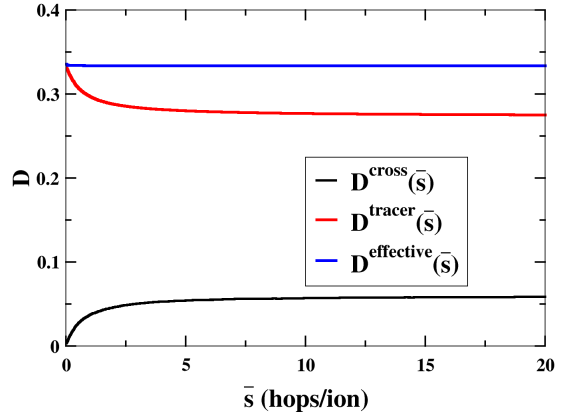FIG. 10. Convergence of $D^{\text{effective}}(\bar{s})$, $D^{\text{tracer}}(\bar{s})$ and $D^{\text{cross}}(\bar{s})$ as defined in Eqs. (11), (9) and (10), before taking the asymptotic limit, as a function of $\bar{s}$. Simulations were performed on a $6 \times 6 \times 6$ supercell.

of simulation cell size. These results show that very good convergence at a value of $H_r = 0.819$ is achieved for a supercell size of $6 \times 6 \times 6$. On this scale, the error bars (representing the standard deviation of the mean) are visible, but small for both the Kubo and Ohm's law simulations.

Finally, in Fig. 10, a more realistic estimate of the time convergence of the diffusion constant is presented for simulations on $6 \times 6 \times 6$ unit supercells. These calculations were performed on a very large number of initial configurations so that the values are converged with their standard deviation of the mean values smaller than the line width of the plot. For these highly sampled simulations, the time convergence of D^{tracer} mirrors that of D^{cross} such that their time convergence for the individual terms is seen to be quite good at $\bar{s} = 2$ hops/ion. Interestingly, the total diffusion $D^{\text{effective}}$ converges at short times for this model.

For the highly sampled simulations in cubic simulation cells, the time convergence of the diffusion coefficients can be can be well interpolated by a simple analytic form based on a single exponential:

$$D^{\text{cross}}_{\text{model}}(\bar{s}) \approx D_\infty e^{-w/\bar{s}}, \qquad (27)$$

where D_∞ and w are fitting parameters. For the $6 \times 6 \times 6$ supercell shown in Fig. 10. Some typical values of the fitting parameters are given in Table I. For asymmetric simulation cells, it is found that typically more than one exponential function is needed to achieve an accurate fit.

V. ANALYSIS

A. Properties of the cross particle displacement contributions

The simulations presented in Sec. IV A document how sensitive the calculations are to the cross particle contributions given by $\Delta_{\text{cr}}(t_0, \tau)$ as defined in Eq. (8). In this section, the term is analyzed further in order to detail its properties. An important point to make about Eq. (8) is that for a collection of truly random and independent hoping events, the ensemble average $\langle \delta X_i(t_0, \tau) \delta X_j(t_0, \tau) \rangle_{t_0}$ is equal to zero. Consequently, the extent to which $\langle \Delta_{\text{cr}}(t_0, \tau) \rangle_{t_0}$ differs from zero is a measure of correlations in the system. Ideally, one could reformulate Eq. (8) into correlated contributions to include in the evaluation in such a way that they well approximate $\langle \Delta_{\text{cr}}(t_0, \tau) \rangle_{t_0}$. Denoting this correlated cross particle displacement contribution by $\langle \Delta_{\text{cr}}^{\text{corr}}(t_0, \tau) \rangle_{t_0}$, we expect that it should well approximate the full contribution in the sense that

$$\left| \langle \Delta_{\text{cr}}^{\text{corr}}(t_0, \tau) \rangle_{t_0} - \langle \Delta_{\text{cr}}(t_0, \tau) \rangle_{t_0} \right| < \epsilon. \qquad (28)$$

where ϵ is some small number within the desired convergence criteria.

In order formulate the correlated contributions, we first

partition the particle displacement defined in Eq. (5) into a sum over sequential displacements. For displacement along the x-axis, we define a displacement "event" $\Lambda_{i\lambda}(t_0)$ such that

$$\delta X_i(t_0,\tau) \equiv X_i(t_0+\tau) - X_i(t_0) = \sum_{\lambda=1}^{\hat{s}} \Lambda_{i\lambda}(t_0). \quad (29)$$

Here λ is an index for the time sequence similar to that defined in Eq. (18)

$$t_\lambda = t_0 + \lambda\delta\hat{\tau}, \quad (30)$$

where it is computationally efficient to define the time increment $\delta\hat{\tau}$ to be an integer multiple of $\delta\tau$ used in simulation so that $\delta\hat{\tau} > \delta\tau$. In this work, a $\delta\hat{\tau}$ equivalent to the incremental scaled step counter $\Delta\bar{s} = 0.25$ hops/ion was used. The displacement event for particle i is then defined according to

$$\Lambda_{i\lambda}(t_0) \equiv X_i(t_0 + \lambda\delta\hat{\tau}) - X_i(t_0 + (\lambda-1)\delta\hat{\tau}). \quad (31)$$

Accordingly, the maximum step counter, $\hat{s}$, for the coarse grained evaluation is chosen such that $\hat{s}\delta\hat{\tau} = \tau$. Now the cross interaction term of Eq. (8) can be equivalently rewritten in the form

$$\Delta_{\mathrm{cr}}(t_0,\tau) = \sum_{i(\neq j)=1}^{N}\sum_{j=1}^{N}\sum_{\lambda=1}^{\hat{s}}\sum_{\lambda'=1}^{\hat{s}} (\Lambda_{i\lambda}(t_0)\Lambda_{j\lambda'}(t_0)). \quad (32)$$

In this formulation, the idea is to choose from all of the cross event products $\Lambda_{i\lambda}(t_0)\Lambda_{j\lambda'}(t_0)$, only those which are "correlated". The expectation is that the correlation is limited in time and space, so that it should be possible choose cutoff parameters t_{cut} and R_{cut} to limit the full summation in Eq. (32) in the form

$$\Delta_{\mathrm{cr}}^{\mathrm{corr}}(t_0,\tau) = \sum_{i(\neq j)=1}^{N}\sum_{j=1}^{N}\sum_{\lambda=1}^{\hat{s}}\sum_{\lambda'=1}^{\hat{s}} (\Lambda_{i\lambda}(t_0)\Lambda_{j\lambda'}(t_0)) \times \\ f_{ij\lambda\lambda'}(t_{\mathrm{cut}}, R_{\mathrm{cut}}), \quad (33)$$

where $f_{ij\lambda\lambda'}(t_{\mathrm{cut}}, R_{\mathrm{cut}})$, represents a function designed to model the correlations of the system. For example, a simple functional form can be written in terms of the Heaviside step functions $\Theta(x)$,

$$f_{ij\lambda\lambda'}(t_{\mathrm{cut}}, R_{\mathrm{cut}}) \equiv \Theta\left(t_{\mathrm{cut}} - |\lambda' - \lambda|\delta\hat{\tau}\right) \times \\ \Theta\left(R_{\mathrm{cut}} - |\mathbf{R}_j(t_0 + \lambda'\delta\hat{\tau}) - \mathbf{R}_i(t_0 + \lambda\delta\hat{\tau})|\right). \quad (34)$$

We first examine the effects of choosing a time correlation in terms of t_{cut} while setting R_{cut} such that the summation includes all events on the basis of their separation, using a $2\times2\times2$ supercell. For this case we find that choosing t_{cut} corresponding to the scaled time counter $\bar{s}_{\mathrm{cut}} = 2$ hops/ion, results in a convergence parameter defined in Eq. (28) to be $\epsilon/\left|\langle\Delta_{\mathrm{cr}}^{\mathrm{corr}}(t_0,\tau)\rangle_{t_0}\right| \leq 1\%$. This result
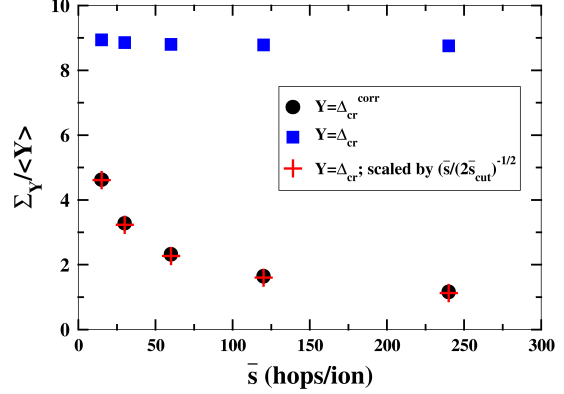

FIG. 11. Comparison of fractional standard deviations $\Sigma_Y/\langle Y\rangle$ for correlated and non-correlated evaluations of cross-interaction displacements evaluated for $2 \times 2 \times 2$ supercells. For $\langle\Delta_{\mathrm{cr}}^{\mathrm{corr}}(t_0,\tau)\rangle_{t_0}$, the time correlation was chosen corresponding to $\bar{s}_{\mathrm{cut}} = 2$ hops/ion, while the spatial correlations were unrestricted. The plus symbols denote results derived from the full calculations of $\langle\Delta_{\mathrm{cr}}(t_0,\tau)\rangle_{t_0}$ scaled as explained in the text.

illustrates how the time correlation of "event products" differs from time convergence of cross-interaction diffusion. For this system, the interpolation model defined in Eq. (27) fits the simulation with $D_\infty = 0.054$ and $w = 0.344$. This means that any simulation which is well converged with respect to initial configurations carried out to a time interval equivalent to $\bar{s} = 2$ hops/ion, has an error of 16% relative to the time converged value because $D^{\mathrm{cross}}(\bar{s} = 2)/D^{\mathrm{cross}} = 0.84$. In order to reduce the convergence error to 1%, one needs to carry out the simulations out to a time interval equivalent to $\bar{s} = 34$ hops/ion. Nevertheless, in the formulation of the cross interaction diffusion in terms of event products as given in Eq. (33), we see that keeping only product pairs whose time differences are within t_{cut} corresponding to $\bar{s}_{\mathrm{cut}} = 2$ hops/ion gives good results. To examine this further, we consider the fractional variances $\Sigma_Y/\langle Y\rangle$ for $\langle Y\rangle = \langle\Delta_{\mathrm{cr}}(\bar{s})\rangle_{t_0}$ and $\langle\Delta_{\mathrm{cr}}^{\mathrm{corr}}(\bar{s})\rangle_{t_0}$ as shown in Fig. 11. Here we see that the fractional standard deviation computed using the correlated events converges toward zero while the fractional standard deviation computed using the full cross displacement asymptotes to constant value, consistent with the notion that keeping only the correlated events reduces the noise of the calculation. It is also interesting to note an empirical scaling relationship between the fractional variance is found to be

$$\frac{\Sigma_{\Delta_{\mathrm{cr}}^{\mathrm{coor}}(\bar{s})}}{\langle\Delta_{\mathrm{cr}}^{\mathrm{coor}}(\bar{s})\rangle} \approx \frac{\Sigma_{\Delta_{\mathrm{cr}}(\bar{s})}}{\langle\Delta_{\mathrm{cr}}(\bar{s})\rangle}\frac{1}{\sqrt{\bar{s}/(2\bar{s}_{\mathrm{cut}})}}, \quad (35)$$

where in this case $\bar{s}/(2\bar{s}_{\mathrm{cut}})$ represents a multiplier for the data sampling made possible by including the correlated
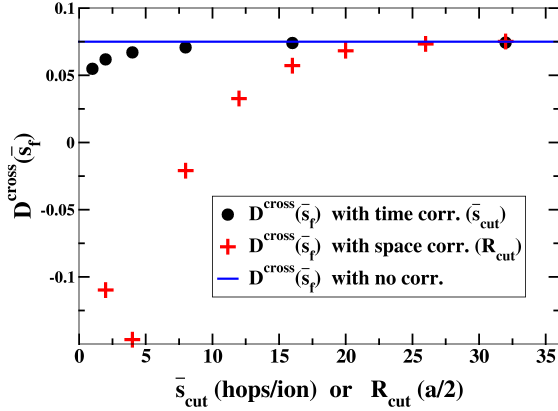
FIG. 12. Plots of $D^{\mathrm{cross}}(\bar{s}_f)$ evaluated for a $80 \times 2 \times 2$ supercell for $\bar{s}_f = 62$ hops/ion. The blue line shows the value calculated using Eq. (8). The black circles show the results obtained from using Eq. (33) to calculate $\langle \Delta_{\mathrm{cr}}^{\mathrm{corr}}(t_0, \tau) \rangle_{t_0}$ with $\bar{s}_{\mathrm{cut}}$ as indicated on the horizontal axis (in units of hops/ion) and no spatial correlation. The red crosses show the results obtained from using Eq. (33) to calculate $\langle \Delta_{\mathrm{cr}}^{\mathrm{corr}}(t_0, \tau) \rangle_{t_0}$ with R_{cut} as indicated on the horizontal axis (in units of $a/2$) and no time correlation.

terms in Eq. (33) with t_{cut}. This scaling is shown in Fig. 11.

In investigating spatial correlations in evaluating Eq. (33), it was found that a large value of R_{cut} is needed to converge the cross interaction diffusion. For example, for cubic $n \times n \times n$ supercells, for all $1 \leq n \leq 16$, we found it necessary to include all events in the simulation according to their spatial separation in order to achieve converged results for $\Delta_{\mathrm{cr}}^{\mathrm{corr}}$. Because the restricted sum in Eq. (33) for our model scales as $2n^6\hat{s}^2$, it is computationally difficult to examine cubic simulation cells with $n > 16$. However, it is feasible to study the nature of the long spatial range correlations, within an asymmetric supercell. For example, we performed a series of simulations for the $80 \times 2 \times 2$ supercell system, separately studying the effects of time and space correlations. The results are presented in Fig. 12. For this system, we found that $D^{\mathrm{cross}}(\bar{s}_f)/D^{\mathrm{cross}}(\bar{s} \to \infty){=}95\%$ for $\bar{s}_f = 62$ hops/ion and that value was used in the evaluations presented in the figure. The results show that for this system the time correlation is well converged for $\bar{s}_{\mathrm{cut}} \geq 8$ hops for ions, but the spatial correlation is only well converged at a distance of $R_{\mathrm{cut}} \geq 20a/2$.

B. Statistical analysis of first principles simulations

The inspiration for this detailed study of the statistical properties of transport coefficients came from our recent
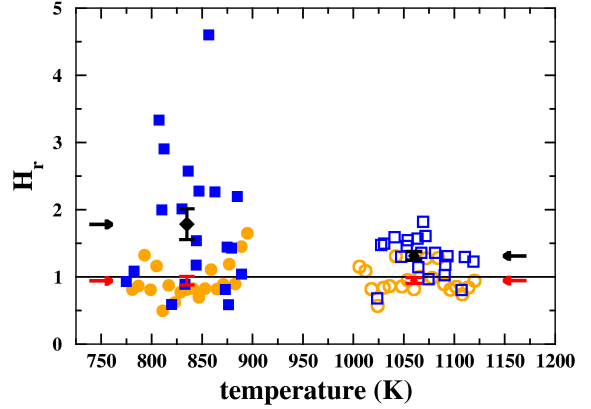

FIG. 13. Results of combined first principles and Monte Carlo study of the Haven ratio for the disordered cubic phase of $\mathrm{Li_2OHCl}$ simulated at a target temperature of 750 K (filled symbols) and a target temperature of 1000 K (open symbols). For each target temperature, the blue symbols indicate the first principles results calculated for 20 initial configurations at the indicated average temperatures. The orange symbols indicate the Monte Carlo results calculated for 20 initial configurations with comparable statistics to the first principles runs as explained in the text. For the Monte Carlo results the horizontal axis placement is arbitrarily assigned for visualization. The averaged first principles results are indicated with black symbols and variance error bars. The averaged Monte Carlo results are indicated with red symbols and variance error bars. The black and red arrows highlight the averaged first principles and Monte Carlo values of H_r.

first principles investigation[7] of the solid state electrolyte $\mathrm{Li_2OHCl}$. In the disordered cubic phase of this material, the Li sublattice is the same as that shown in Fig. 1. While the first principles simulations are able to incorporate much more physically realistic interactions of the material into the simulations, the increased physical accuracy reduces the number of hops/ion possible compared to the results obtained with the same computer resources using the kinetic Monte Carlo model. The hope is that our kinetic Monte Carlo simulations for this system can be used together with the first principles simulations to obtain a more complete understanding of its ionic diffusion. Of particular interest is the result suggested by comparing simulations for D^{tracer} with experimental results for the ionic conductivity using Eq. 13, that at experimentally accessible temperatures, the Haven ratio H_r for this system is greater than 1 and increases with decreasing temperature.

In the present work, we performed both first principles simulations and kinetic Monte Carlo simulations using $2 \times 2 \times 2$ supercells. Apart from using a smaller simulation cell in order to improve the computational statistics, the computational methods used for the first principles simu-

lations were the same as those used in our previous work.[7] In particular, the first principles formalism is based on density functional theory (DFT)[23,24] implemented using the projector augmented wave (PAW) method[25] using the Quantum Espresso software package.[26] The calculational parameters were similar to those specified in the previous publication[7] except that the plane wave expansion of the wavefunctions included reciprocal lattice vectors $|\mathbf{k} + \mathbf{G}|^2 \leq 35$ Ry and the wave vector sampling of the Brillouin zone included a $2 \times 2 \times 2$ grid.

For this study, twenty randomly generated configurations were prepared for $2 \times 2 \times 2$ supercells representing the disordered cubic phase of Li_2OHCl. The cubic lattice constant was fixed at $a = 3.91$ Å. The eight O and eight Cl positions were fixed at their ideal lattice positions. The 16 Li positions were randomly selected based on the unit cell shown in Fig. 1 and hydrogen locations were placed with the OH bond length assumed to be 1.0 Å and a randomly chosen bond angle within all possible 4π radians. For each of the twenty initial structures, the static lattice internal energies were optimized at constant volume. Subsequently, first principles molecular dynamics simulations for these twenty optimized structures were performed at constant volume for two different target temperatures of $T = 750$ K and $T = 1000$ K. The simulations were performed in a microcanonical ensemble, at constant energy in terms of the kinetic energy associated with nuclear motion and electronic total DFT energy. The approximate simulation temperatures were controlled by initiating the calculations with velocity distributions corresponding to twice the target temperature values. While the first principles simulation times extended to $\tau = 180\text{-}250$ ps for the simulations at target temperature $T = 750$K and to $\tau = 90\text{-}170$ ps for the simulations at target temperature $T = 1000$K, it is clear that the results are not converged with respect to configuration averaging and with simulation time. Nevertheless, by pairing the first principles results with analogous kinetic Monte Carlo simulations, taking care to use equivalent levels of statistics, it is possible to make a statistically significant differentiation of the two models. In this case, the first principles simulations include, in addition to the realistic treatment of interparticle interactions, the effects of lattice vibrations, and a possible "gating" mechanism of the OH bond orientation. On the other hand, the kinetic Monte Carlo model includes only the geometric features of the Li sublattice.

In order to align the two calculations, we noted that for the kinetic Monte Carlo simulations, the parameter $\bar{s}$ represents the hops/ion. According to the extension of Eq. 7 for three dimensional diffusion, the hops/ion can be estimated for a first principles simulation at a time duration τ according to

$$\bar{s}_\tau \approx \frac{\Delta^x_{\mathrm{sf}}(t_0, \tau) + \Delta^y_{\mathrm{sf}}(t_0, \tau) + \Delta^z_{\mathrm{sf}}(t_0, \tau)}{N(a^2/2)}. \qquad (36)$$

In this case $a^2/2$ approximates the three dimensional hop length for this system, and $\bar{s}_\tau$ approximates the number

of hops for the simulation time τ. It is reasonable to assume that the hop counter $\bar{s}_\tau$ determined from each first principles simulation run is analogous to the scaled hop counter $\bar{s}$ used in the Monte Carlo simulations. In this way, we could deduce that on average the two sets of temperature simulations corresponded to $\bar{s} = 11$ hops/ion and $\bar{s} = 3.5$ hops/ion for the 1000 K and 750 K simulations respectively. The corresponding ranges of $\bar{s}$ were 4.75-21.25 and 1.5-5.6, respectively. In order to improve the statistical sampling, each of the first principles simulations were analyzed separately, averaging the results for the entire runs into $\bar{s} = 1$ hop/ion segments and determining the average temperature of each run. Correspondingly, for both the $T = 1000$ K and $T = 750$ K temperature ranges, sets of 20 Monte Carlo simulations were performed using similar sampling statistics. That is for each Monte Carlo run, the total simulation was fixed at $\bar{s} = 11$ (3.5) hops/ion for the $T = 1000$ K (750 K) cases and the results for the entire run was averaged by analyzing $\bar{s} = 1$ hop/ion segments. While physical temperature effects are not explicitly included in the Monte Carlo runs, their effects on the statistical sampling was modeled as closely as possible in this way. The results were analyzed in terms of the Haven ratios, calculated from Eq. (12) at finite simulation time corresponding to $\bar{s} = 1$ hop/ion and the results are presented in Fig. 13.

The results for H_r shown in Fig. 13 show substantial statistical noise as well as systematic error, however a clear distinction of the behavior of ion diffusion in the realistic "first principles" model relative to that of the kinetic Monte Carlo results is demonstrated. Knowledge of systematic errors comes from the Monte Carlo studies for which it was shown previously that at this level of statistical time, that the simulations were still not at their asymptotic limit. The value of the Haven ratio from the Monte Carlo model for a $2 \times 2 \times 2$ supercell converged with time intervals of $\bar{s} = 1$ hop/ion is $H_r \approx 0.92$, while the converged value is $H_r = 0.84$. Nevertheless, the results for the first principles simulations suggest that $H_r > 1$ in the temperature range of $T = 750$ K and $T = 1000$ K and also suggest a temperature dependence of H_r such that $H_r(750 \text{ K}) > H_r(1000 \text{ K})$. The simulations at $T = 750$ and 1000 K were performed in order to improve the statistics, but in reality the material is not expected to exist in its crystalline form at such high temperatures. In our previous work,[7] the suggestion was made that H_r is significantly larger than 1 in the temperature range of $315 < T < 470$ K based on simulations with inferior statistics and comparing to experimental conductivity measurements at those temperatures.

It is also interesting to consider possible mechanisms that cause $H_r > 1$ for this system. A possible physical mechanism comes from observing the short time behavior of $D^{\mathrm{cross}}(\tau)$ which is shown in Fig. 14. In Fig. 14, the value of $D^{\mathrm{cross}}(\tau)$ is shown for a simulation with average temperature 1074K simulated to 140ps and final value of $\Delta_{\mathrm{sf}}/N = 89\text{Å}^2$. In this calculation, the averaging over initial configurations was achieved by averaging the full
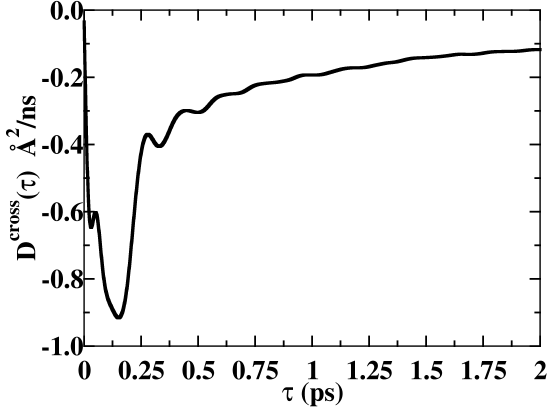
FIG. 14. Results of first-principles molecular dynamics simulation of $2 \times 2 \times 2$ supercell of Li_2OHCl at a temperature of $T = 1074K$ to determine $D^{\mathrm{cross}}(\tau)$ for $0 \leq \tau \leq 2$ ps.

simulations in terms of $\tau = 7$ps segments; the first 2ps of the resultant $D^{\mathrm{cross}}(\tau)$ are presented. It is interesting that $D^{\mathrm{cross}}(\tau) < 0$ throughout this time range and that within the first 0.2 ps there is a negative dip indicating the short time motions (vibrations) of the lithium atoms are anti-correlated. It can be argued that this anti-correlated property of the short time motion of the lithium ions contributes to the net bias for anti-correlated hopping which leads to a Haven ratio greater than 1.

VI. SUMMARY AND CONCLUSIONS

The results of this study both provides insight into the transport properties of a specific system, the disordered cubic phase of Li_2OHCl, and also provides detailed analysis of the statistical and convergence properties of transport simulations more generally. The work in this paper was motivated by the challenge of reaching the large statistical time scales (hops/ion) necessary to study these convergence properties. With the help of a lattice kinetic Monte Carlo model, it is possible to explore aspects of the transport simulations which rely on long simulation times, large simulation cells, and sampling over large numbers of initial configurations. For the Li_2OHCl system, we have been able to use the lattice kinetic Monte Carlo model together with first principles simulations to improve the prediction of the ionic correlations. While the lattice kinetic Monte Carlo model used in this work was based on the Li sublattice of the disordered cubic phase of Li_2OHCl, we expect that the qualitative statistical and convergence properties of the results can be generalized to other lattices.

In this work, we considered both transport coefficients calculated in absence and presence of an applied electric field. Evaluated for a fixed supercell and fixed simulation time, the distribution of values obtained for different initial configurations was determined. We found that the distributions for $\Delta_{\mathrm{sf}}(t_0, \bar{s})/2N\bar{s}$ and correspondingly $\mu_x(t_0, \bar{s})$ have a Gaussian shape and standard deviation that approaches zero in the limit of large sample size as represented by large supercells in the periodic boundary formulation. By contrast, the distribution of values of $\Delta_{\mathrm{cr}}(t_0, \bar{s})/2N\bar{s}$ is found to have a very asymmetric distribution with a standard deviation that limits to a non-zero constant in the large supercell limit. The ratio of the standard deviation to mean value is found to limit to a non-zero constant in time for both the Δ_{sf} and Δ_{cr} terms. However, the ratio of the standard deviation to mean value of μ_x tends to zero in the long time limit at a rate that depends on the applied field strength used in the calculations. The statistical results indicate that for the Kubo formalism, the primary difficulty of convergence is due to the Δ_{cr} term which requires a large number of initial configurations. For the Ohm's law formulation of the transport simulations, the statistical results indicate that calculation of ionic conductivity would benefit from use of a field strength adjusted to the largest magnitude possible while still remaining in the linear response regime. Adapting the Ohm's law formulation to first principles simulations would need additional considerations.

The lattice kinetic Monte Carlo simulations also were used to assess the convergence of the transport parameters with respect to simulation time and system size given high convergence with respect to initial configurations. In terms of supercell size, the results show that for this lattice geometry the properties of interest are well converged for a cubic supercell composed of $6 \times 6 \times 6$ unit cells. In terms of simulation time, the results for cubic supercells, both $D^{\mathrm{tracer}}(\bar{s})$ and $D^{\mathrm{cross}}(\bar{s})$ can be represented by a simple interpolation form from which the asymptotic form can be determined. For the lattice considered in this work, $D^{\mathrm{effective}}(\bar{s})$ converged at very short time. It is not clear whether or not this feature is more generally true for other lattice geometries.

This work also introduces an alternate formulation of Δ_{cr} in terms of a sum over event products for the purpose of considering temporal and/or spatial correlations. For an example system, we found that including only event pairs separated in time by $\bar{s}_{\mathrm{cut}}=2$ hops/ion or less in the calculation of $\Delta_{\mathrm{cr}}^{\mathrm{corr}}$ reduced the fractional standard deviation substantially. This suggests that correlations can be used to reduce the noise in the calculation and therefore improving the calculational efficiency. Translating this idea into a practical computational scheme is not trivial, since it is generally difficult to estimate $\bar{s}_{\mathrm{cut}}$, but probably worth further consideration. This study also showed that spatial correlations in this system are long range.

The lattice kinetic Monte Carlo simulations were used to closely analyze the statistics of analogous first principles simulations of $\Delta_{\mathrm{cr}}(t_0, \tau)$ the full Li_2OHCl lattice. We were able to improve the statistical analysis to pro-

vide further evidence about the Haven ratio, showing that $H_r > 1$ at the simulation temperatures. Interestingly, a plot of $D^{\text{cross}}(\tau)$ from the first principles simulations, shows negative values for $0 \leq \tau \leq 2$ ps with a negative peak at approximately $\tau = 0.2$ ps. This time generally corresponds to vibrational modes in the lattice and suggests that these vibrations may lead to short time anti-correlated motions. The first principles result for $D^{\text{cross}}(\tau)$ shown in Fig. 14 can be contrasted with the corresponding result for the lattice kinetic Monte Carlo model which has a shape similar to that shown in Fig. 10, monotonically increasing above zero. This example shows how the lattice kinetic Monte Carlo sim-

ulations can be used to estimate the level of statistics necessary to converge the more accurate simulations of the the transport parameters. The lattice kinetic Monte Carlo results for the transport parameters can also serve as a well defined reference which captures the geometric and site blocking effects.

* email:natalie@wfu.edu

[1] N. Kamaya, K. Homma, Y. Yamakawa, M. Hirayama, R. Kanno, M. Yonemura, T. Kamiyama, Y. Kato, S. Hama, K. Kawamoto, and A. Mitsui, Nature Materials **10**, 682 (2011).

[2] D. Zahn, Journal of Molecular Modeling **17**, 1531 (2011).

[3] Y. Mo, S. P. Ong, and G. Ceder, Chemistry of Materials **24**, 15 (2012).

[4] Z. D. Hood, H. Wang, A. Samuthira Pandian, J. K. Keum, and C. Liang, Journal of the American Chemical Society **138**, 1768 (2016).

[5] Y. Li, W. Zhou, S. Xin, S. Li, J. Zhu, X. L, Z. Cui, Q. Jia, J. Zhou, Y. Zhao, and J. B. Goodenough, Angewandte Chemie International Edition **55**, 9965 (2016).

[6] G. Schwering, A. Hönnerscheid, L. van Wüllen, and M. Jansen, ChemPhysChem **4**, 343 (2003).

[7] J. Howard, Z. D. Hood, and N. A. W. Holzwarth, Phys. Rev. Materials **1**, 075406 (2017).

[8] A.-Y. Song, Y. Xiao, K. Turcheniuk, P. Upadhya, A. Ramanujapuram, J. Benson, A. Magasinski, M. Olguin, L. Meda, O. Borodin, and G. Yushin, Advanced Energy Materials , 1700971 (2017).

[9] K. Campaan and Y. Haven, Transactions of the Faraday Society **54**, 1498 (1958).

[10] Y. Haven and B. Verkerk, Physics and chemistry of glasses **6**, 38 (1965).

[11] A. D. Le Claire, "Correlation Effects in Diffusion in Solids," in *Physical Chemistry An Advanced Treatise, Volume X/Solid State*, edited by W. Jost (Academic Press, New York, 1970) Chap. 5, pp. 261–330.

[12] G. Murch, Solid State Ionics **7**, 177 (1982).

[13] A. Marcolongo and N. Marzari, Physical Review Materials **1**, 025402 (2017).

[14] X. He, Y. Zhu, and Y. Mo, Nature Communications **8**, 15893 (2017).

[15] A. Van der Ven, G. Ceder, M. Asta, and P. D. Tepesch, Physical Review B **64**, 184307 (2001).

[16] R. Kubo, Journal of the Physical Society of Japan **12**, 570 (1957).

[17] J. M. Haile, *Molecular Dynamics Simulation: Elementary Methods* (John Wiley & Sons, Inc., 1992) iSBN: 978-0-471-81439-3.

[18] N. Kuwata, X. Lu, T. Miyazaki, Y. Iwai, T. Tanabe, and J. Kawamura, Solid State Ionics **294**, 59 (2016).

[19] N. Metropolis, A. W. Rosenbluth, M. N. Rosenbluth, A. H. Teller, and E. Teller, The Journal of Chemical Physics **21**, 1087 (1953).

[20] J. Manning, *Diffusion Kinetics for Atoms in Crystals* (Van Nostrand, 1968).

[21] S. Ihara and K. Suzuki, Journal of the Physical Society of Japan **55**, 1695 (1986).

[22] P. R. Bevington, *Data Reduction and Error Analysis for the Physical Sciences* (McGraw-Hill Book Company, 1969).

[23] P. Hohenberg and W. Kohn, Physical Review **136**, B864 (1964).

[24] W. Kohn and L. J. Sham, Physical Review **140**, A1133 (1965).

[25] P. E. Blöchl, Phys. Rev. B **50**, 17953 (1994).

[26] P. Giannozzi, O. Andreussi, T. Brumme, O. Bunau, M. B. Nardelli, M. Calandra, R. Car, C. Cavazzoni, D. Ceresoli, M. Cococcioni, N. Colonna, I. Carnimeo, A. D. Corso, S. de Gironcoli, P. Delugas, R. A. D. Jr, A. Ferretti, A. Floris, G. Fratesi, G. Fugallo, R. Gebauer, U. Gerstmann, F. Giustino, T. Gorni, J. Jia, M. Kawamura, H.-Y. Ko, A. Kokalj, E. Kkbenli, M. Lazzeri, M. Marsili, N. Marzari, F. Mauri, N. L. Nguyen, H.-V. Nguyen, A. O. de-la Roza, L. Paulatto, S. Ponc, D. Rocca, R. Sabatini, B. Santra, M. Schlipf, A. P. Seitsonen, A. Smogunov, I. Timrov, T. Thonhauser, P. Umari, N. Vast, X. Wu, and S. Baroni, Journal of Physics: Condensed Matter **29**, 465901 (2017).

Bibliography

[1] P. Hohenberg and W. Kohn. Inhomogeneous electron gas. *Physical Review*, 136:B864–B871, 1964.

[2] W. Kohn and L. J. Sham. Self-consistent equations including exchange and correlation effects. *Physical Review*, 140:A1133–A1138, 1965.

[3] Paolo Giannozzi, Stefano Baroni, Nicola Bonini, Matteo Calandra, Roberto Car, Carlo Cavazzoni, Davide Ceresoli, Guido L Chiarotti, Matteo Cococcioni, Ismaila Dabo, Andrea Dal Corso, Stefano de Gironcoli, Stefano Fabris, Guido Fratesi, Ralph Gebauer, Uwe Gerstmann, Christos Gougoussis, Anton Kokalj, Michele Lazzeri, Layla Martin-Samos, Nicola Marzari, Francesco Mauri, Riccardo Mazzarello, Stefano Paolini, Alfredo Pasquarello, Lorenzo Paulatto, Carlo Sbraccia, Sandro Scandolo, Gabriele Sclauzero, Ari P Seitsonen, Alexander Smogunov, Paolo Umari, and Renata M Wentzcovitch. Quantum espresso: a modular and open-source software project for quantum simulations of materials. *Journal Physics Condensed Matter*, 21(39):394402 (19pp), 2009. Available from the website `http://www.quantum-espresso.org`.

[4] N. A. W. Holzwarth, A. R. Tackett, and G. E. Matthews. A Projector Augmented Wave (PAW) code for electronic structure calculations, Part I: *atompaw* for generating atom-centered functions. *Computer Physics Communications*, 135:329–347, 2001. Available from the website `http://pwpaw.wfu.edu`.

[5] J.S. Newman. *Electrochemical Systems*. Prentice-Hall international series in the physical and chemical engineering sciences. Prentice Hall, 1991.

[6] James P. Sethna. Statistical mechanics: Entropy, order parameters, and complexity. In *Oxford Master Series in Physic*. Univ. Press, 2006.

[7] Ryogo Kubo. Statistical-mechanical theory of irreversible processes. i. general theory and simple application to magnetic and conduction problems. *Journal of the Physical Society of Japan*, 12:570–586, 1957.

[8] J. M. Haile. *Molecular Dynamics Simulation: Elementary Methods*. John Wiley & Sons, Inc., 1992. ISBN: 978-0-471-81439-3.

[9] F. Giustino. *Materials Modelling Using Density Functional Theory: Properties and Predictions*. Oxford University Press, 2014.

[10] Jean-Louis Calais. Density-functional theory of atoms and molecules. r.g. parr and w. yang, oxford university press, new york, oxford, 1989. ix + 333 pp. price 45.00. *International Journal of Quantum Chemistry*, 47(1):101–101, 1993.

[11] John P. Perdew and Yue Wang. Accurate and simple analytic representation of the electron-gas correlation energy. *Physical Review B*, 45:13244–13249, 1992.

[12] Jason Howard and N. A. W. Holzwarth. First-principles simulations of the porous layered calcogenides $li_{2+x}sno_3$ and $li_{2+x}sns_3$. *Physical Review B*, 94:064108, Aug 2016.

[13] Ilyas Tarhouchi, Virginie Viallet, Philippe Vinatier, and Michel Mntrier. Electrochemical characterization of li10snp2s12: An electrolyte or a negative electrode for solid state li-ion batteries? *Solid State Ionics*, 296:18 – 25, 2016.

[14] J. A. Brant, D. M. Massi, N. A. W. Holzwarth, J. H. MacNeil, Alexios P. Douvalis, Thomas Bakas, S. W. Martin, M. D. Gross, and J. A. Aitken. Fast lithium

ion conduction in li2sns3: Synthesis, physicochemical characterization, and electronic structure. *Chemistry of Materials*, 27(1):189–196, 2015.

[15] A. Einstein. Über die von der molekularkinetischen Theorie der Wärme gefordert Bewegung von in ruhenden Flüßigkeiten suspendierten Teilchen. (German) [On the molecular-kinetic theory of the movement by heat of particles suspended in liquids at rest].

[16] A. Al-Qawasmeh, J. Howard, and N. A. W. Holzwarth. Li4sns4 and li4snse4: Simulations of their structure and electrolyte properties. *Journal of The Electrochemical Society*, 164(1):A6386–A6394, 2017.

[17] Zachary D. Hood, Hui Wang, Amaresh Samuthira Pandian, Jong Kahk Keum, and Chengdu Liang. Li2ohcl crystalline electrolyte for stable metallic lithium anodes. *Journal of the American Chemical Society*, 138(6):1768–1771, 2016.

[18] J. Howard, Zachary D. Hood, and N. A. W. Holzwarth. Fundamental aspects of the structural and electrolyte properties of li$_2$OHCl from simulations and experiment. *Physical Review Materials*, 1:075406, Dec 2017.

[19] J. Nanda N. J. Dudney, W. C. West. *Handbook of Solid State Batteries*. World Scientific Series in Materials and Energy, 2016. ISBN: 978-981-4651-89-9.

[20] Ah-Young Song, Yiran Xiao, Kostiantyn Turcheniuk, Punith Upadhya, Anirudh Ramanujapuram, Jim Benson, Alexandre Magasinski, Marco Olguin, Lamartine Meda, Oleg Borodin, and Gleb Yushin. Protons enhance conductivities in lithium halide hydroxide/lithium oxyhalide solid electrolytes by forming rotating hydroxy groups. *Advanced Energy Materials*, pages 1700971–n/a. 1700971.

[21] Georg Schwering, Andreas Hönnerscheid, Leo van Wüllen, and Martin Jansen. High lithium ionic conductivity in the lithium halide hydrates li3-n(ohn)cl

(0.83n2) and li3-n(ohn)br (1n2) at ambient temperatures. *ChemPhysChem*, 4(4):343–348, 2003.

[22] P. E. Blöchl. Projector augmented-wave method. *Physical Review B*, 50:17953–17979, 1994.

[23] Stefano Baroni, Stefano de Gironcoli, Andrea Dal Corso, and Paolo Giannozzi. Phonons and related crystal properties from density-functional perturbation theory. *Reviews of Modern Physics*, 73:515–562, Jul 2001.

[24] K. Momma and F. Izumi. Vesta 3 for three-dimensional visualization of crystal, volumetric, an morphology data. *Applied Crystallography*, 44:1272–1276, 2011. Code available from the website `http://jp-minerals.org/vesta/en/`.

[25] Anton Kokalj. XCrySDen– an new program for displaying crystalline structures and densities. *Journal of Molecular Graphics and Modelling*, 17:176–179, 1999. Code available at the website `http://www.xcrysden.org`.

[26] MATLAB. version 8.3.0.532 (r2014a), 2017. MATLAB, The MathWorks, Inc., Natick, Massachusetts, United States.

Part IV

Curriculum Vitae

Contact information

Jason Howard

1202 Aspen Way 27106 Winston Salem

336-953-6681(cell)

howajd14@wfu.edu(work), howardjason8@gmail.com (personal)

Employment history

1. Sep/05-Sep/09

   United States Navy – Interior Communications Electrician

   Honorable Discharge. Last title E-5 group supervisor of alarm and warning, and multi-channel shops on CVN 69 the "Dwight D. Eisenhower"

2. May-June 2014

   Parallel programming using openMP of code used for calculations of scattering cross sections. Work done as summer job for Dr. Deepshikha Shukla who was an assistant professor at UNCG at the time.

Education History

Bachelor of Science – Physics UNCG 2009-2014

Phd– Wake Forest University Physics Department 2014-present, graduating May 2018

My dissertation work is focused on using computational techniques to study the fundamental properties of solid state battery materials.

Self-taught in c++ with 4 years of experience actively writing code for my research. My strength is developing classes using the standard library.

Papers published

1. Jason Howard and N.A.W. Holzwarth "First principles simulations of the porous layered calcogenides $Li_{2+x}SnO_3$ and $Li_{2+x}SnS_3$" Phys. Rev. B **94** 064198 (2016)

2. Ahmad Al-Qawaseh, Jason Howard, and N.A.W. Holzwarth "Li_4SnS_4 and Li_4SnSe_4: Simulations of their Structure and Electrolyte Properties" J. Electrochem. Soc. **164** A6386-A6394 (2017)

3. Jason Howard, Zachary Hood, and N.A.W Holzwarth "Fundamental aspects of the structural and electrolyte properties of Li_2OHCl from simulations and experiment" Phys. Rev. Mat. **1** 075406(2017)

Papers submitted

Jason Howard and N.A.W. Holzwarth. "Analysis of the statistical and convergence properties of ionic transport coefficients with application to the solid electrolyte Li_2OHCl ". Submitted to Solid State Ionics 4/24/2018.

Papers in progress

Understanding the orthorhombic to cubic phase transition in Li_2OHCl, $and\ Li_2OHBr$ using first principles simulations. This work includes the development of an approximation method to the Helmholtz free energy of a system with known multiplicity. This approximation is called the "disordered subspace approximation"

Conferences talks

1. Electrochemical Society 228th meeting Oct 11-15 , 2015 Phoenix AZ
   Jason Howard and N.A.W Holzwarth
   "Computational Study of Li_2SnO_3 and Li_2SnS_3"

2. American Physical Society March meeting 2016. Baltimore MD
   Jason Howard and N.A.W Holzwarth
   "Lithiation of Li_2SnO_3 and Li_2SnS_3 in context of Li-ion battery materials"

3. American Physical Society March meeting 2017 New Orleans LA
   Jason Howard, Zachary Hood, and N.A.W. Holzwarth
   "Computational study of Li_2OHCl as a possible solid state battery material"

4. American Physical Society March meeting 2017 Los Angeles CA
   Jason Howard and N.A.W Holzwarth
   "Computational study of the high ionic conductivity cubic phases of Li_2OHX electrolytes with $X = Cl\ and\ Br$"

Conference posters

1. Recent developments in electronic structure workshop 2017 Princeton NJ
   Jason Howard, Zachary Hood, and N.A.W Holzwarth
   "First principles simulations of Li_2OHCl "

2. 232nd Meeting of the Electrochemical Society Oct 1-5, 2017 National Harbor MD
   Jason Howard, Zachary Hood, and N.A.W. Holzwarth
   "Structural and electrolyte properties of Li_2OHCl"